



Title	Development of Thermal Process Methodology and Mechanochemical Synthesis for Luminescent Copper(I)-halide Complexes
Author(s)	梁, 磐仪
Citation	北海道大学. 博士(理学) 甲第13364号
Issue Date	2018-09-25
DOI	10.14943/doctoral.k13364
Doc URL	http://hdl.handle.net/2115/71832
Type	theses (doctoral)
File Information	LIANG_Panyi.pdf



[Instructions for use](#)

**Development of thermal process methodology and
mechanochemical synthesis for luminescent
copper(I)-halide complexes**

(発光性銅(I)-ハライド錯体のメカノケミカル合成お
よび熱プロセス法の開発)

Panyi Liang

6, 10, 2018

Contents

Chapter 1 General Introduction	1
1-1. Introduction	2
1-2. Luminescence of metal complexes	3
1-3. Luminescence of Copper (I) complexes	4
1-4. Mechanochemical synthesis	9
1-5. Thermal synthesis	11
1-6. Purposes of thesis	13
1-7. Outline of thesis.....	15
1-8. References	17
Chapter 2 Thermal and Mechanochemical Syntheses of Luminescent Mononuclear Copper(I) Complexes	18
2-1. Introduction	19
2-2. Experimental.....	21
2-2-1. Synthesis	21
2-2-2. Physical measurements	22
2-2-3. Luminescence Measurements	24
2-2-4. Theoretical Calculations	25
2-3. Results and discussion	26
2-3-1. Crystal Structures.....	26
2-3-2. Mechanochemical and Thermal Syntheses	28
2-3-3. Photophysical Properties	34
2-4. Conclusion	49
2-5. References	50
Chapter 3 Solvent-free Thermal Synthesis of Luminescent Dinuclear Cu(I) Complexes with Triarylphosphines	53
3-1. Introduction	54
3-2. Experimental.....	56
3-2-1. Synthesis	56
3-2-2. Physical measurements	57
3-2-3. Luminescence measurements	57
3-2-4. Computational methods	57
3-3. Results and discussion	59
3-3-1. Crystal structures	59
3-3-2. Thermal syntheses.....	60
3-3-3. Photophysical properties.....	67
3-4. Conclusion	88
3-5. References	89
Chapter 4 General Conclusions	93

Chapter 1

General Introduction

1-1. Introduction

Since the luminescent materials have been found and highly valued as optical resources, under the consideration of convenience and efficiency with acceptable cost, which has been deeply focused on in the latest 20 years and bring beneficial into our daily life by multiply functionalized and easily accessible. By the mean of controlling the luminescence, the study of luminescence mechanism has contributed largely.

Traditional organic and inorganic luminophores have been extensively explored for their diverse functionalities and applicablilities in lighting¹, optical devices², and sensors³. The unique function of inorganic rare-earth compounds is attributed to the narrow emission wavelength and high color purity from the f-block elements, such as Ce^{3+} , Eu^{2+} , Eu^{3+} , Sm^{2+} , and Cr^{3+} , especially in generate of white and blue light⁴. For the organic and inorganic materials, their application in light emitting diodes by a thin film incorporated with two conductors for the electronic devices, known as OLED or LEDs, thousands of materials have been developed⁵.

Considering of the efficiency and multi-functionalization of luminescent materials, assembling systems of inorganic metal compounds and organic components were highly valued, because both parts can devote to the generation of luminescence. The luminescence originated from ligand-centered charge transfer (CC), metal-metal ligand charge transfer (MMLCT) and metal to ligand charge transfer (MLCT), comparing with the organic clusters or inorganic compounds, the MLCT provide one more dimension of luminescence.

From an environmental friendly perspective, the search of the synthetic methodology of materials are also essential. Recently, mechano-chemical synthesis was considered as an optimal method, by comparing with the mostly developed solution synthesis of metal-organic complexes, which have been obtained by mechano-chemical method with minimal amount of solvent or solvent-free based on the manual grinding or ball milling (*vide infra*)⁶.

As stated above, metal-organic luminescent complexes have attracted intensive attention on the photo-related properties and ligand-related syntheses due to the diversity conjugation of organic and inorganic clusters⁷. In particular, I have focused on copper(I) complexes aiming to construct new luminescent materials with high performance in properties, methodology, and environmental and economic perspectives. The research related to these subjects would deserve further development.

1-2. Luminescence of metal complexes

In recent decades, due to the utilization of light-emitting electro-chemistry cells (LEECs) and organic light emitting diodes (OLEDs), luminescent materials has attracted much attention. The luminescent mechanism of metal complexes is distinct from the organic luminescent materials, because of the introduction of heavy metal atoms which contribute rapid intersystem crossing due to the spin-orbit coupling.

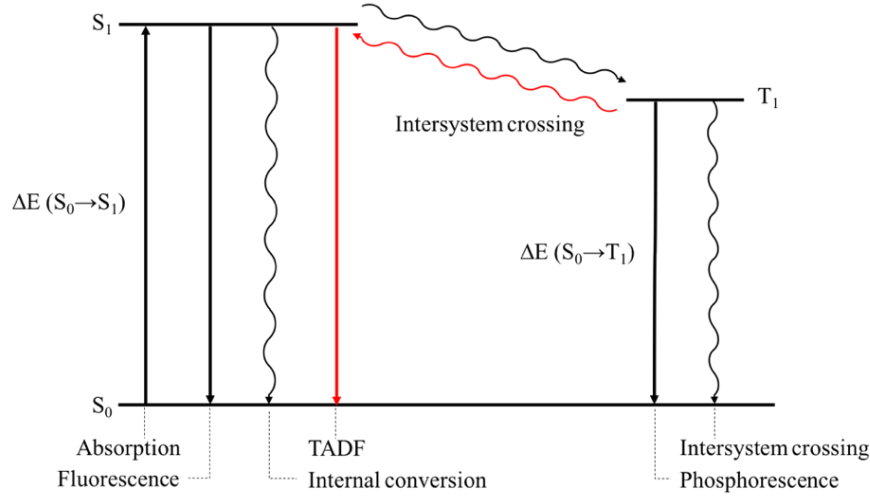


Figure 1-1. The state energy diagram of phosphorescence, fluorescence, and TADF.

Phosphorescence, thermally activated delayed fluorescence (TADF), and fluorescence are defined as the light-emission from the lowest excited singlet state (S₁) and the lowest excited triplet state (T₁), respectively (Figure 1-1). The luminescence properties can be characterized by three parameters: (1) luminescence spectra, including absorption and emission spectra, defined as the function of wavelength, (2) quantum yield, which indicate the efficiency of luminescence and defined by the number of emitted photons in the decay to the number of absorbed photons, (3) lifetime, which refers the average time that photons decay from excited states to ground state. The general expression of quantum yield (Φ) and lifetime (τ) from a specific excited state (S₁ or T₁) is given by Eq. 1-1:

$$\Phi = \Phi^* k_r \left(k_r + \sum k_i \right)^{-1} = \Phi^* k_r \tau \quad \text{Eq. 1 - 1}$$

Where as Φ^* is the formation efficiency of the emitting state, k_r is the radiative rate constant for emission from the S₁ or T₁ state, and $\sum k_i$ is the sum of all rate constants that radiationlessly deactivate the emitting state. The quantum yield (Φ) and lifetime (τ) mainly depending on the $\sum k_i$, as the k_r usually don't change much with experimental conditions, but $\sum k_i$ highly related to the experimental conditions. Thus, in order to obtain the k_r value, measurement of the lifetime (τ) usually carried out with various temperature, from 77K usually, at this temperature, the rigidity of structure is enhanced by comparing with the ambient condition⁸.

1-3. Luminescence of Copper (I) complexes

Copper(I) complexes have attracted much attention recently because of their remarkable luminescence properties. Copper is much cheaper metal than Pt, Au, and iridium, which provide luminescent metal complexes. So, Cu(I) complexes can be economically feasible. Cu(I) complexes are well known to adopt various structures from mononuclear complexes to multinuclear clusters, and highly luminescence materials have been developed by constructing robust structures. In addition, some highly luminescent Cu(I) complexes can be synthesized easily and efficiently by environmental-friendly methods such as solvent-free mechanochemical grinding.⁹

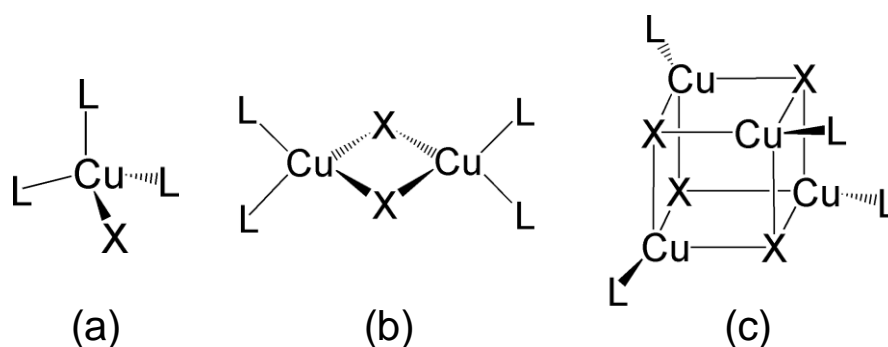


Figure 1-2. Structures of the complexes with (a) $[\text{CuIL}_3]$, (b) $[\text{Cu}_2\text{X}_2\text{L}_4]$ and (c) $[\text{Cu}_4\text{X}_4\text{L}_4]$.

Luminescent copper (I) complexes have been intensively investigated by applying various ligands with N, P, C, and S coordinated. The mostly reported structures are mononuclear $[\text{CuIL}_3]$, dinuclear $[\text{Cu}_2\text{X}_2\text{L}_4]$ and cubic structures $[\text{Cu}_4\text{X}_4\text{L}_4]$ (X = halide; L: N, P, S ligands), as shown in Figure 1-2, and because of the thermochromic and vapochromic luminescent properties, there are some researches focused on the structure transformation between these structures induced by vapor diffusion or mechanochemical grinding.

The strategy using triphenylphosphine as at least one of the ligands has been succeeded in the structure construction exhibiting remarkable luminescent properties. With the mono and bidentate N-heteroaromatic ligands (4,4'-bipyridine, pyrazine, pyrimidine, 1,5-naphthyridine, 1,6-naphthyridine, quinazoline, N,N-dimethyl-4-aminopyridine, 3-benzoylpyridine, 4-benzoylpyridine) (Figure 1-3), a discrete molecular type and extended chain structure were formed, respectively¹⁰. And the reason of the structure variety is due to the geometric flexibility of the $\{\text{Cu}_2\text{X}_2\}$ center. The emission wavelength of these complexes $[\text{Cu}_2\text{X}_2(\text{PPh}_3)_2(\text{L})_n]$ (L= N-heteroaromatic ligands, 4,4'-bipyridine, pyrazine, pyrimidine, piperazine, 1,5-naphthyridine, 1,6-naphthyridine, quinazoline, N,N'-dimethylamino-pyridine, 3-benzoylpyridine, 4-benzoylpyridine) was varied systematically of the N-heteroaromatic ligands from 450 nm to 707 nm, and were assigned to metal-to-ligand charge transfer (MLCT) excited states and mixing with halide-to-ligand charge transfer

(XLCT) characters. The reduction potential of the ligands with π type orbitals are strongly impact on the emission energies of the dicopper complexes. Thus, the origin of the emission is assumed to be the charge-transfer excited states to π^* orbitals of the N-heteroaromatic ligands.

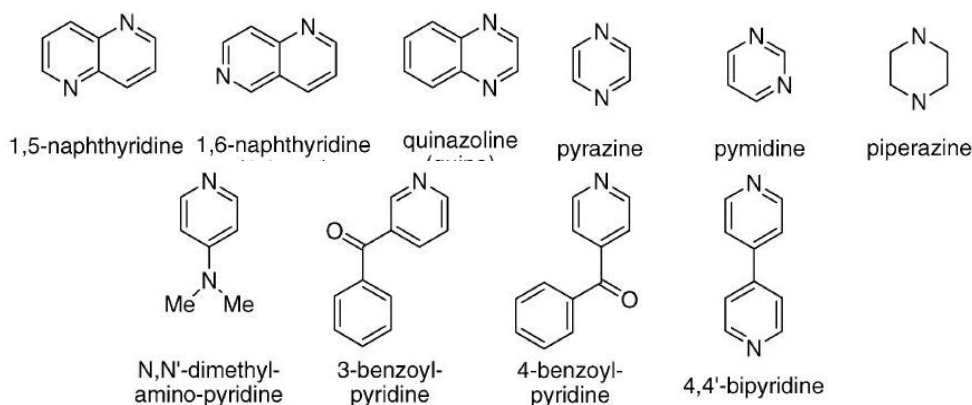


Figure 1-3. N-heteroaromatic ligands used to prepare $[\text{Cu}_2\text{X}_2(\text{PPh}_3)_2(\text{L})_n]$ complexes in reference 10.

Table 1-1. Reduction potentials of N-heteroaromatic ligands (L) and $\lambda_{\text{max}}^{\text{em}}$ of $[\text{Cu}_2\text{Br}_2(\text{PPh}_3)_2(\text{L})_n]$ in reference 10.

L	n	redox potential (V) ^a	$\lambda_{\text{max}}^{\text{em}}$ (nm)
4,4'-bipyridine	2	-1.84	595
pyrazine	2	-2.10	707
pyrimidine	2	-2.35	579
1,5-naphthyridine	2	-1.82	616
1,6-naphthyridine	2	-1.79	633
quinazoline	2	-1.74	644
4-benzoylpyridine	1	-1.46	686
3-benzoylpyridine	1	-1.60	579
pyridine	1	-2.76	487

^a In acetonitrile, vs Ag|AgCl.

The study of copper(I) iodide complexes $[\text{Cu}_4\text{I}_4\text{L}_4]$ (L = $\text{P}(\text{C}_6\text{H}_4\text{OCH}_3)_3$, $\text{P}(\text{C}_6\text{H}_4\text{CH}_3)_3$, and $\text{P}(\text{C}_6\text{H}_4\text{CF}_3)_3$) as shown in Figure 1-4, which the ligand with electron-donating or electron-withdrawing groups, demonstrated that the potential of electron withdrawing has a clear influence on the luminescent properties. Due to the electronic-withdrawing characters, an energy decrease of the unoccupied molecular orbitals was indicated by red shift of absorption band¹¹.

The emerging of high energy (HE) emission band with the decrease of temperature as shown in Figure 1-5. At 295 K, a single unstructured broad emission band centered

at 558 nm for C-OCH₃ and 515 nm for C-CH₃ was found as low energy band (LE). The C-CF₃ cluster presents two broad bands with a more intense peak at 440 nm (HE) and the other one at 525 nm (LE). With the decreasing of temperature, a new emission band of C-OCH₃ and C-CH₃ appeared progressively at higher energy at 415 nm and 420 nm at 77 K for each, along with the concomitant extinction of the LE band of C-OCH₃. For C-CF₃, the two band shows at 295 K, while the LE band decreased and cooling down to 8 K only HE band was observed.

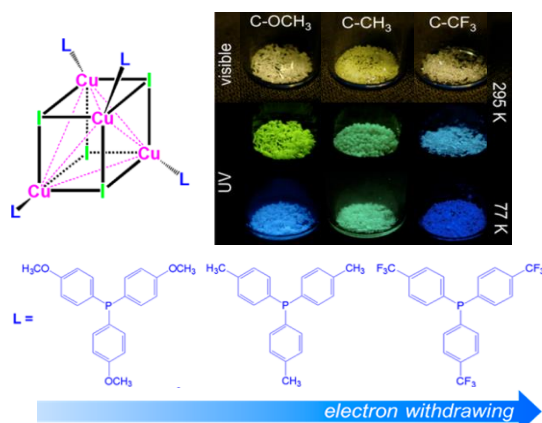


Figure 1-4. General representation of the copper iodide clusters [Cu₄I₄L₄] (L = P(C₆H₄OCH₃), P(C₆H₄CH₃), and P(C₆H₄CF₃)), and photos under UV irradiation (λ=365 nm) at 295 K and 77 K.

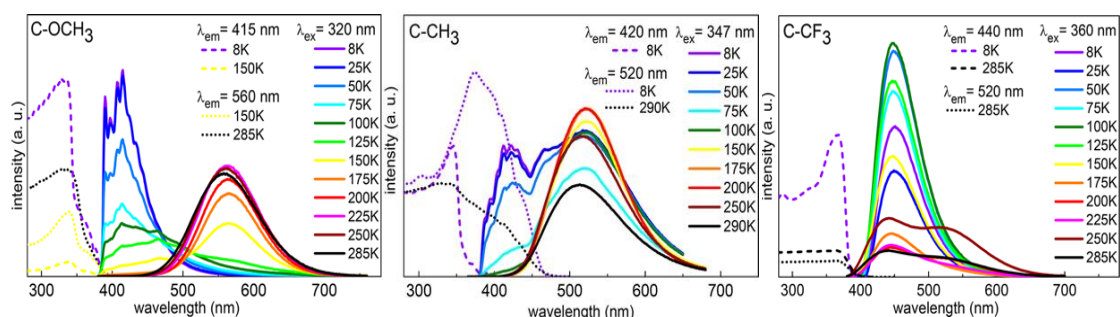


Figure 1-5. Temperature dependence of solid state luminescence spectra of [Cu₄I₄L₄] (L = phosphine ligand) copper iodide clusters showing electron-withdrawing tendency (solid lines for emission; dashed lines for excitation) in reference 11.

The polymorph and isomer conversion of CuI cored complexes corresponded to the versatile photophysical properties has been investigated in solution and in solid state. Lucia Maini, et al, reported that the solid state reactions of stoichiometries of CuI and PPh₃ by kneading and vapor digestion the polymorph [CuI(PPh₃)₄] conversion between cubane-like **1a** and **1b**, and isomer step-like **2** [CuI(PPh₃)₄] were obtained as shown in Figure 1-7. The crystal structure of polymorph **1a** and **1b**, and isomer **2** are as shown in Figure 1-6.¹²

The solid states excitation and emission spectra of **1a** (Figure 1-8) suggest that the green-yellow emission at 544 nm at room temperature and a dual emission maximum at 410 nm and 591 nm at 77 K can attributed to 3CC (triplet cluster to cluster charge transfer) and the red-shift of low temperature resulted from the shortening of the Cu-Cu distance (for **1a** and **1b** at RT are 2.839(3) Å and 2.945(4) Å, and at 90 K 2.7427(8) Å and 2.828(2) Å, respectively). The green emission of **1b** at 518 nm at room temperature largely blue-shifted comparing with that of **1a**, and a dual emission with intense band centered at 434 nm and less intense band at 516 nm. The reduced shift of **1a** to **1b** at low energy band with temperature was attributed to the longer Cu-Cu distances the distortion of the 3CC state with respect to the ground state is reduced. As well as the emission of **2**, Cu-Cu distance in the unit cell is close to the orbital interaction limit leads to weak emission and slightly blue-shifted emission can be assigned to 3XLCT (triplet halide to ligand charge transfer) at both temperatures.

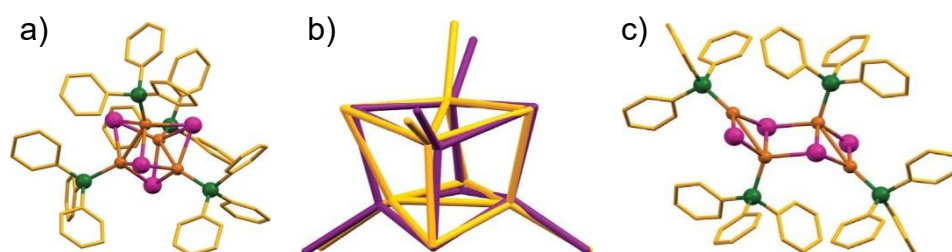


Figure 1-6. a) The $[\text{CuI}(\text{PPh}_3)_4]$ cubane-like unit, hydrogen atoms are removed for clarity; b) Overlap between Cu_4I_4 clusters in $[\text{CuI}(\text{PPh}_3)_4]$ **1a** (yellow) and **1b** (purple), phenyl rings are removed for clarity; c) The $[\text{CuI}(\text{PPh}_3)_4]$ form of **2**, hydrogens are removed for clarity.

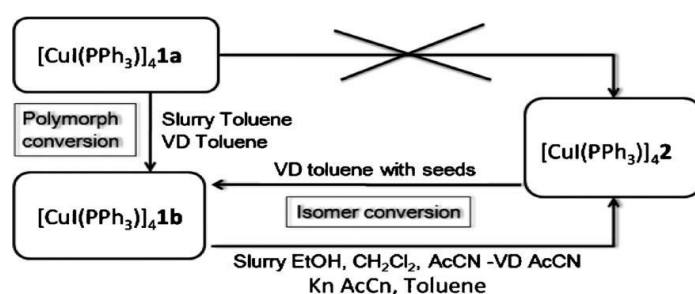


Figure 1-7. Interconversions between polymorphic and isomeric forms (VD: vapor digestion, Kn: kneading).

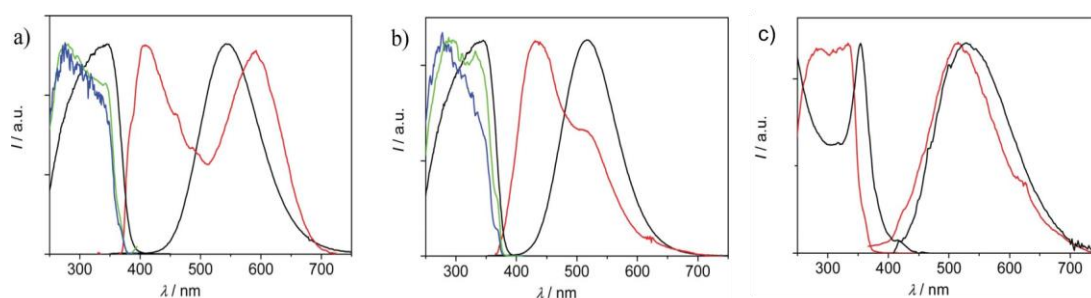


Figure 1-8. Normalized emission and excitation spectra of solids a) $[\text{CuI}(\text{PPh}_3)_4]$ (form

1a), b) $[\text{CuI}(\text{PPh}_3)_4]$ (form **1b**), c) $[\text{CuI}(\text{PPh}_3)_4]$ (form **2**), at room temperature (black lines) and at 77 K (red lines). For a) and b) the excitation spectra at 77 K measured on the HE band are in green lines whereas the measurement on the LE band are in blue lines.

1-4. Mechanochemical synthesis

In the past decade, driven by the search for new and cleaner synthetic methodologies, solid-state approaches have been highly evaluated. The mechanical treatment of solid materials by the means of grinding by ball milling or manual grinding enabled by mechanical force, is one of the widely used operations with which the inorganic and organic materials both has been successfully obtained.

The cause of the reactions was recognized as a heating process, at very first as an experience. And then the reactivity was considered as a result of increase in the specific surface of the solid states.¹³ Until recently, the more detailed studies concerning about the process of mechanochemical in the field of mechanochemistry was realized worth-well for specific investigation due to the quickly and quantitatively reactions, and especially the solvent-free or minimal solvent needed. The mechanochemical method is considered to be separated into two parts depending on the solvent: the solvent-free and liquid assisted grinding (in the term of kneading).

The first solvent-free mechanochemical synthesis of a microporous metal-organic framework [Cu(INA)₂] (INA= isonicotinic acid) with a robust 3-dimensional connectivity was reported by Anne Pichon et al.¹⁴ The color change of the mixture after ball milling indicated the formation of the reaction, and the grinding time has impact on the microscopic morphologies of the MOFs. By comparing the grinding for 1 minutes (as to initiate the reaction) to 5 minutes, after one week standing, the SEM images shown in Figure 1-9 with larger crystals and have more clearly defined faces and edges, as well as more intense peaks at higher 2- θ values comparing with 10 minutes grinding (Figure 1-10).

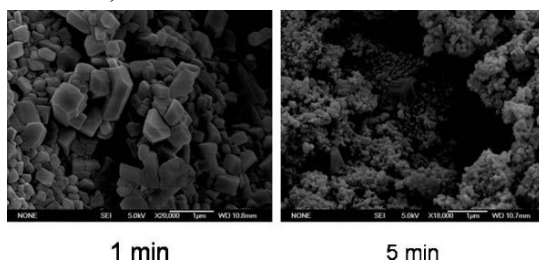


Figure 1-9. SEM images of samples prepared by grinding for 1 minute or for 5 minutes, after standing for one week.

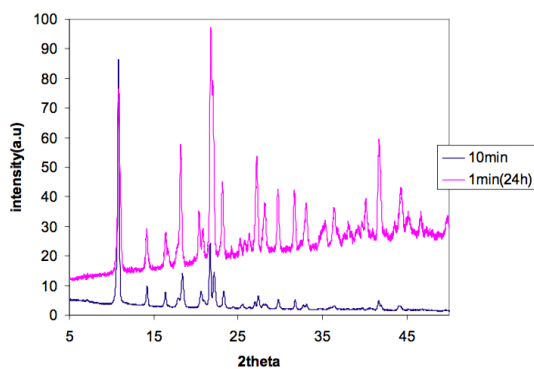


Figure 1-10. Comparison of PXRD patterns from samples of material **1** prepared by 1 and 10 minutes grinding.

luminescent copper (I) cyanide (CuCN) coordination polymers with three-dimensional structures were synthesized by directly kneading of CuCN and thiourea and other five derivatives as shown in Figure 1-11. In the case of $[(\text{CuCN})_2(\text{tu})]_n$, $[(\text{CuCN})_5(\text{mtu})_3]_n$, $[(\text{CuCN})(\text{ptu})]_n$, and $[(\text{CuCN})_3(\text{fptu})_2]_n$ minimal amount of water or water/acetonitrile solution 1:1 was used; $[(\text{CuCN})(\text{dptu})]_n$ was yielded by kneading with minimal amount of ethanol or water acetonitrile solution 1:1. The yield of these compounds were between 95% to 98%.¹⁵

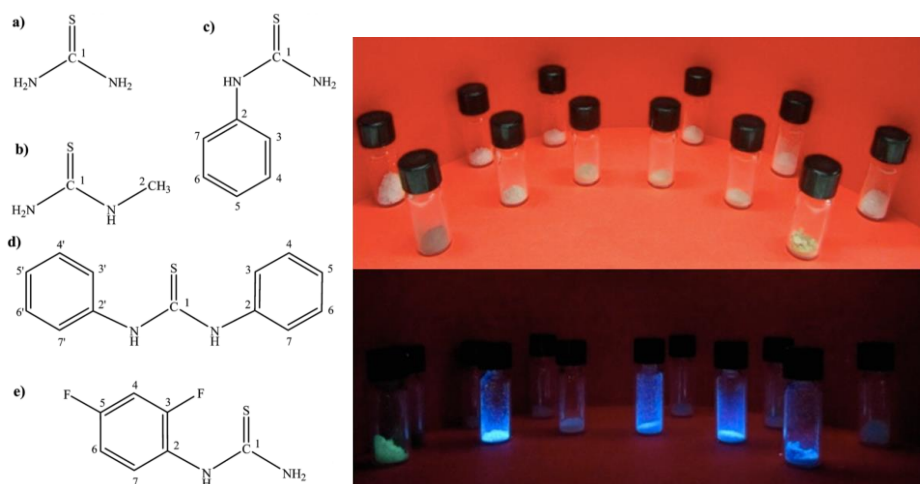


Figure 1-11. Pictures of powdered samples: from left to right, $[(\text{CuCN})_2(\text{tu})]_n$, $[(\text{CuCN})_5(\text{mtu})_3]_n$, $[(\text{CuCN})_3(\text{mtu})_2]_n$, $[(\text{CuCN})(\text{ptu})]_n$, $[(\text{CuCN})(\text{dptu})]_n$, and $[(\text{CuCN})_3(\text{fptu})_2]_n$ and backward corresponding ligands tu (a), mtu (b), mtu (b), ptu (c), dptu (d), and fptu (e) under visible light (above) and under 365 nm light (below).

The highly luminescent mononuclear copper(I) iodide complexes have been reported by Ohara et. al which were prepared by simple manual grinding for several minutes. As shown in Figure 1-12, the mixture of CuI, triphenylphosphine (PPh_3), and ligand (isoquinoline, 1,6-naphthyridine, and pyridine) was not luminescent before grinding, while, after 8 s grinding for isoquinoline, the green luminescent materials was obtained, and at 2 min, the reaction was already processed.¹⁶

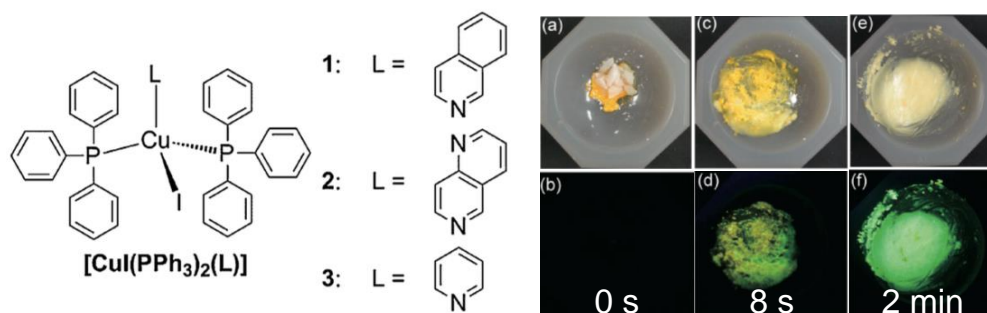


Figure 1-12. Schematic representation of complexes and synthetic process of 1 by manual grinding under bright field (a, c, e) and UV-light (b, d, f).

1-5. Thermal synthesis

Under the consideration of environmental-friendly process, comparing with the conventional solution method, mechanochemical method is optimal, by using minimal amount of solvent, environmentally nontoxic solvent such as H₂O, ethanol, or solvent-free. In the case of ligands with crystallized H₂O or liquid state ligand sacrificed as solvent, in which liquid state were involved. The thermal introduced liquid state at high temperature was considered and the reactions at high temperature was solid-solid or liquid involved was discussed.

The synthesis of solid state reactions introduced by high temperature usually applied in a single precursor to phase transformation, and two or more precursors to one product. Thermal method was highly recognized by inorganic chemistry in the preparation of ceramic while which is severely applied in the preparation of coordination compounds, especially the luminescent metal-organic materials. As the materials obtained by solid states reaction are microcrystals instead of single crystals by solution method, notably, the severe compounds as I found until now prepared by heating introduced, novel structures were obtained which are difficult or impossible by conventional method in solution. The identification of the structure usually characterized by powder X-ray diffraction (PXRD) and recrystallization in solvent or conventional solution method.

The studies of thermal synthesis of coordination compounds Zn(4-pymo)₂ by heating of ground mixture of ZnO and 4-Hpymo (4-Hydroxypyrimidine) at 140°C, which is lower than the melting of 4-Hpymo (164.5 °C), for 2 h under N₂ atmosphere, and the crude product was suspended in acetone (40 mL) and stirred for 2 h at room temperature was considered as a solid-state reaction. Due to the multi-coordinate properties of 4-Hpymo, each zinc ion lies in a nearly tetrahedral N₃O environment, which is uncommon in the Hpymo compounds as shown in Figure 1-13. As in the conventionally synthesized structures, the zinc ion usually in the N, N'-exo-bidentate mode.¹⁷

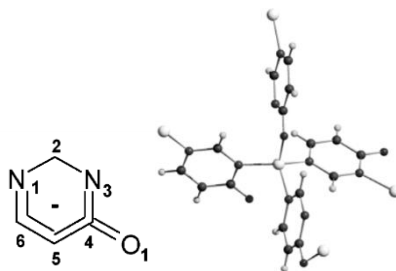


Figure 1-13. Structure of 4-Hpymo (4-hydroxypyrimidine) and crystal structure of Zn(4-pymo)₂ characterized by ab initio X-ray powder diffraction.

The thermal synthesis of copper complex with one coordinating ligand was found with identified by PXRD, as reported by Dario Brago et al. The heating of a mixture of CuI and DABCO (1,4-diazabicyclo [2.2.2] octane) at 353 K yielded a new compound with unclear crystal structure but not identical with the kneading or the solution synthesized 2D-coordination polymer [Cu₂I₂(DABCO)₂]_∞ as shown in Figure 1-14.¹⁸

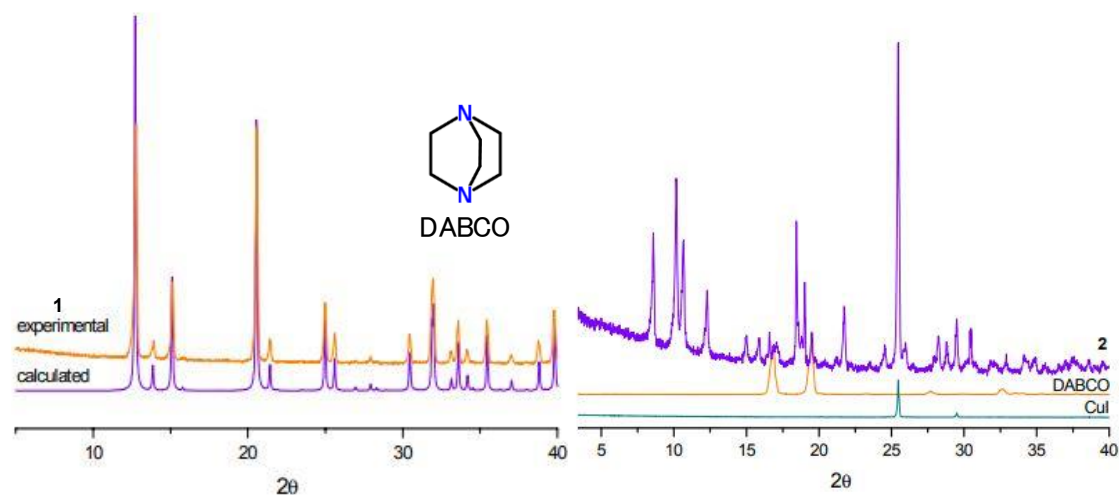


Figure 1-14. Comparison of calculated and experimental PXRD of $[\text{Cu}_2\text{I}_2(\text{DABCO})_2]_\infty$ **1** and thermally synthesized complex **2**.

The mechanism of the process thermal synthesis of luminescent metal-organic complex has not been clearly reported as much as I know. Under the consideration of the development of environmental friendly solvent-free chemistry, the exploration of thermal method is necessary.

1-6. Purposes of thesis

There are a number of copper(I) luminescent complexes has been synthesized by conventional solution method and several reports about mechanochemical grinding synthesis with solvent-free or minimal amount of solvent. However, the development of environmental-friendly, cleaner, safer and more efficient chemical industries is necessary as the limitation amount and hazardous of organic solvent as well as the disposal of wasted solvents.

The differences between the solvent-free and minimal amount needed mechanochemical synthesis was mainly depend on the melting point of ligands, as our group reported. The using of minimal amount of solvent in mechano-chemical process was considered related to the higher melting point of ligands, as reported in the complex system $[\text{CuI}(\text{PPh}_3)_2\text{L}]$, the melting point of ligands pyridine (-41.6°C) isoquinoline (23°C) and naphthyridine (35°C) are near room temperature (25°C).¹⁶ while in the case of $[\text{Cu}_2\text{I}_2(\text{L}_2)]_\infty$ (L=piperazine, melting point 106°C), drops of acetonitrile was added.¹⁸ Thus, only if the melting point of ligand is lower or around room temperature (py: pyridine, iq: isoquinoline, and nap: 1,6-naphthyridine), the complexes $[\text{CuI}(\text{PPh}_3)_2\text{L}]$, (L=py, iq, nap) were obtained by simple grinding. While, in the case of higher melting point ligands, after grinding there was no reaction was observed as I identified by PXRD.

The magma plasma theory and the hot spot theory of mechanochemical reactions emphasize the importance of temperature during the initiate of mechanochemical reactions. *In situ* Raman spectroscopy coupled with thermography of IR camera was applied to investigate the influence of temperature on the reactivity on a structure level was reported by Hannes Kulla et al.¹⁹ Ball milling of mixtures of theobromine and oxalic acid as well as pyrazinamide and oxalic observed temperature increased during milling, and during the reaction process, which was identified by IR and PXRD, temperature increased at a higher speed than single material and the temperature after 20 min milling resulted higher than the single particles. The course of the reaction can be analyzed by local temperature maxima followed by a cooling period caused by releasing of crystallization water.

In order to eliminate the impact of organic solvent to environment and improve the yield and under the consideration of melting point effects and hot spot theory, solvent-free thermal synthesis which has rarely used in coordination complex was investigated in this thesis. Simply by heating the mixture of ligands at a temperature related to the melting point of them, As the versatile coordination properties of copper(I) complex and easily oxidized to copper(II) complex which afford non-luminescence, a precisely control of heating temperature and molar ratio was precisely controlled.

In order to find the relation between the melting point of ligands and heating temperature for complexation, isoquinoline derivatives and triphenylphosphine derivatives with small difference of melting point were applied. The identification of reaction process was observed by various temperature of PXRD and thermogravimetric (TG).

As the decomposition of complexes and form of amorphous states might occur in the heating process, which leads to decrease of the luminescence efficiency, the luminescence efficiency of thermally synthesized complex was compared with the conventionally synthesized single crystals.

1-7. Outline of thesis

This thesis consists of 4 chapters, and briefly described as follow.

In chapter 1, the background and purpose of this studies are introduced with related references.

In chapter 2, mononuclear CuI iodide complexes, $[\text{CuI}(\text{PPh}_3)_2\text{L}]$ $\{\text{PPh}_3 =$ triphenylphosphine; $\text{L} =$ 4-aminoisoquinoline (4-aiq) (**2**), 5-aminoisoquinoline (5-aiq) (**3**), and 5-nitroisoquinoline (niq) (**4**) $\}$, as shown in Figure 1-15, were prepared by three different methods: normally used reactions in the solution state, mechanochemical synthesis, and newly developed solvent-free thermal synthesis. The amino-functionalized isoquinoline complexes were successfully synthesized by heating the ground mixture of three types of starting materials at ca. 100 °C, where the PPh_3 ligand melted to promote complex formation by acting as the ligand and the solvent. The emission properties strongly depend on the L ligand.

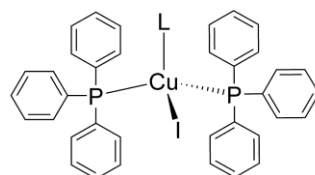


Figure 1-15. structure formula of mononuclear complex and ligand **1-4**.

In chapter 3, luminescent dinuclear Cu(I) complexes, $[\text{Cu}_2\text{I}_2(\text{pyrpy})_2(\text{PR}_3)_2]$ (pyrpy = 4-pyrrolidinopyridine; $\text{PR}_3 =$ triphenylphosphine (**5**), tri(*m*-tolyl)phosphine (**6**), tri(*p*-tolyl)phosphine (**7**)), as shown in Figure 1-16, were prepared from the solution reaction and seldom-reported solvent-free thermal synthesis. X-ray structure analysis revealed that dinuclear $\{\text{Cu}_2\text{I}_2\}$ core, surrounded by two PR_3 and two pyrpy ligands, is formed. Although the melting point of the pyrpy ligand is the lowest among the ligands used in this study, the temperature to form luminescent dinuclear complex in the thermal synthesis strongly depends on the PR_3 ligand. Two of the three complexes (**5** and **7**) have successfully prepared by solvent-free thermal synthesis. Emission lifetime measurements and time dependant density functional theory (TDDFT) calculations suggest the thermally-activated delayed fluorescence (TADF) from the excited state having charge-transfer character between $\{\text{Cu}_2\text{I}_2\}$ core and PR_3 ligands.

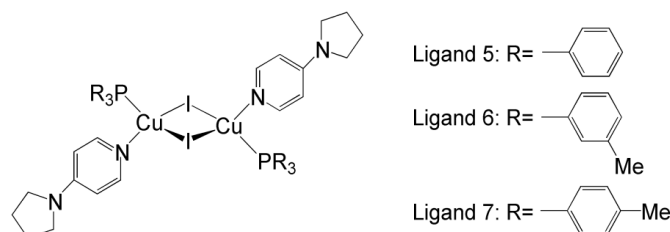


Figure 1-16. Dinuclear structure formula and ligand **5-7**.

In chapter 4, the general conclusion of this thesis was summarized and future perspective of thermal thesis was proposed.

1-8. References

- [1] Ryota Kabe, and Chihaya Adachi, *Nature*, 2017, 550, 384-388.
- [2] Cees Ronda, *Journal of Luminescence*, 2002, 100, 301-305.
- [3] Hiroyuki Suzuki, Atsushi Yokoo, and Masaya Notomi, *Polym. Adv. Technol.*, 2004, 15, 75-80.
- [4] Matthew S. Tremblay, Minhee Lee, and Dalibor Sames, *Org. Lett.*, 2008, 10(1), 5-8.
- [5] (a) G.M. Farinola and R. Ragni, 2015, *Journal of solid state lighting*, 2-9; (b) Bhushan P. Kore, N.S. Dhoble, S.P. Lochab, and S.J. Dhoble, *Journal of Luminescence*, 2014, 145, 299-306; (c) Francisco G. Montoya, Antonio Pena-Garcia, Adel Juaidi, and Francisco Manzano-Agugliaro, 2017, *Energy and buildings*, 140, 50-60; (d) M.K. Bamgbose, P.O. Adebambo, G.T. Solola, B.S. Badmus, E.O. Dare, and G.A. Adebayo, *Materials Letters*, 2018, 221, 330-335.
- [6] (a) Jean-Louis Do and Tomislav Friscic, 2017, *ACS Cent. Sci.*, 3, 13-19; (b) Daniel Prochowicz, Iwona Justyniak, Arkadiusz Kornowicz, Tomasz Kaczorowski, Zbigniew Kaszkur, and Janusz Lewinski, *Chem. Eur. J.* 2012, 18, 7367-7371.
- [7] Wei Liu, Kun Zhu, Simon J. Teat, Gangotri Dey, Zeqing Shen, Lu Wang, Deirdre M. O'Carroll, and Jing Li, *J. Am. Chem. Soc.*, 2017, 139, 9281-9290.
- [8] *Principles of molecular photochemistry, an introduction*, Nicholas J. Turro, V. Ramamurthy, J.C. Scaiano, 223-225.
- [9] (a) Manoj Trivedi, Gurmeet Singh, Abhinav Kumar, and Nigam P. Rath, *Dalton Trans.*, 2014, 43, 13620-13629; (b) Maria Klimakow, Peter Klobes, Klaus Rademann, Franziska Emmerling, *Microporous and mesoporous materials*, 2012, 154, 113-118.
- [10] Hiromi Araki, Kiyoshi Tsuge, Yoichi Sasaki, Shoji Ishizaka, and Noboru Kitamura, *Inorg. chem.*, 2005, 44, 26, 9667-9675.
- [11] Brendan Huitorel, Hani El Moll, Raquel Utrera Melero, Marie Cordier, Alexandre Fargues, Alain Garcia, Florian Massuyeau, Charlotte Martineau-Corcus, Franck Fayon, Aydar Rakhmatullin, Samia Kahlal, Jean-Yves Saillard, Thierry Gacoin, and Sandrine Perruchas, *Inorganic chemistry*, 2018, DOI.10.1021/acs.inorgchem.7b03160.
- [12] Lucia Maini, Dario Braga, Paolo P. Mazzeo and Barbara Ventura, *Dalton Trans.*, 2012, 41, 531-539.
- [13] V.V. Boldyrev, *Solid state ionics*, 1993, 63-65, 537-543.
- [14] Anne Pichon, Ana Lazuen-Garay and Stuart L. James, *CrystEngComm*, 2006, 8, 211-214.
- [15] Francesca Grifasi, Michele R. Chierotti, Claudio Garino, Roberto Gobetto, Emanuele Priola, Eliano Diana, and Francesco Turci, *Cryst. Growth Des.* 2015, 15, 2929-2939.
- [16] Hiroki Ohara, Atsushi Kobayashi, and Masako Kato, *Chem. Lett.* 2014, 43, 1324-1326.
- [17] Elisa Barea, Jorge A. R. Navarro, Juan M. Salas, Norberto Masciocchi, Simona Galli, and Angelo Sironi, *Coordination frameworks containing the pyrimidin-4-olate ligand*. *Inorg. Chem.* 2004, 43, 473-481.
- [18] Dario Brago, Fabrizia Grepioni, Lucia Maini, Paolo P. Mazzeo and Barbara Ventura, *New J. Chem.*, 2011, 35, 339-334.
- [19] Hannes Kulla, Manuel Wilke, Franziska Fischer, Mathias Rollig, Christiane Maierhofer and Franziska Emmerling, *Chem. Commun.*, 2017, 53, 1664-1667.

Chapter 2

Thermal and Mechanochemical Syntheses of Luminescent Mononuclear Copper(I) Complexes

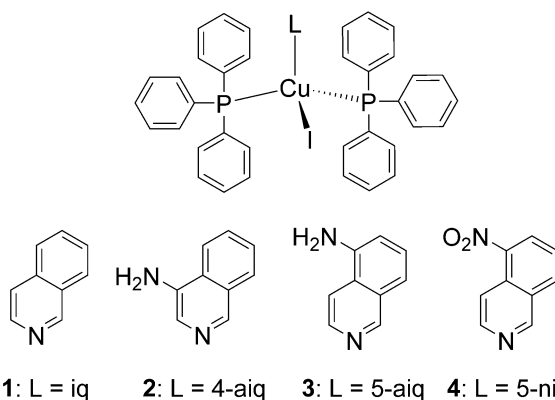
2-1. Introduction

Monovalent Cu complexes have been widely studied in the field of luminescent materials, because they are promising candidates for solar-energy conversion,^[1] organic light-emitting diodes (OLEDs),^[2] biosensors,^[3,4] chromic sensors,^[5,6] and lightemitting electrochemical cells (LEECs).^[7] One of the characteristic features of the emissive Cu^I complexes is their diverse emission origins, involving metal-to-ligand charge transfer (MLCT), halide-to-ligand charge transfer (XLCT), ligand-to-ligand charge transfer (LLCT), and ligand-centered (LC) and cluster-centered (CC) states.^[8–14] In recent years, it has been well established that the structural rigidity around the CuI center is crucial to the design of highly emissive complexes, because the geometric distortion in the excited state is suppressed.^[15–24] The development of environmentally friendly and efficient synthetic methods is another way to reduce the potential risk of environmental pollution by harmful organic solvents. In this context, mechanochemical synthesis has attracted considerable attention as an alternative to conventional solution-state reactions.^[25–29] A typical example was reported by Braga et al.,^[30] 2D coordination polymers [Cu₂I₂(L)₂]_∞ (L = piperazine) with thermochromic luminescence properties were successfully synthesized by kneading them with drops of acetonitrile.

Cu^I cyanide-based 3D complexes with thiourea derivatives were also synthesized by mechanochemical grinding with a minimal amount of solvent; compared with hydrothermal synthesis, almost double the yield was reported by Grifasi et al.^[31] Ohara et. al also previously reported the mechanochemical syntheses of luminescent mononuclear^[32,33] and Kobayashi et. al reported the dinuclear CuI complexes,^[34] [CuI(PPh₃)₂L] and [Cu₂X₂(dpypp)₂] {X = Cl, Br, I; PPh₃ = triphenylphosphine; L = pyridine, isoquinoline (iq), 1,6-naphthyridine(nap); dpypp = 2,2'-(phenylphosphinediyl)dipyridine}. I found that a minimal amount of assisting solvent (e.g., acetonitrile) was necessary to dissolve the starting materials in the synthesis of dinuclear [Cu₂X₂(dpypp)₂] complexes, whereas no assisting solvent was required in the mechanochemical synthesis of the two mononuclear complexes, [CuI(PPh₃)₂(iq)] and [CuI(PPh₃)₂-(nap)]. However, the reason for this difference was not clear.

In this work, I have focused on the role of the L ligand of the mononuclear complex system [CuI(PPh₃)₂L] in mechanochemical synthesis. I hypothesized that the melting point of the ligand is one of the crucial factors for mechanochemical synthesis; that is, the melting points of two ligands, iq (23 °C) and nap (35 °C), are close to room temperature. Such low melting points enable them to partially melt during the grinding, thereby, promoting the complex-formation reactions. To validate our hypothesis, three functionalized isoquinoline derivatives (Scheme 1; 4-aiq = 4-aminoisoquinoline, 5-aiq = 5-aminoisoquinoline, and 5-niq = 5-nitroisoquinoline), were selected as the L ligand of mononuclear complex [CuI(PPh₃)₂L], because these ligands have higher melting points (> 100 °C) than iq. Herein, I report the mechanochemical and solvent-free thermal syntheses, crystal structures, and luminescence properties of the mononuclear CuI complexes [CuI(PPh₃)₂L]. The mechanochemical synthesis of the functionalized isoquinoline complexes did not proceed in the absence of an assisting solvent, but

proceeded in the presence of benzonitrile (PhCN) as the assisting solvent. Further, the solvent-free thermal synthesis of the amino-functionalized isoquinoline complexes was successfully carried out by simply heating the ground mixture at approximately the melting point of the PPh₃ ligand, affording the luminescent Cu^I complexes directly onto the surface of the substrate.



Scheme 2-1. Schematic representation of complexes **1–4**.

2-2. Experimental

Caution! Although I experienced no difficulties, all of the solvents used in this study are potentially harmful and should be used in small quantities and handled with care in a fume hood.

2-2-1. Synthesis

General Procedures: All of the commercially available starting materials were used as received, and the solvents were used without any purification. The Cu^I complex with unmodified isoquinoline, [CuI(PPh₃)₂(iq)] (**1**), was synthesized according to our previous literature method.^[32] Unless otherwise stated, all of the manipulations were conducted under an air atmosphere.

Synthesis of [CuI(PPh₃)₂(4-aiq)] (**2**)

Preparation of Single Crystals (2S): Compounds 4-aiq (36.2 mg, 0.25 mmol), PPh₃ (98.4 mg, 0.375 mmol), and CuI (24.3 mg, 0.125 mmol) were dissolved in CH₂Cl₂ (2 mL). Yellow crystals were obtained by slowly diffusing diethyl ether vapor into the solution for 48 h. The crystals were collected, washed with diethyl ether, and dried under vacuum. Yield: 47.6 mg, 44 %. C₄₅H₃₈CuIN₂P₂ (859.21): calcd. C 62.91, H 4.46, N 3.26; found C 62.85, H 4.36, N 3.18.

Manual Grinding Synthesis (2M): CuI (48.4 mg, 0.25 mmol), PPh₃ (262.4 mg, 1.0 mmol), and 4-aiq (72.7 mg, 0.5 mmol) were manually ground using a mortar and pestle for 5 min. Then, four drops of PhCN were added, and the mixture was ground for 10 min. The obtained yellow powder was collected by suction filtration, washed with diethyl ether, and dried under vacuum. Yield: 183.9 mg, 85.6 %. C₄₅H₃₈CuIN₂P₂ (859.21): calcd. C 62.91, H 4.46, N 3.26; found C 62.41, H 4.34, N 3.18.

Thermal Synthesis (2T): CuI (48.8 mg, 0.25 mmol), PPh₃ (262.9 mg, 1.0 mmol), and 4-aiq (73.1 mg, 0.5 mmol) were manually ground using a mortar and pestle for 5 min. Then, the mixture was heated at 85–90 °C for 30 min. Finally, the yellow powder obtained was collected by suction filtration, washed with diethyl ether, and dried under vacuum. Yield: 192.7 mg, 89.7 %. C₄₅H₃₈CuIN₂P₂ (859.21): calcd. C 62.91, H 4.46, N 3.26; found C 62.56, H 4.34, N 3.23.

Synthesis of [CuI(PPh₃)₂(5-aiq)] (**3**)

Preparation of Single Crystals (3S): Compounds 5-aiq (57.2 mg, 0.4 mmol), PPh₃ (209.6 mg, 0.8 mmol), and CuI (57.3 mg, 0.3 mmol) were dissolved in CHCl₃ (3 mL). Yellow crystals were obtained by slowly diffusing diethyl ether vapor into the solution for 48 h. Then, the crystals were collected by suction filtration, washed with diethyl ether, and dried under vacuum. Yield: 67.5 mg, 52.4 %. C₄₅H₃₈CuIN₂P₂ (859.21): calcd. C 62.91, H 4.46, N 3.26; found C 62.83, H 4.42, N 3.26.

Manual Grinding Synthesis (3M): Compounds 5-aiq (72.2 mg, 0.5 mmol), PPh₃ (198.8 mg, 0.75 mmol), and CuI (48.2 mg, 0.25 mmol) were added to a mortar and ground for 5 min. Then, four drops of PhCN were added, and the mixture was ground for 10 min. A pale yellow powder was collected by filtration, washed with diethyl ether, and dried under vacuum. Yield: 169.3 mg, 78.8 %. C₄₅H₃₈CuIN₂P₂ (859.21): calcd. C 62.91, H 4.46, N 3.26; found C 62.77, H 4.38, N 3.20.

Thermal Synthesis (3T): Compounds 5-aiq (261.3 mg, 1.5 mmol), PPh₃ (594.5 mg, 2.25 mmol), and CuI (143.8 mg, 0.75 mmol) were added to a mortar and manually ground using a pestle for 5 min. A pale-yellow powder was collected by heating the mixture at 100 °C, 30min. After cooling to room temperature, the obtained yellow powder was collected by filtration, washed with diethyl ether, and dried under vacuum. Yield: 591.2 mg, 91.7 %. C₄₅H₃₈CuIN₂P₂ (859.21): calcd. C 62.91, H 4.46, N 3.26; found C 62.68, H 4.37, N 3.26.

Synthesis of [CuI(PPh₃)₂(5-niq)] (4)

Preparation of Single Crystals (4S): PPh₃ (65.6 mg, 0.25 mmol), CuI (16.2 mg, 0.08 mmol), and 5-niq (29.2 mg, 0.17 mmol) were dissolved in CHCl₃ (4 mL). Orange crystals were obtained by slowly diffusing diethyl ether vapor into the solution for 48 h. Then, the crystals were collected by filtration, washed with diethyl ether, and dried under vacuum. Yield: 23.9 mg, 32 %. C₄₅H₃₆CuIN₂O₂P₂ (889.19): calcd. C 60.78, H 4.08, N 3.15; found C 60.62, H 3.99, N3.08.

Manual Grinding Synthesis (4M): Compounds 5-niq (87.2 mg, 0.5 mmol), PPh₃ (198.7 mg, 0.75 mmol), and CuI (48.1 mg, 0.25 mmol) were added to a mortar and ground manually for 5 min using a pestle. Then, three drops of PhCN were added, and the mixture was ground for 10 min. An orange complex was collected by suction filtration, washed with diethyl ether, and dried under vacuum. Yield: 194.1 mg, 87.3 %. C₄₅H₃₆CuIN₂O₂P₂ (889.19): calcd. C 60.78, H 4.08, N 3.15; found C 60.36, H 3.96, N 2.97.

2-2-2. Physical measurements

Elemental analyses and ESI-TOF mass spectroscopic analyses were performed with a MICRO CORDER JM 10 analyzer and a JEOL JMS-T100LP spectrometer, respectively, at the Analysis Center, Hokkaido University.

Single-Crystal XRD Measurements: All single-crystal XRD measurements were conducted with a Rigaku Mercury70 diffractometer, equipped with graphite-monochromated Mo-K α radiation ($\lambda = 0.71075 \text{ \AA}$) and a rotating anode generator. The single crystal was mounted on a MicroMount using paraffin oil. Then, the crystal was cooled using a N₂-flow-type temperature controller. The diffraction data were collected and processed with the CrystalClear software.^[37] Structures were solved by the direct method using SIR2011.^[38] Structure refinements were conducted by the fullmatrix least-squares refinement using SHELXL2013.^[39] The nonhydrogen atoms were refined anisotropically, and the hydrogen atoms were refined using the riding model. All of the calculations were conducted using the CrystalStructure crystallographic software package.^[40] The crystallographic data obtained for each complex are shown in Table 2-2.

CCDC 1557191 (for **2**), 1557192 (for **3**), and 1557193 (for **4**) contain the supplementary crystallographic data for this paper. These data can be obtained free of charge from The Cambridge Crystallographic Data Centre.

PXRD Measurements: PXRD was conducted with a Bruker D8 Advance

diffractometer, equipped with a graphite monochromator using Cu-K α radiation and one-dimensional LinxEye detector.

Table 2-1. Selected bond distances(Å), bond angles and torsion angles (°) around Cu(I) ions of complexes **1-4**.

Complex	1-α^a	1-β^a	2	3	4
Bond distances (Å)					
Cu1-N1	2.125(4)	2.120(2)	2.142(2)	2.099(3)	2.110(3)
Cu1-I1	2.6514(8)	2.6288(5)	2.6574(6)	2.6467(5)	2.6418(4)
Cu1-P1	2.271(1)	2.2858(8)	2.2713(8)	2.3101(9)	2.2716(8)
Cu1-P2	2.287(1)	2.2807(8)	2.2745(8)	2.2815(9)	2.2933(8)
Bond angles (°)					
N1-Cu1-I1	108.23	101.92	110.42(6)	105.61(7)	102.38(7)
N1-Cu1-P1	107.80	105.44	107.53(7)	99.90(8)	112.30(8)
N1-Cu1-P2	97.65	102.72	96.09(6)	111.18(8)	102.40(7)
I1-Cu1-P1	101.50(4)	103.90(3)	101.53(2)	103.98(2)	108.71(2)
I1-Cu1-P2	113.50(4)	116.42(3)	113.09(2)	112.00(2)	111.84(2)
P1-Cu1-P2	127.13	123.80	127.60(3)	122.43(3)	118.02(3)
Torsion angles (°)					
I1-Cu1-N1-C1	40.22	32.33	43.63(18)	-8.7(2)	-179.42(15)
I1-Cu1-N1-C9	-153.27	-150.27	152.91(14)	-173.34(17)	-11.63(19)
Cu1-N1-C1-C2	168.52	179.19	164.2(2)	-162.5(2)	166.62(19)
Cu1-N1-C9-C8	-168.29	-179.71	-	165.0(2)	-165.15(18)

Table 2-2. Crystal parameters and refinement data of complexes **2-4** compared with **1**.

Complex	1-α^c	1-β^c	2	3	4
Empirical Formula	$C_{45}H_{37}ICuNP_2$	$C_{45}H_{37}ICuNP_2$	$C_{45}H_{38}CuIN_2P_2$	$C_{45}H_{38}CuIN_2P_2$	$C_{45}H_{36}CuIN_2O_2P_2$
Formula Weight	844.19	844.19	859.21	859.21	889.19
T / K	200(1)	200(1)	173(1)	168(1)	173(1)
Crystal system	Monoclinic	Monoclinic	Monoclinic	Monoclinic	Triclinic
Space group	$P2_1/c$	$P2_1/n$	$P2_1/c$ (#14)	$P2_1/c$ (#14)	$P-1$ (#2)
$a / \text{\AA}$	10.313(3)	10.0363(10)	10.2766(19)	13.4914(19)	10.7769(10)
$b / \text{\AA}$	18.345(5)	35.870(4)	18.110(3)	10.8989(14)	11.7920(9)
$c / \text{\AA}$	20.464(5)	11.5526(10)	20.848(4)	25.891(4)	15.6507(11)
$\alpha / ^\circ$	90	90	90	90	95.838(4)
$\beta / ^\circ$	93.496(3)	114.936(3)	95.416(2)	93.5911(17)	92.406(5)
$\gamma / ^\circ$	90	90	90	90	90.162(6)
$V / \text{\AA}^3$	3864.03(16)	3771.2(7)	3862.7(12)	3799.6(9)	1976.8(3)
Z	4	4	4	4	2
$R_1 (I > 2.00s(I))^a$	0.0541	0.0353	0.0375	0.0412	0.0388
wR_2^b	0.1450	0.0944	0.0616	0.0873	0.0933

2-2-3. Luminescence Measurements

The luminescence spectrum of each crystal sample was measured with a JASCO FR-6600 spectrofluorometer at room temperature and 77 K. Luminescence quantum yields were obtained using a Hamamatsu Photonics C9920-02 absolute photoluminescence quantum-yield measurement system, equipped with an integrating sphere-apparatus and a 150 W CW Xe light source. Emission lifetimes were determined with a Hamamatsu Photonics C4334 system, equipped with a streak camera as the photodetector and a nitrogen laser as the excitation light source ($\lambda_{\text{ex}} = 337 \text{ nm}$). The sample temperature was controlled with a liquid N_2 cryostat (Optistat-DN optical Dewar and ITC-503 temperature controller, Oxford Instruments). The emission decays were analyzed using two exponentials; that is, $I = A_1 \exp(-t/\tau_1) + A_2 \exp(-t/\tau_2)$, where τ_1 and τ_2 are the lifetimes, and A_1 and A_2 are the pre-exponential factors. The average lifetimes (τ_{av}) were used for the determination of the radiative and nonradiative rate constants using Equation (1) for the two exponential decay components:^[36]

$$\tau_{av} = (A_1\tau_1^2 + A_2\tau_2^2) / (A_1\tau_1 + A_2\tau_2) \quad \text{Eq. 2-1}$$

2-2-4. Theoretical Calculations

TD-DFT calculations were performed with the B3LYP functional,^[41,42] the SDD basis set for Cu and I,^[43,44] and the 6-31G** basis set for the other atoms,^[45,46] using Gaussian 09W.^[47] Atomic coordinates determined for the individual molecular structures by X-ray diffraction crystallographic analysis were used for the DFT calculations. MO diagrams for all of the complexes were reproduced using GaussView 5.0.^[48]

2-3. Results and discussion

2-3-1. Crystal Structures

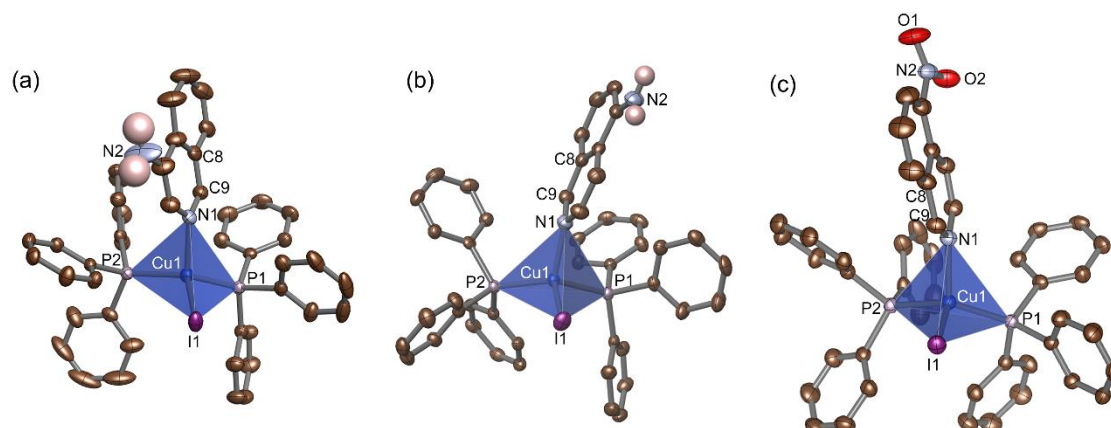


Figure 2-1. Molecular structures of (a) **2**, (b) **3**, and (c) **4**. Hydrogen atoms bound to C atom are omitted for clarity. Coordination spheres of Cu(I) ions are shown as blue tetrahedrons. Brown, light blue, red, pale purple, and dark purple ellipsoids represent C, N, O, P, and I atoms, respectively. H atoms bound to N atom are shown as pink balls and the other H atoms are omitted for clarity. Displacement parameters are drawn at the 50% probability level.

Single crystals of complexes **2** to **4** were successfully obtained by normal solution reactions, followed by the widely used vapor-diffusion method. The molecular structures of the complexes, determined by X-ray diffraction crystallographic analysis, are shown in Figure 2-1. Selected bond lengths and angles are shown in Table 2-1. Each Cu^I ion in all of the three complexes has a tetrahedral coordination geometry, occupied by an iodide anion, one N atom from the isoquinoline derivatives (4-aiq, 5-aiq, and 5-niq for complexes **2**, **3**, and **4**, respectively), and two P atoms from the two PPh₃ ligands.

Complexes **2** and **3** were crystallized in the same space group as complex **1** bearing the unsubstituted isoquinoline ligand, but complex **4**, bearing the 5-niq ligand, crystallized in a different triclinic *P*-1 space group (Table 2-2). This is probably because of the effective π - π stacking interaction between the two adjacent molecules of 5-niq ligands in **4** (Figure 2-2), whereas the isoquinoline ligands of complexes **1** and **2** do not form any intermolecular π - π stacking interaction. The 5-aiq ligand in complex **3** also forms intermolecular π - π stacking interactions, as well as in complex **4**, but the two planar 5-aiq ligands overlap only at the outside edge of isoquinoline (Figure 2-2), indicating that the interaction would be less effective than that of **4**. The functionalization of the isoquinoline ligand produces several noteworthy effects on the molecular structure: The Cu1–N1 bond length of **2** becomes longer, by ca. 0.016 Å, than that of **1**, whereas it becomes shorter, by ca. 0.025 and 0.016 Å, in complexes **3** and **4**, respectively. The P1–Cu1–P2 bond angles of complexes **3** and **4** are remarkably smaller than that of **1**, whereas the bond angle is comparable with that of **2**. The torsion angle between I–Cu and the isoquinoline derivatives of complex **2** is comparable with

that of **1**, but those of **3** and **4** are close to 180° or 0° . These differences clearly indicate that the effects of functionalization of the 4- and 5-positions are different. The functionalization at the 5-position of isoquinoline not only forms intermolecular interactions around the isoquinoline ligand, but also distorts the tetrahedral coordination structure of the CuI ion. In contrast, the functionalization at the 4-position of the isoquinoline affects the coordination environment of Cu^{I} , but does not induce notable intermolecular interactions, probably because the functional group at the 4-position is located inside the molecule. Such intermolecular interactions in complexes **3** and **4** form a more tightly packed structure than in **2**, because the molecular volume of complex **3** (estimated from V/Z to be 950 \AA^3) is smaller than that of complex **2** (966 \AA^3) and is comparable with that of the unmodified isoquinoline complex **1- β** (944 \AA^3), despite the introduction of an amino group at the 5-position of the isoquinoline ligand. In addition, the cell volume of complex **2** is comparable with that of another polymorph, **1- α** , despite the introduction of an amino group to the isoquinoline ligand, indicating looser crystal packing in **1- α** than in the others.

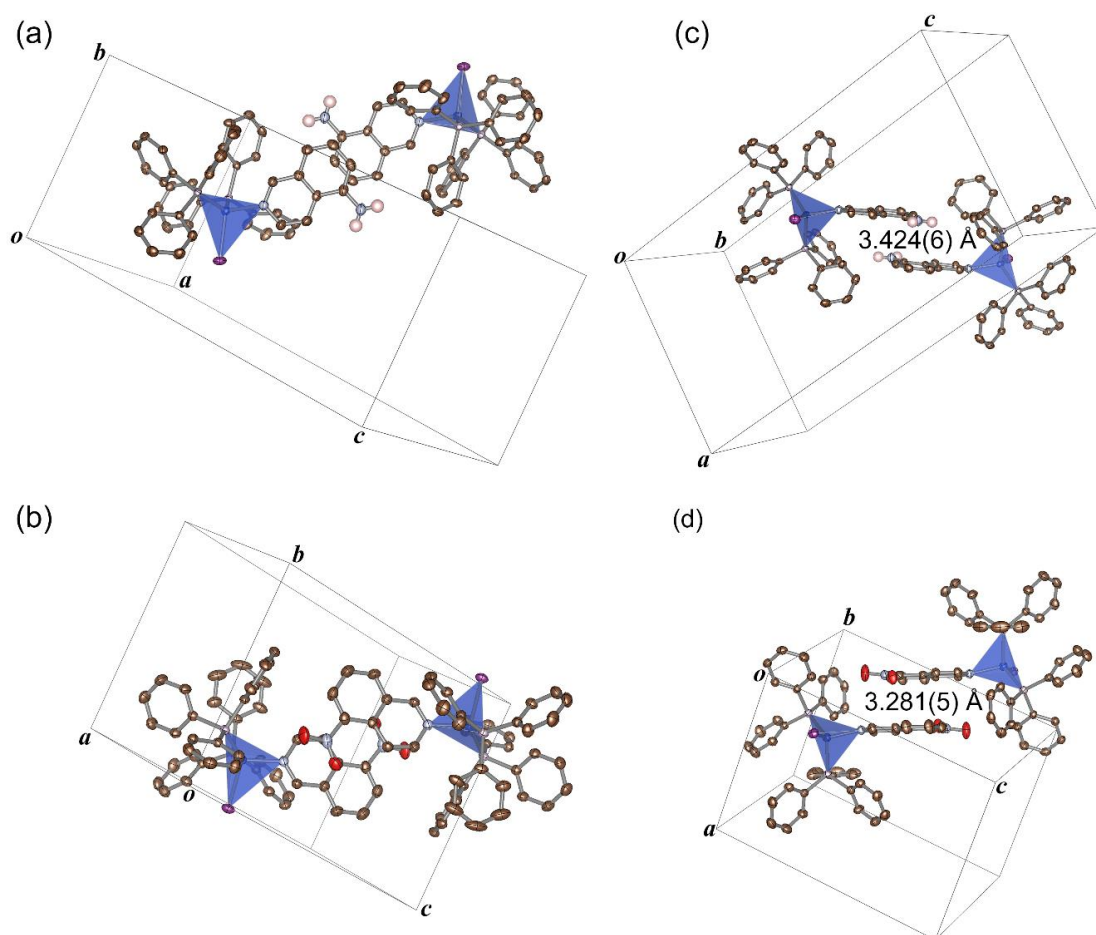


Figure 2-2. Packing diagram of complexes (a, c) **3** and (b, d) **4**. Hydrogen atoms bound to C atom are omitted for clarity, but H atoms bound to N atom are shown as pink balls. Coordination spheres of Cu(I) ions are shown as blue tetrahedrons. Brown, light blue, red, pale purple, and dark purple ellipsoids represent C, N, O, P, and I atoms,

respectively. Displacement parameters are drawn at the 50% probability level.

2-3-2. Mechanochemical and Thermal Syntheses

The complexes were additionally synthesized by the mechanochemical method, one of the most commonly and widely used synthetic techniques, using a minimum amount of solvent.

Figure 2-3 shows the powder X-ray diffraction (PXRD) patterns of ground samples containing CuI, PPh₃, and the isoquinoline derivatives. Ohara et. al have already reported the mechanochemical synthesis of **1**, without using any assisting solvent.^[32] In contrast, as shown by the PXRD measurements (the brown lines **2R**, **3R**, and **4R** in Figure 2-3), no reaction occurs in the absence of an assisting solvent in the mechanochemical syntheses of **2–4**. This is probably because the melting points of the functionalized isoquinolines (m.p. 107–113, 125–128, and 106–109 °C for 4-aiq, 5-aiq, and 5-niq, respectively) are much higher than that of unsubstituted isoquinoline (m.p. 26–28 °C), resulting in the absence of an actual solvent to promote the reaction. On the other hand, the PXRD

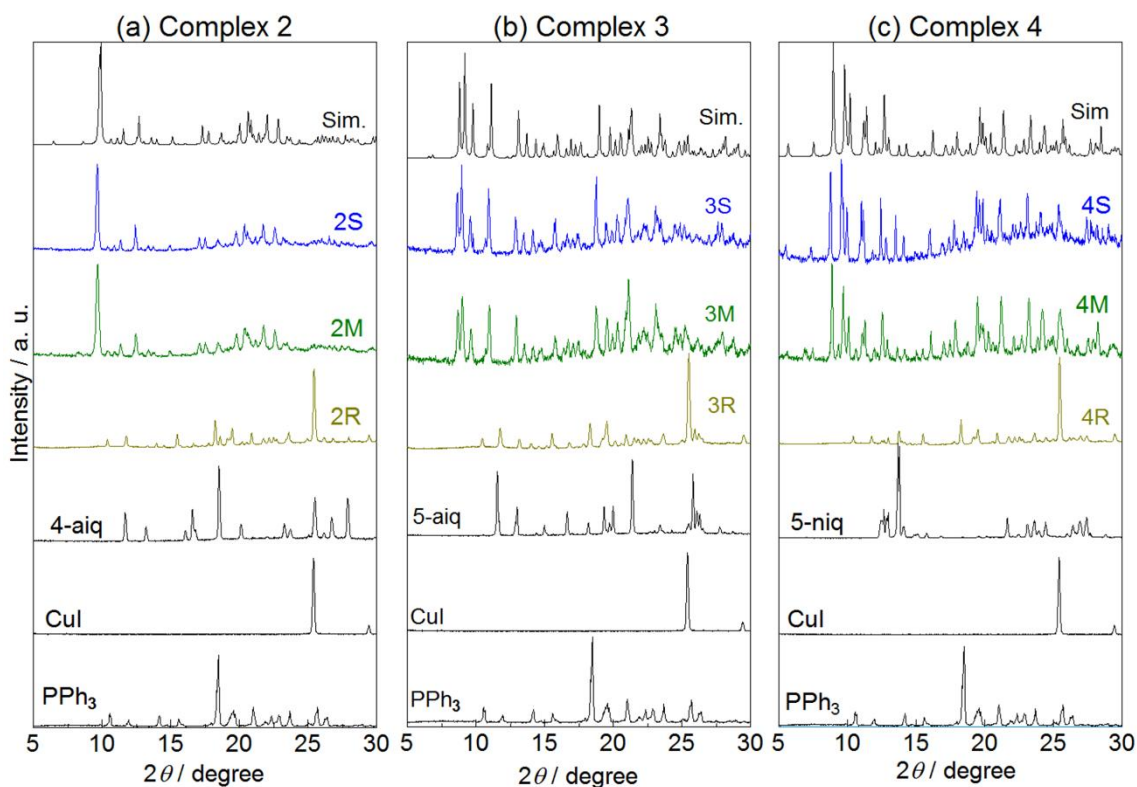


Figure 2-3. PXRD patterns of complexes **2**, **3**, and **4** synthesized by normal reactions in the solution state (**S**), manual grinding with 4 drops of PhCN (**M**), and without using an assisting solvent (**R**). Molar ratios of the starting materials used in these measurements are the same as reported in the experimental section. The top pattern of each panel shows the simulation calculated from the X-ray structure.

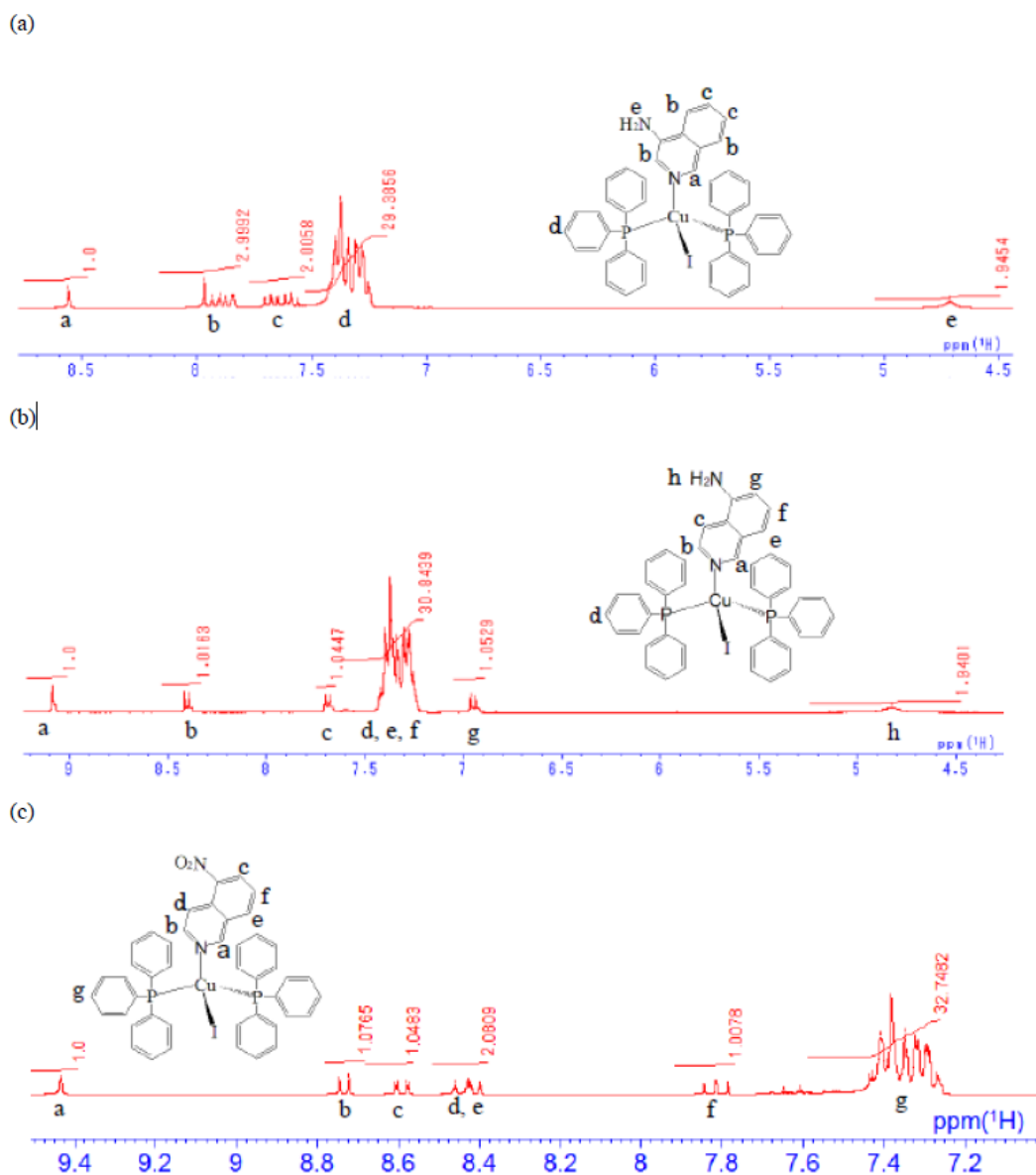


Figure 2-4. ^1H NMR spectra of the CD_3CN solutions of (a) 2M, (b) 3M, and (c) 4M patterns of the ground reaction mixture drastically change in the presence of four drops of PhCN (the green lines 2M, 3M, and 4M shown in Figure 2-3).

Notably, the observed PXRD patterns of the ground mixtures are almost identical to those of complexes prepared by the normal solution method (the blue lines 2S, 3S, and 4S shown in Figure 2-3) and the simulation patterns calculated from the X-ray diffraction structures of 2, 3, and 4, indicating that these three Cu^{I} mononuclear complexes were successfully synthesized by the mechanochemical method in the presence of PhCN as the assisting solvent, as well as by the normal solution reaction.

These results are consistent with those reported in our previous paper; that is, good solvents for CuI (e.g., PhCN and CH_3CN) effectively promote the mechanochemical reaction, producing CuI luminescent complexes.^[34] The purity of the obtained samples was confirmed by elemental analysis (Exp. Sect.), and the ^1H NMR spectra (Figure 2-

4) are identical to those of the complexes obtained by the normal solution method.

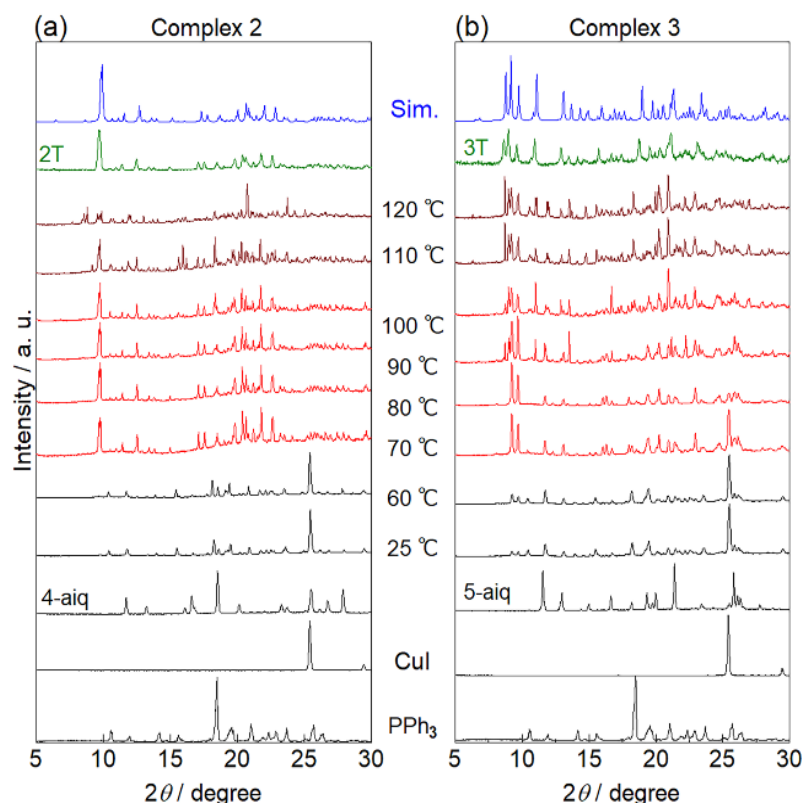


Figure 2-5. Temperature dependences of PXRD patterns of the ground mixtures of CuI, PPh₃ (4 equiv for **2T** and 3 equiv for **3T**), and (a) 4-aiq or (b) 5-aiq (2 equiv each). Blue and green lines show the simulation and observed patterns of thermally synthesized samples **2T** and **3T**, respectively.

As mentioned above, the melting point of the ligands is one of the important factors in mechanochemical synthesis. These results motivated us to investigate the thermal syntheses of luminescent Cu^I complexes **2** and **3** (the luminescence properties are discussed in the next section) in the solid state, without using any assisting solvent. In these syntheses, a mixture of CuI, PPh₃, and the isoquinoline derivative (4-aiq or 5-aiq) was first ground in the absence of any assisting solvent at room temperature (note that no reaction occurs at this point, as shown in Figure 2-3). Figure 2-5 shows the temperature dependence of the PXRD patterns of the ground mixtures. At 25 °C, each sample

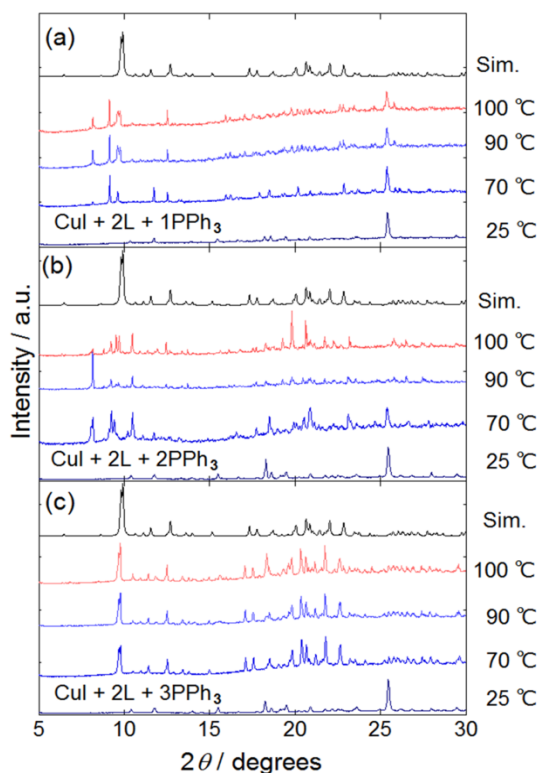


Figure 2-6. Temperature dependence of the PXRD patterns of the ground mixtures of CuI, 4-aiq (2 equiv), and PPh₃ (a) 1 equiv, (b) 2 equiv, and (c) 3 equiv. The top line in each panel shows the simulation pattern of complex **2**.

exhibited a strong diffraction peak at 25.4°, derived from the unreacted CuI solid, indicating that the reaction to synthesize complexes **2–4** hardly occurs just by manual grinding at room temperature. These PXRD patterns of ground mixtures drastically change above 70 or 80 °C; the diffraction peak of CuI completely disappears above 70 °C for the mixture containing 4-aiq and 80 °C for the mixture containing 5-aiq. Notably, the observed patterns of the mixture containing 4-aiq in the temperature region 70–100 °C qualitatively agree with the simulation pattern calculated from the X-ray diffraction structure of **2**, indicating that complex **2** was successfully obtained by simple heating of the ground mixture. Above 110 °C, the mixture containing 4-aiq shows further changes, indicating further structural transformation or decomposition. On the other hand, the PXRD pattern of the mixture containing 5-aiq in the temperature region 70–100 °C is different from the simulation pattern obtained for complex **3**, but above 110 °C, the PXRD pattern qualitatively agrees with the pattern obtained from the simulation. These results clearly indicate that the temperature required to form the mononuclear CuI complex [CuI(PPh₃)₂L] strongly depends on the ligand L. This can be attributed to 5-aiq having a higher melting point than 4-aiq.

Next, the effect of the amount of PPh₃ on the thermal synthesis of complex **2** was investigated, because complex **2** was successfully obtained by heating at or near the melting point of the PPh₃ ligand. As shown in Figure 2-6a, with the addition of only 1 equiv. of PPh₃ to CuI, the characteristic peak derived from the unreacted CuI is clearly

observed, even above the melting point of PPh₃ (> 80 °C). This peak completely disappears when > 2 equiv. of PPh₃ is used in the thermal synthesis, as shown in Figures 2-6b, 2-6c. However, although 2 equiv. of PPh₃ (i.e., the ideal molar ratio to synthesize complex **2**) is used for the thermal synthesis of complex **2**, the observed PXRD pattern does not match that obtained from the simulation of complex **2** (Figure 2-6b), indicating that another species might have been produced. In contrast, an almost-identical PXRD pattern to that of the simulation is clearly observed for the ground mixture containing 3 equiv. of PPh₃ (Figure 2-6c). Thus, the amount of PPh₃ ligand is one of the crucial parameters for the synthesis of mononuclear complex **2** with a high purity. Such an excess amount of PPh₃ prevents the formation of the dinuclear complex [Cu₂I₂(PPh₃)₂L₂] in a 1:1:1 ratio.

TG-DTA analyses of the ground mixtures of CuI, PPh₃, and the isoquinoline derivatives were also conducted to obtain more insight about the thermal syntheses of complexes **2** and **3**. TG-DTA analysis of a mixture of CuI, PPh₃, and the unmodified isoquinoline was also conducted as the reference. As shown in Figure 2-7, all of the three mixtures show a negligibly small mass change (< 5 %) in the temperature region below 125 °C, indicating that most of the reagents used in these thermal syntheses are still

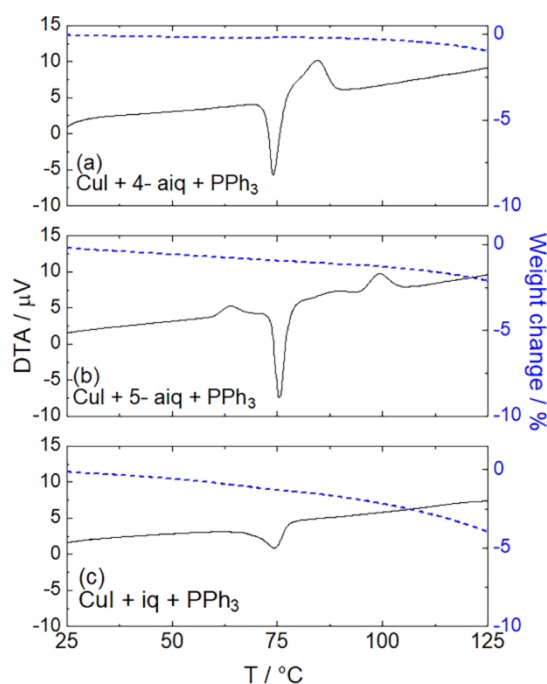


Figure 2-7. TG (dotted lines) and DTA (solid lines) curves of the ground mixtures of CuI, PPh₃, and (a) 4-aiq, (b) 5-aiq, and (c) iq (molar ratios of CuI: PPh₃:L = 1:4:2) under Ar flow (flow rate: 250 mL/min).

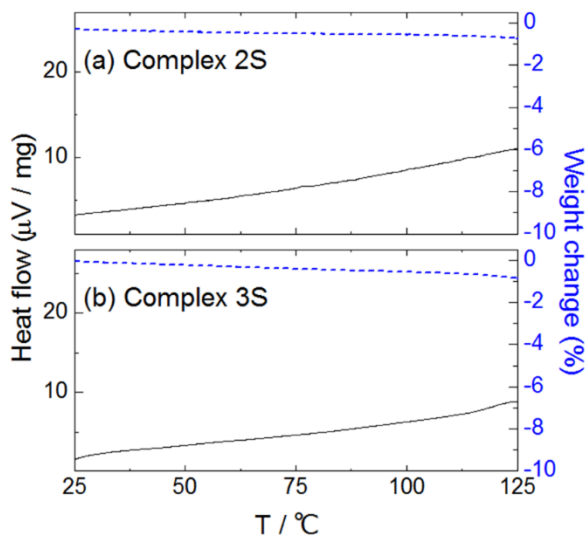


Figure 2-8. TG (blue dotted lines) and DTA (black solid lines) curves of **2S**, and **3S**.

present in this temperature range. Please note that the complexes obtained by the normal solution method (**2S** and **3S**) do not show any phase transition or decomposition in this temperature range (Figure 2-8). Several interesting features are observed in the DTA curves: one endothermic peak is clearly and commonly observed at ca. 70 °C for all of the three mixtures. This can be attributed to the solid–liquid phase transition of the PPh₃ ligand (the m.p. of pure PPh₃ is 80 °C). A slight deviation from the melting point of PPh₃ can be attributed to it mixing with the isoquinoline derivative, because almost-identical endothermic peaks are observed for the mixtures of PPh₃ and the isoquinoline derivatives (Figure 2-9). Notably, a clear exothermic peak is observed for the mixtures containing 4-aiq, just above the melting point of PPh₃. Similar exothermic peaks are observed for the mixtures containing 5-aiq, but the temperatures where the peaks are observed are moderately different. Because drastic changes in the PXRD patterns are commonly observed between 60 and 80 °C for these two mixtures containing amino-functionalized isoquinolines, these exothermic peaks can be attributed to the heat of formation of the complex. This is also supported by the fact that no exothermic peak is observed for the mixture containing the unmodified/8/32d isoquinoline; that is, the formation of complex **1** is already completed by the manual grinding of the mixture at room temperature.^[32] Although I have not identified the complexes formed between 70 and 100 °C in the thermal synthesis of complex **3**, these PXRD and TG-DTA data clearly indicate the importance of the PPh₃ ligand melting. In other words, the formation of complexes **2** and **3** at temperatures above the melting point of PPh₃ occurs by dissolving the other two starting materials (CuI and L) in the melted PPh₃. This is also supported by the TG DTA results: exothermic peaks are observed for the mixtures composed of PPh₃ and CuI (Figure 2-9).

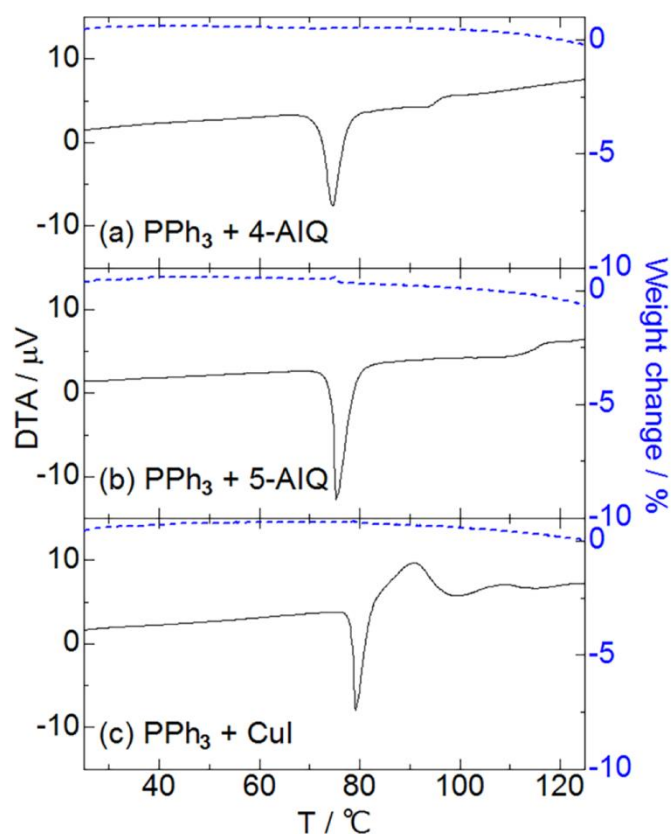


Figure 2-9. TG (blue dotted lines) and DTA (black solid lines) curves of mixtures of PPh₃ and (a) 4-AIQ, (b) 5-AIQ, or (c) CuI.

2-3-3. Photophysical Properties

As reported in our previous paper, complex **1**, bearing an unmodified isoquinoline ligand, exhibits interesting luminescence properties that strongly depend on the crystal polymorphs; one polymorph of complex **1- α** (the space group is $P2_1/c$) exhibits a broad emission band centered at 535 nm, whereas the characteristic vibronic structure was observed at a comparable wavelength for another polymorph **1- β** (the space group is $P2_1/n$).^[35] Although I temporarily assumed that such a dependence could be due to the slight difference in the crystal packing between **1- α** and **1- β** , indicating that the isoquinoline complex has comparable energy levels of $^3\pi\pi^*$ and $^3\text{MLCT}$ states, to obtain more information, several photophysical measurements were conducted for complexes **2–4** containing isoquinoline derivatives. As shown in Figure 2-10, complexes **2** and **3** exhibit yellow and orange emissions under UV-light irradiation, but complex **4**, bearing a nitro group attached to the isoquinoline ligand, hardly shows any emission.

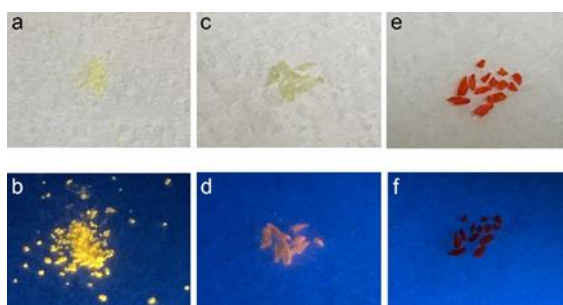


Figure 2-10. Photographs under bright field (upper) and UV light (lower) of sample **2S** (a and b), **3S** (c and d), and **4S** (e and f).

In the emission spectra (Figure 2-11), complex **2** shows the emission maximum at 543 nm with vibronic progressions, whereas complex **3** exhibits broad orange emission bands at ca. 584 nm and 611 nm. At 77 K, the emission band positions of these two complexes are almost unchanged, but the vibronic structures are clearly observed, not only in the emission spectrum of complex **2**, but also in that of complex **3**. The characteristic vibronic structures clearly indicate that the emission of complexes **2** and **3** are assignable to the phosphorescence from the ligand-centered $^3\pi\pi^*$ excited state, as in the case of complex **1- β** . The emission lifetimes and quantum yields of these complexes were also measured at 298 and 77 K. The obtained photophysical parameters are summarized in Table 2-3, along with those for complexes **1- α** and **1- β** . The relatively long emission lifetimes (in the range of milliseconds at both 298 and 77 K, Figure 2-13) and small radiative rate constants (k_r is in the order of several 10^1 s^{-1}) also indicate the strongly forbidden phosphorescence of the organic ligands. Because of lower k_r values of complexes **2** and **3**, their emission quantum yields decrease, compared with that of complex **1- β** . This is also supported by the comparable nonradiative rate constants (k_{nr} , Table 2-3).

To further investigate the photophysical properties, density functional theory (DFT) calculations were performed for four complexes, **1- β** , **2**, **3**, and **4**. In these calculations, the molecular structures determined by X-ray diffraction structure analysis were used without further optimization to investigate the photophysical property in the solid state. The simplified molecular orbital (MO) diagram is shown in Figure 2-12. The highest occupied MO (HOMO) of each complex is mainly composed of the 5p orbital of the iodide anion and 3d orbital of the Cu^{I} cation. Similar characteristics are also observed in the HOMO-1 and HOMO-2 diagrams of all of the four complexes (Figures 2-14 to 2-17). The energies of these orbitals are slightly destabilized ($< 0.1 \text{ eV}$) by the introduction of an amino group and stabilized (ca. 0.15 eV) by the introduction of a nitro group to the isoquinoline ligand, probably because of the electron-donating and -withdrawing nature of these functional groups, respectively. In other words, the amino-functionalized isoquinoline ligand has a stronger σ -donating ability, resulting in a larger ligand-field splitting of the Cu^{I} center (vice versa). The LUMO and LUMO-1 of each complex are commonly delocalized on the π^* orbital of the isoquinoline ligand in all of

the four complexes. The timedependent DFT (TD-DFT) calculations for these complexes (Tables 2-4 to 2-7) indicate that the lowest singlet excited state can be mainly attributed to the HOMO–LUMO transition; that is, the MLCT transition combined with the XLCT transition [$^1(\text{M}+\text{X})\text{LCT}$]. Notably, the LUMO of complex **4** is remarkably more stabilized, by ca. 1.2 eV, than the parent complex **1**, resulting in the lowest energy gap between the HOMO and LUMO among the four complexes. In contrast, the LUMOs of **2** and **3** are destabilized, by ca. 0.25 eV, by the introduction of an amino group to the isoquinoline ligand. These trends are reasonable, because the nitro group in complex **4** is a well-known electron-withdrawing group, whereas the amino groups in complexes **2** and **3** are electron-donating in nature. In fact, complex **4** exhibits absorption bands (< 560 nm) in the UV/Vis diffuse reflectance spectrum in a longer wavelength region than those observed for complexes **2** and **3** (< 450 nm, Figure 2-18). Thus, such a small

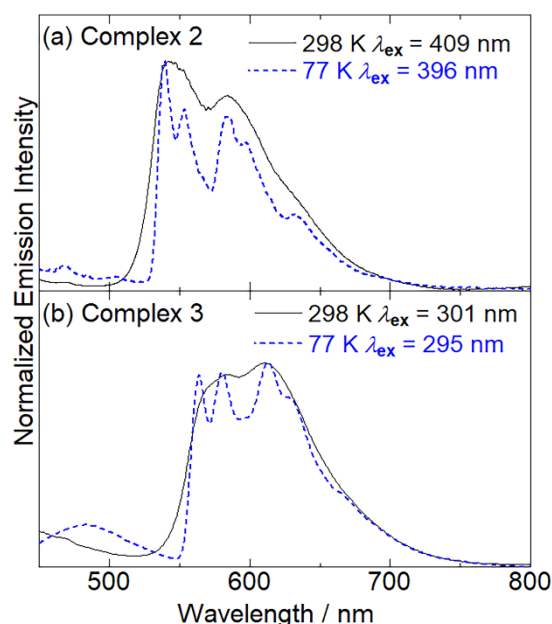


Figure 2-11. Emission spectra of complexes (a) **2** and (b) **3** in the solid state at 77 K (blue dotted lines) and 298 K (black solid lines).

HOMO–LUMO energy gap for complex **4** is one of the possible origins of its nonemissive nature. Another interesting result is that the highest occupied π orbital of the isoquinoline ligand is commonly observed at HOMO-5 for emissive complexes **1**–**3**, but the energies of complexes **2** and **3** are remarkably higher, by ca. 0.80 and 0.91 eV, respectively, than that of complex **1**. This difference indicates that the $\pi\pi^*$ excited states of complexes **2** and **3** are stabilized, compared with that of complex **1**, by the introduction of an electron-donating amino group to the isoquinoline ligand. Because the singlet–triplet stabilization energies of $\pi\pi^*$ states are generally larger than those

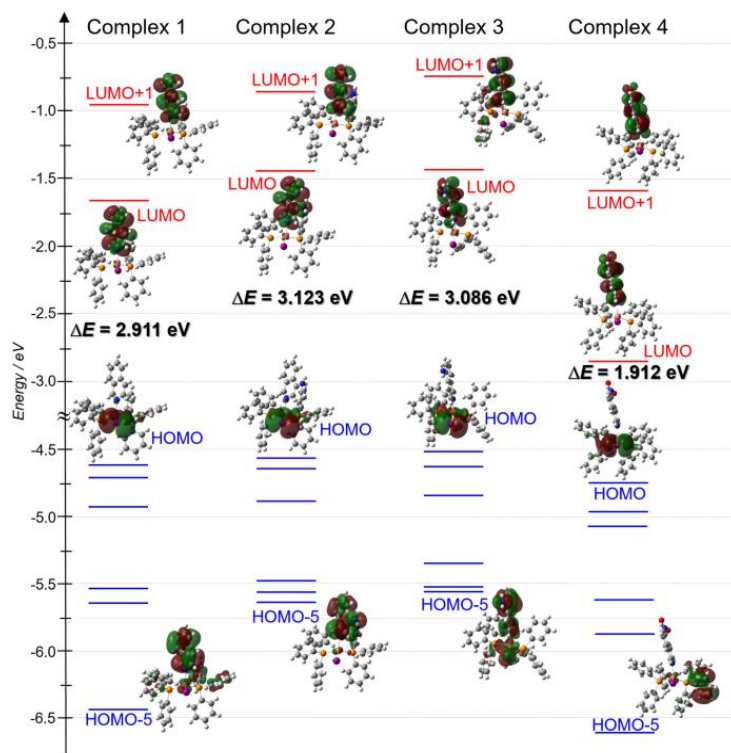


Figure 2-12. MO diagrams and orbital shapes of complexes **1–4**. The molecular structures determined by X-ray analysis were used for these DFT calculations. The energy differences (ΔE) between the HOMO and LUMO energies are also shown.

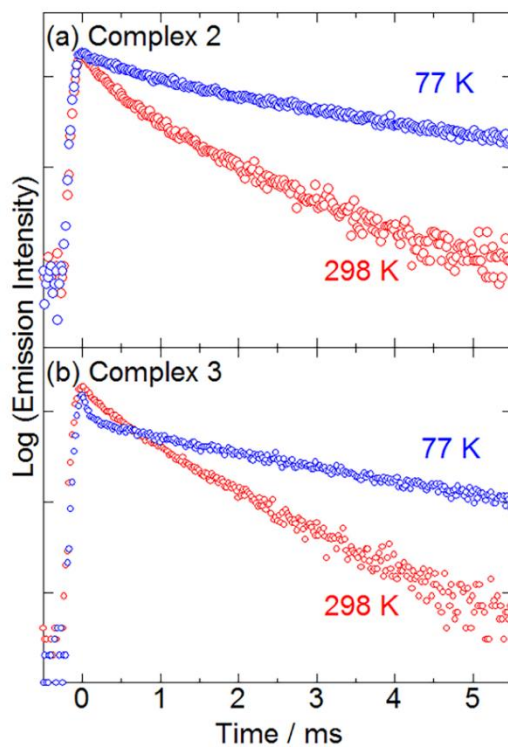
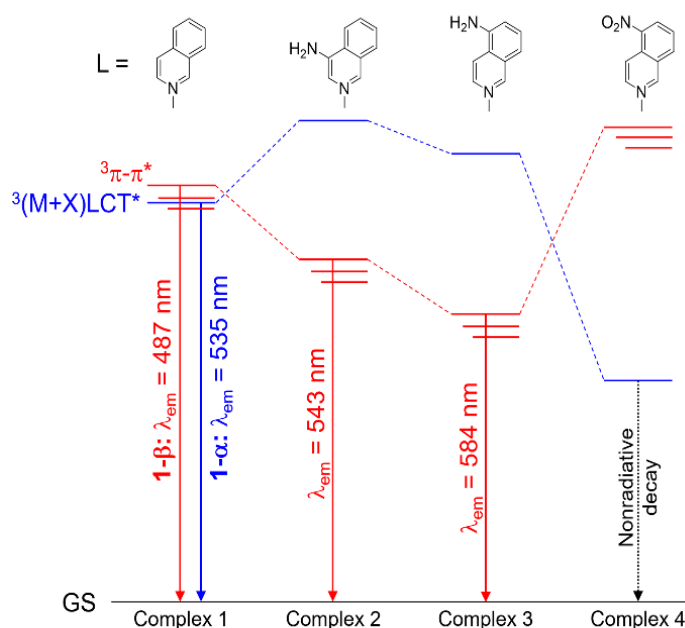


Figure 2-13. Emission decay of the complexes **2** and **3** in the solid state ($\lambda_{\text{ex}} = 337$ nm).

of the MLCT states, the $^3\pi\pi^*$ emission for complexes **2** and **3** is reasonable. Further,

the trend in the $^3\pi\pi^*$ emission energies is qualitatively consistent with the result of the emission wavelength of these complexes; the highest $^3\pi\pi^*$ emission band energy decreases in the order $1 > 2 > 3$ (Table 2-3). Scheme 2-2 shows the schematic energy diagram for all of the four complexes, thus exhibiting the effect of the introduction of the functional groups to the isoquinoline ligand on the photophysical properties of the parent complex **1**. As suggested by the TD-DFT calculations and emission spectral measurements, the $^3\pi\pi^*$ emissive states of complexes **2** and **3**, which are localized on the isoquinoline ligand, are stabilized by the introduction of an electron-donating amino group, whereas their (M+X)LCT states are inversely destabilized. The smaller k_r values of these complexes, compared with that of complex **1- β** , can be attributed to the larger energy gap between these two states. In contrast, the nitro group attached to the 5-position of the isoquinoline ligand significantly stabilizes the (M + X)LCT states of complex **4**, resulting in rapid nonradiative deactivation from the photoexcited state.



Scheme 2-2. Schematic energy diagram for the excited states of complexes **1–4**. Sublines for $^3\pi-\pi^*$ state schematically represent the contribution of vibrational levels.

Table 2-3. Luminescence properties of complexes **2** and **3** in the crystals at 77 K and 298 K.

Complex	1-α^e		1-β^e		2		3	
T / K	298	77	298	77	298	77	298	77
λ_{\max} (nm)	535	486, 521, 561, 610	487, 520, 558	484, 496, 520, 532, 561, 607	543, 584	539, 553, 583	584, 611	564, 580, 613
τ_1^a (ms) (A_1) ^a	$2.7 \cdot 10^{-2}$ (0.54)	$1.23 \cdot 10^{-1}$ (0.94)	0.079 (0.74)	0.126 (0.86)	0.341 (0.917)	0.436 (0.55)	0.302 (0.98)	0.263 (0.20)
τ_2^a (ms) (A_2) ^a	$7.7 \cdot 10^{-2}$ (0.52)	$5.34 \cdot 10^{-1}$ (0.18)	0.493 (0.30)	0.777 (0.23)	1.178 (0.339)	3.271 (0.452)	0.948 (0.75)	2.748 (0.47)
τ_{av}^b (ms) Φ	0.065 0.63	0.31 0.51	0.376 0.65	0.528 0.50	0.810 0.024	2.875 0.199	0.758 0.024	2.651 0.127
k_r^c (s ⁻¹)	$9.8 \cdot 10^3$	$1.6 \cdot 10^3$	$1.7 \cdot 10^3$	$9.5 \cdot 10^2$	$3.0 \cdot 10^1$	$6.9 \cdot 10^1$	$3.2 \cdot 10^1$	$4.8 \cdot 10^1$
k_{nr}^d (s ⁻¹)	$5.7 \cdot 10^3$	$1.6 \cdot 10^3$	$9.3 \cdot 10^2$	$9.5 \cdot 10^2$	$1.2 \cdot 10^3$	$2.8 \cdot 10^2$	$1.3 \cdot 10^3$	$3.3 \cdot 10^2$

[a] Emission lifetime. Emission decays were analyzed with two components: $I = A_1 \exp(-t/\tau_1) + A_2 \exp(-t/\tau_2)$.

[b] Emission lifetime. Average emission lifetimes determined from Eq. (1). [c] Radiative rate constants $k_r = \phi/\tau_{av}$. [d] Nonradiative rate constants $k_{nr} = k_r(1 - \phi) / \phi$. [e] Ref. [35], for **1- α** and **1- β** .

Table 2-4. Energy, oscillator strength and major contribution of calculated transition for 1- β .

Excited state	Energy / eV (/ nm)	Oscillator strength	Major contribution (%)
1	2.3812 (520.68)	0.0030	HOMO-1 \rightarrow LUMO (2.82)
			HOMO \rightarrow LUMO (96.09)
2	2.4200 (512.34)	0.0014	HOMO-1 \rightarrow LUMO (95.14)
			HOMO \rightarrow LUMO (2.85)
3	2.6408 (469.49)	0.0032	HOMO-2 \rightarrow LUMO (97.89)
4	3.0849 (403.21)	0.0055	HOMO \rightarrow LUMO+1 (98.25)
5	3.1248 (396.77)	0.0040	HOMO-1 \rightarrow LUMO+1 (95.97)
6	3.2309 (383.74)	0.0139	HOMO-4 \rightarrow LUMO (51.47)
			HOMO-3 \rightarrow LUMO (44.09)
7	3.3069 (374.93)	0.0144	HOMO-4 \rightarrow LUMO (43.78)
			HOMO-3 \rightarrow LUMO (52.30)
8	3.337 (371.51)	0.0025	HOMO-2 \rightarrow LUMO+1 (97.55)
9	3.4517 (359.20)	0.0083	HOMO \rightarrow LUMO+2 (96.12)
10	3.477 (356.50)	0.0061	HOMO \rightarrow LUMO+3 (81.85)
			HOMO \rightarrow LUMO+4 (11.19)

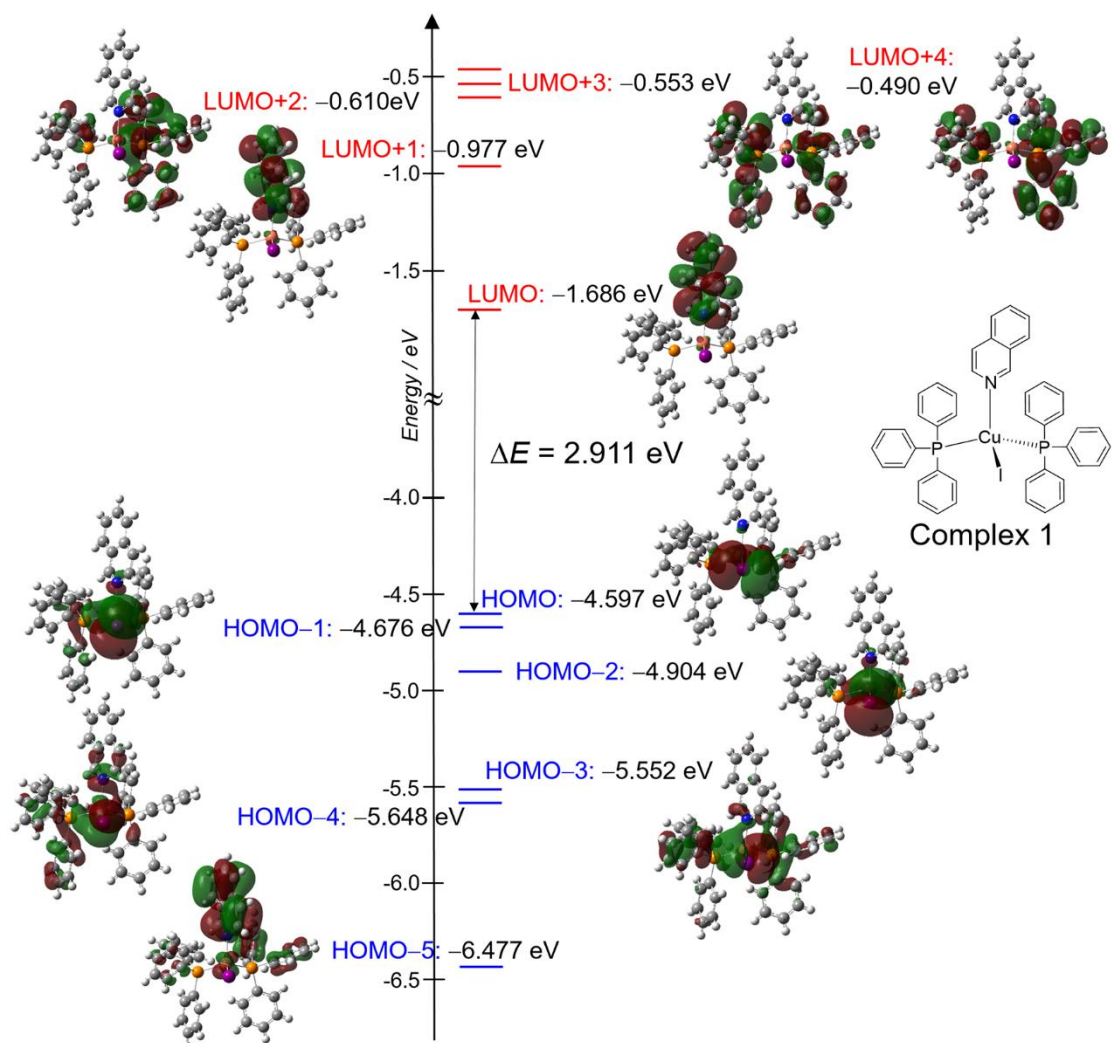


Figure 2-14. Molecular orbital energy diagram and schematic representations of the relevant molecular orbitals of **1**. Molecular structure of **1- β** determined by X-ray analysis was used.

Table 2-5. Energy, oscillator strength and major contribution of calculated transition for **2**.

Excited state	Energy / eV (/ nm)	Oscillator strength	Major contribution (%)
1	2.6161 (473.93)	0.0064	HOMO-1 → LUMO (9.27) HOMO → LUMO (89.31)
2	2.6422 (469.25)	0.0023	HOMO-1 → LUMO (88.47) HOMO → LUMO (9.38)
3	2.8797 (430.54)	0.0021	HOMO-2 → LUMO (97.52)
4	3.2176 (385.34)	0.0075	HOMO → LUMO+1 (93.68) HOMO-1 → LUMO+1 (4.65)
5	3.2557 (380.82)	0.0045	HOMO → LUMO+1 (4.87) HOMO-1 → LUMO+1 (92.24)
6	3.3862 (366.14)	0.0059	HOMO-1 → LUMO+2 (2.25) HOMO → LUMO+2 (86.19) HOMO → LUMO+3 (8.21)
7	3.4527 (359.09)	0.0108	HOMO-4 → LUMO (43.92) HOMO-3 → LUMO (36.47) HOMO-2 → LUMO+1 (11.38) HOMO → LUMO+3 (2.72)
8	3.4658 (357.73)	0.0086	HOMO-2 → LUMO+1 (4.31) HOMO-1 → LUMO+2 (80.44) HOMO → LUMO+2 (5.55) HOMO → LUMO+3 (4.59)
9	3.4788 (356.40)	0.0053	HOMO-2 → LUMO+1 (3.54) HOMO-1 → LUMO+2 (9.84) HOMO-1 → LUMO+3 (2.59) HOMO → LUMO+2 (4.32) HOMO → LUMO+3 (76.51)
10	3.488 (355.46)	0.0023	HOMO-4 → LUMO (2.51) HOMO-3 → LUMO (4.42) HOMO-2 → LUMO+1 (37.59) HOMO-1 → LUMO+3 (46.12) HOMO → LUMO+3 (4.55)

Figure 2-15. Molecular orbital energy diagram and schematic representations of the relevant molecular orbitals of **2**. Molecular structure of **2** determined by X-ray analysis was used.

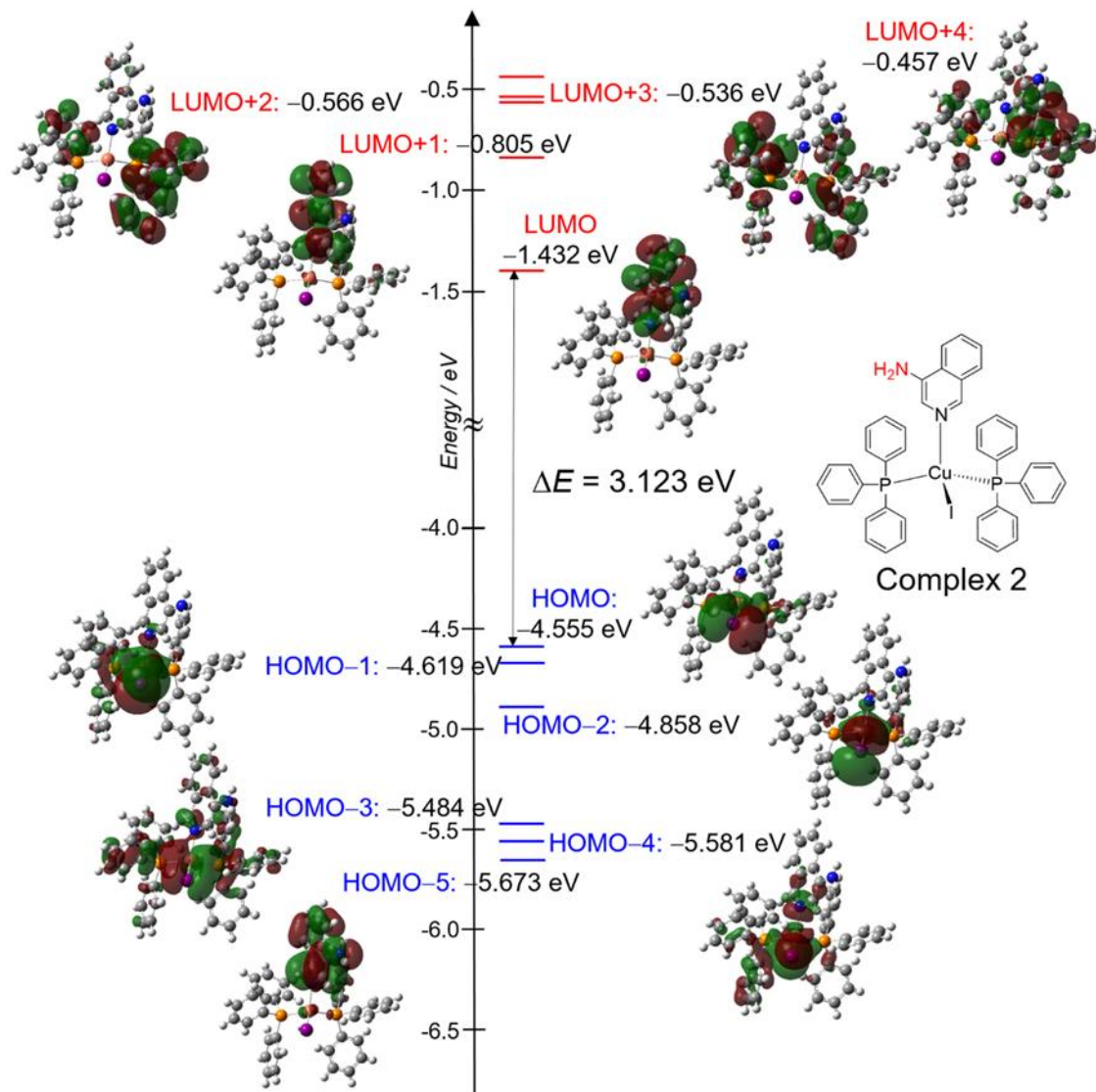


Table 2-6. Energy, oscillator strength and major contribution of calculated transition for **3**.

Excited state	Energy / eV (/ nm)	Oscillator strength	Major contribution (%)
1	2.5237 (491.29)	0.0030	HOMO → LUMO (97.44)
2	2.5928 (478.19)	0.0013	HOMO-1 → LUMO (96.54)
3	2.7706 (447.5)	0.0031	HOMO-2 → LUMO (97.76)
4	3.2094 (386.31)	0.0160	HOMO → LUMO+1 (98.22)
5	3.2819 (377.78)	0.0030	HOMO-4 → LUMO (2.28) HOMO-1 → LUMO+1 (90.58) HOMO → LUMO+2 (2.84)
6	3.3223 (373.19)	0.0175	HOMO-1 → LUMO+1 (3.41) HOMO → LUMO+2 (92.21)
7	3.3578 (369.24)	0.0019	HOMO-5 → LUMO (29.39) HOMO-4 → LUMO (62.87) HOMO-1 → LUMO+1 (2.36)
8	3.3740 (367.47)	0.0438	HOMO-5 → LUMO (2.34) HOMO-3 → LUMO (90.00)
9	3.399 (364.74)	0.0096	HOMO-1 → LUMO+2 (16.05) HOMO → LUMO+3 (77.81)
10	3.414 (363.13)	0.0009	HOMO-1 → LUMO+2 (74.52) HOMO → LUMO+3 (15.36)

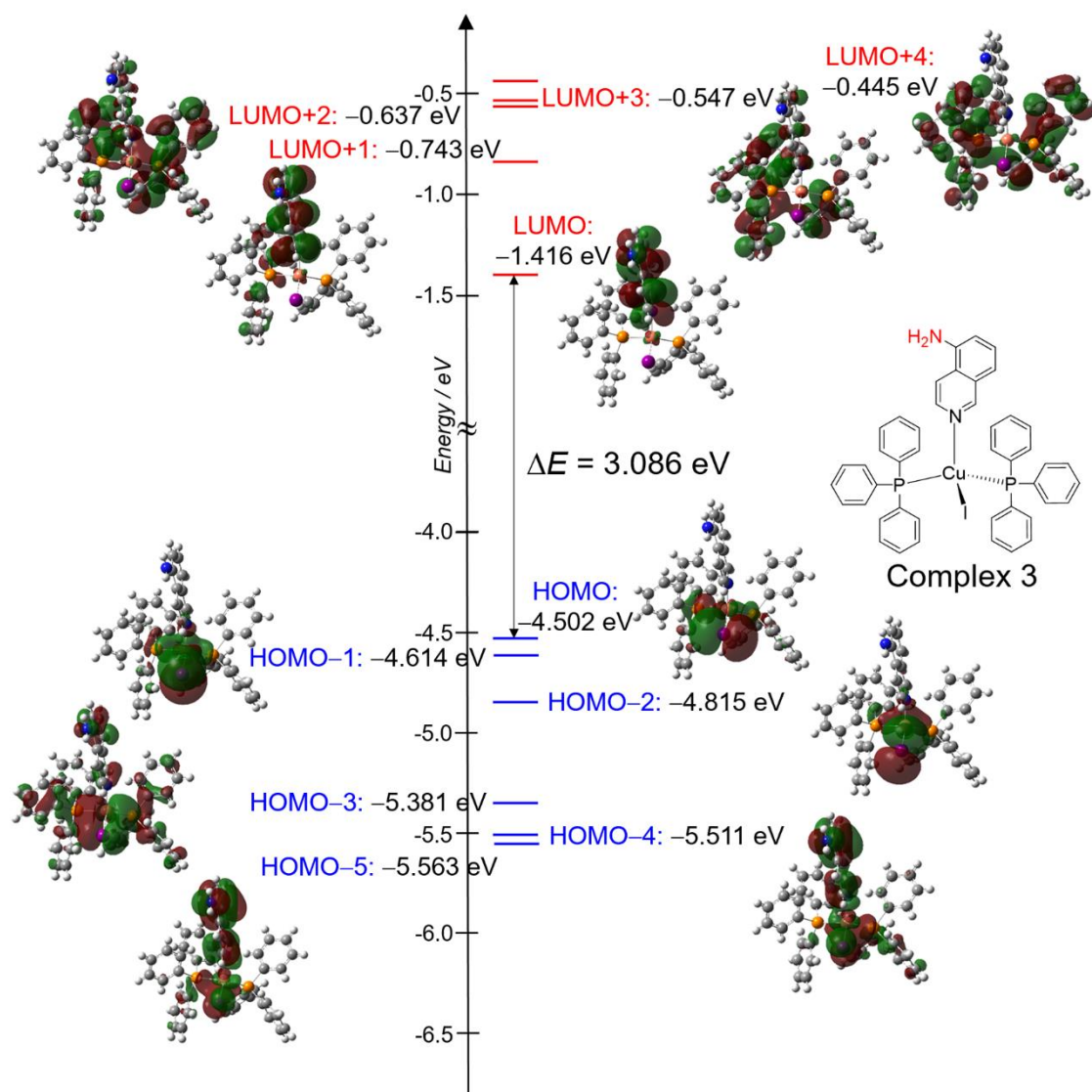


Figure 2-16. Molecular orbital energy diagram and schematic representations of the relevant molecular orbitals of **3**. Molecular structure of **3** determined by X-ray analysis was used.

Table 2-7. Energy, oscillator strength and major contribution of calculated transition for **4**.

Excited state	Energy / eV (/ nm)	Oscillator strength	Major contribution (%)	
1	1.476 (839.88)	0.0041	HOMO	→ LUMO (99.29)
2	1.658 (747.61)	0.0012	HOMO-1	→ LUMO (98.87)
3	1.793 (691.29)	0.0007	HOMO-2	→ LUMO (98.64)
4	2.3396 (529.93)	0.0046	HOMO-3	→ LUMO (98.74)
5	2.5069 (494.57)	0.0014	HOMO-4	→ LUMO (98.74)
6	2.5849 (479.65)	0.0122	HOMO	→ LUMO+1 (98.59)
7	2.7465 (451.42)	0.0011	HOMO-1	→ LUMO+1 (97.70)
8	2.868 (432.17)	0.0005	HOMO-2	→ LUMO+1 (97.41)
9	2.978 (416.27)	0.0004	HOMO	→ LUMO+2 (98.48)
10	3.162 (392.06)	0.0009	HOMO-1	→ LUMO+2 (98.10)

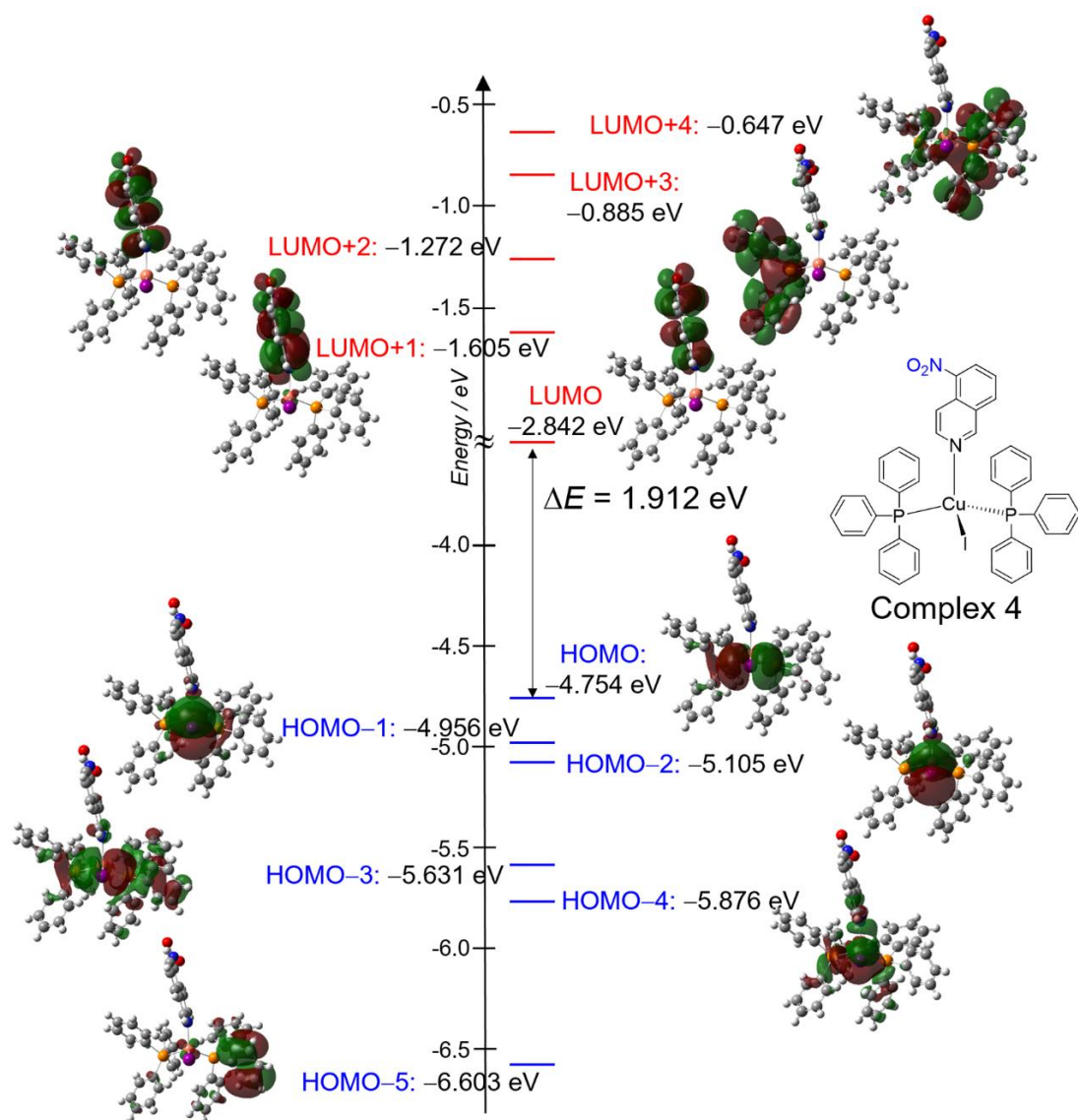


Figure 2-17. Molecular orbital energy diagram and schematic representations of the relevant molecular orbitals of **4**. Molecular structure of **4** determined by X-ray analysis was used.

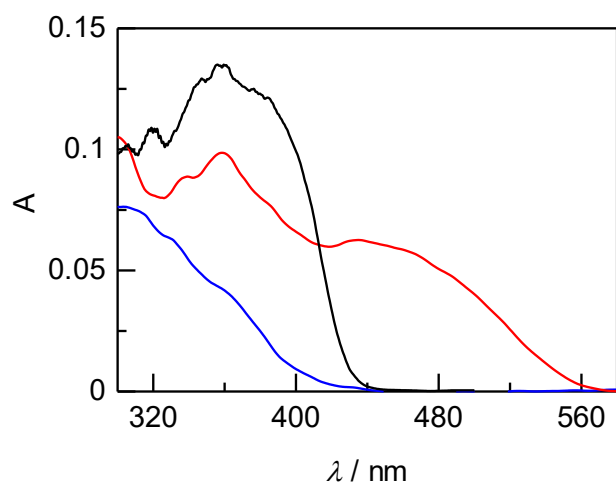


Figure 2-18. UV-Vis diffuse reflectance spectra of the complexes **2S** (blue lines), **3S** (black lines) and **4S** (red lines).

2-4. Conclusion

Three new mononuclear CuI complexes $[\text{CuI}(\text{PPh}_3)_2\text{L}]$ ($\text{L} = 4\text{-aiq}, 5\text{-aiq}, \text{and } 5\text{-niq}$) were synthesized by conventional solution reactions, mechanochemical syntheses, and newly developed thermal syntheses. The introduction of an amino or nitro group to the isoquinoline ligand significantly affected not only the luminescence properties, but also the mechanochemical synthesis. In the mechanochemical syntheses of the three functionalized isoquinoline complexes, a small amount of PhCN solvent was required to form the mononuclear complexes, whereas the parent complex with an unmodified isoquinoline complex, $[\text{CuI}(\text{PPh}_3)_2(\text{iq})]$, was synthesized mechanochemically, without the use of any assisting solvent. This contrasting result strongly indicates the importance of the melting point of the L ligand. This finding prompted us to investigate the thermal synthesis of luminescent CuI complex. Complexes **2** and **3** with aminofunctionalized isoquinoline ligands were successfully synthesized in high yields by simply heating the ground mixtures of the three starting materials (CuI, PPh₃, and L) at ca. 100 °C. Complexes **2** and **3** exhibited yellow and orange phosphorescence with ms range lifetimes originating from the ligandcentered $^3\pi\pi^*$ excited state, whereas complex **4**, with a nitrofunctionalized isoquinoline ligand, did not show any emission in the visible region. The TD-DFT calculations indicated that the introduction of an electron-donating amino group to the isoquinoline ligand stabilized the $^1\pi\pi^*$ excited state localized on the isoquinoline ligand, whereas the MLCT excited state of complex **4** was remarkably stabilized by the electron-withdrawing nature of the nitro group. Further studies to synthesize highly luminescent Cu^I complexes by the thermal synthesis method are underway.

2-5. References

- [1] B. Marsen, S. Dorn, B. Cole, R. E. Rocheleau, E. L. Miller, *Mater. Res. Soc. Symp. Proc.* 2007, 974, 0974-CC09-05.
- [2] C. L. Linfoot, M. J. Leitzl, P. Richardson, A. F. Rausch, O. Chepelin, F. J. White, H. Yersin, N. Robertson, *Inorg. Chem.* 2014, 53, 10854–1086.
- [3] M. Liu, H. Zhao, S. Chen, H. Yu, Y. Zhang, X. Quan, *Biosens. Bioelectron.* 2011, 26, 4111–4116.
- [4] N. Ayyadurai, N. S. Prabhu, K. Deepankumar, S. G. Lee, H. H. Jeong, C. S. Lee, H. Yun, *Angew. Chem. Int. Ed.* 2011, 50, 6534–6537; *Angew. Chem.* 2011, 123, 6664.
- [5] C. S. Smith, K. R. Mann, *J. Am. Chem. Soc.* 2012, 134, 8786–8789.
- [6] A. Kobayashi, M. Kato, *Chem. Lett.* 2017, 46, 154–162.
- [7] C. Bizzarri, C. Strabler, J. Prock, B. Trettenbrein, M. Ruggenthaler, C. H. Yang, F. Polo, A. Iordache, P. Brüggegger, L. D. Cola, *Inorg. Chem.* 2014, 53, 10944–10951.
- [8] T. Hofbeck, U. Monkowius, H. Yersin, *J. Am. Chem. Soc.* 2015, 137, 399–404.
- [9] R. Czerwieniec, J. Yu, H. Yersin, *Inorg. Chem.* 2011, 50, 8293–8301.
- [10] Y. Hattori, M. Nishikawa, T. Kusamoto, S. Kume, H. Nishihara, *Inorg. Chem.* 2014, 53, 2831–2840.
- [11] D. A. Safin, M. P. Mitoraj, K. Robeyns, Y. Filinchuka, C. M. L. V. Velde, *Dalton Trans.* 2015, 44, 16824–16832.
- [12] J. L. Chen, X. F. Cao, W. Gu, H. R. Wen, L. X. Shi, G. Rong, P. Luo, *Inorg. Chem. Commun.* 2011, 14, 1894–1897.
- [13] N. M. Khatri, M. H. P. Lansigan, W. L. Boncher, J. E. Mertzman, A. C. Labatete, L. M. Grande, D. Wunder, M. J. Prushan, W. G. Zhang, P. S. Halasyamani, J. H. S. K. Monteiro, A. de Bettencourt-Dias, S. L. Stoll, *Inorg. Chem.* 2016, 55, 11408–11417.
- [14] T. Gunaratne, M. A. J. Rodgers, D. Felder, J. F. Nierengarten, G. Accorsic, N. Armaroli, *Chem. Commun.* 2003, 3010–3011.
- [15] M. T. Miller, P. K. Gantzel, T. B. Karpishin, *J. Am. Chem. Soc.* 1999, 121, 4292–4293.
- [16] N. Armaroli, *Chem. Soc. Rev.* 2001, 30, 113.
- [17] C. Bizzarri, C. Strabler, J. Prock, B. Trettenbrein, M. Ruggenthaler, C. H. Yang, F. Polo, A. Iordache, P. Brüggegger, L. D. Cola, *Inorg. Chem.* 2014, 53, 10944–10951.
- [18] J. Föllner, M. Kleinschmidt, C. M. Marian, *Inorg. Chem.* 2016, 55, 7508–7516.
- [19] C. E. McCusker, F. N. Castellano, *Inorg. Chem.* 2013, 52, 8114–8120.
- [20] M. J. Leitzl, V. A. Krylova, P. I. Djurovich, M. E. Thompson, H. Yersin, *J. Am. Chem. Soc.* 2014, 136, 16032–16038.
- [21] S. W. Sun, X. Zhang, G. F. Wang, J. F. Qin, *Russ. J. Coord. Chem.* 2017, 43, 127–132.
- [22] A. Tsuboyama, K. Kuge, M. Furugori, S. Okada, M. Hoshino, K. Ueno, *Inorg. Chem.* 2007, 46, 1992–2001.
- [23] Q. S. Zhang, T. Komino, S. P. Huang, S. Matsunami, K. Goushi, C. Adachi, *Adv. Funct. Mater.* 2012, 22, 2327–2336.
- [24] K. Shimada, A. Kobayashi, Y. Ono, H. Ohara, T. Hasegawa, T. Taketsugu, E. Sakuda, S. Akagi, N. Kitamura, M. Kato, *J. Phys. Chem. C* 2016, 120, 16002–16011.
- [25] S. L. James, C. J. Adams, C. Bolm, D. Braga, P. Collier, T. Friscic, F. Grepioni, K. D. M. Harris, G. Hyett, W. Jones, A. Krebs, J. Mack, L. Maini, A. G. Orpen, I. P. Parkin, W. C. Shearouse, J. W.

- Steedk, D. C. Waddell, *Chem. Soc. Rev.* 2012, 41, 413–447.
- [26] L. Maini, P. P. Mazzeo, F. Farinella, V. Fattorib, D. Bragaa, *Faraday Discuss.* 2014, 170, 93.
- [27] T. Friscic, S. L. James, E. V. Boldyreva, C. Bolm, W. Jones, J. Mack, J. W. Steed, K. S. Suslick, *Chem. Commun.* 2015, 51, 6248–6256.
- [28] C. H. Huang, M. Wen, C. Y. Wang, Y. F. Lu, X. H. Huang, H. H. Li, S. T. Wu, N. F. Zhuang, X. L. Hu, *Dalton Trans.* 2017, 46, 1413–1419.
- [29] M. Vitale, P. C. Ford, *Coord. Chem. Rev.* 2001, 219–221, 3–16.
- [30] D. Braga, F. Grepioni, L. Maini, P. P. Mazzeoa, B. Ventura, *New J. Chem.* 2011, 35, 339–344.
- [31] F. Grifasi, M. R. Chierotti, C. Garino, R. Gobetto, E. Priola, E. Diana, F. Turci, *Cryst. Growth Des.* 2015, 15, 2929–2939.
- [32] H. Ohara, A. Kobayashi, M. Kato, *Chem. Lett.* 2014, 43, 1324–1326.
- [33] H. Ohara, A. Kobayashi, M. Kato, *Dalton Trans.* 2014, 43, 17317–17323.
- [34] A. Kobayashi, T. Hasegawa, M. Yoshida, M. Kato, *Inorg. Chem.* 2016, 55, 1978–1985.
- [35] H. Ohara, A. Kobayashi, M. Kato, *C. R. Chim.* 2015, 18, 766–775.
- [36] J. R. Lakowicz, *Principles of Fluorescence Spectroscopy*, 3rd ed., Springer, New York, 2006, pp. 141–143.
- [37] CrystalClear, Data Collection and Processing Software, Rigaku Corporation (1998–2014), Tokyo 196–8666, Japan.
- [38] M. C. Burla, R. Caliendo, M. Camalli, B. Carrozzini, G. L. Cascarano, C. Giacovazzo, M. Mallamo, A. Mazzone, G. Polidori, R. Spagna, *J. Appl. Crystallogr.* 2012, 45, 357–361.
- [39] G. M. Sheldrick, *Acta Crystallogr., Sect. A: Found. Crystallogr.* 2008, 64, 112–122.
- [40] CrystalStructure 4.1, Crystal Structure Analysis Package, Rigaku Corporation: Tokyo, Japan, 2000–2014.
- [41] A. D. Becke, *J. Chem. Phys.* 1993, 98, 5648–5652.
- [42] C. Lee, W. Yang, R. G. Parr, *Phys. Rev. B: Condens. Matter Mater. Phys.* 1988, 37, 785–789.
- [43] W. J. Hehre, R. Ditchfield, J. A. Pople, *J. Chem. Phys.* 1972, 56, 2257–2261.
- [44] M. M. Francl, W. J. Pietro, W. J. Hehre, J. S. Binkley, M. S. Gordon, D. J. Defrees, J. A. Pople, *J. Chem. Phys.* 1982, 77, 3654–3665.
- [45] D. Andrae, U. Haussermann, M. Dolg, H. Stoll, H. Preuss, *Theor. Chem. Acc.* 1990, 77, 123–141.
- [46] W. Küchle, M. Dolg, H. Stoll, H. Preuss, *J. Chem. Phys.* 1994, 100, 7535–7542.
- [47] M. J. Frisch, G. W. Trucks, H. B. Schlegel, G. E. Scuseria, M. A. Robb, J. R. Cheeseman, G. Scalmani, V. Barone, B. Mennucci, G. A. Petersson, H. Nakatsuji, M. Caricato, X. Li, H. P. Hratchian, A. F. Izmaylov, J. Bloino, G. Zheng, J. L. Sonnenberg, M. Hada, M. Ehara, K. Toyota, R. Fukuda, J. Hasegawa, M. Ishida, T. Nakajima, Y. Honda, O. Kitao, H. Nakai, T. Vreven, J. A. Montgomery Jr., J. E. Peralta, F. Ogliaro, M. Bearpark, J. J. Heyd, E. Brothers, K. N. Kudin, V. N. Staroverov, R. Kobayashi, J. Normand, K. Raghavachari, A. Rendell, J. C. Burant, S. S. Iyengar, J. Tomasi, M. Cossi, N. Rega, J. M. Millam, M. Klene, J. E. Knox, J. B. Cross, V. Bakken, C. Adamo, J. Jaramillo, R. Gomperts, R. E. Stratmann, O. Yazyev, A. J. Austin, R. Cammi, C. Pomelli, J. W. Ochterski, R. L. Martin, K. Morokuma, V. G. Zakrzewski, G. A. Voth, P. Salvador, J. J. Dannenberg, S. Dapprich, A. D. Daniels, Ö. Farkas, J. B. Foresman, J. V. Ortiz, J. Cioslowski, D. J. Fox, *Gaussian 09*, Revision E.01, Gaussian, Inc., Wallingford CT, 2009.

[48] R. Dennington, T. Keith, J. Millam, GaussView 5.0, Semichem Inc., Shawnee Mission, KS, 2009.

Chapter 3

Solvent-free Thermal Synthesis of Luminescent Dinuclear Cu(I) Complexes with Triarylphosphines

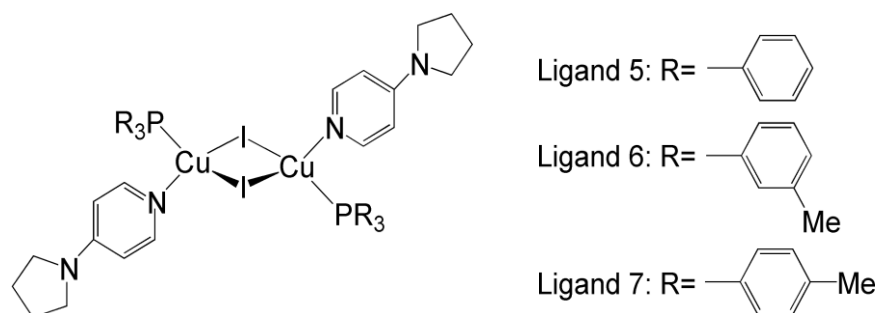
3-1. Introduction

Luminescent Cu(I) complexes have attracted considerable attention over the past few decades because of their interesting luminescence properties and promise as alternative materials to luminescent noble-metal complexes, such as those containing Ru(II), Ir(III), and Pt(II).¹⁻⁶ Although the coordination structures of such noble-metal ions are largely unaffected by the ligands, the coordination structures of Cu(I) ions can be controlled, from two-coordinated linear to four-coordinated tetrahedral, by altering their ligands.⁷⁻¹⁰ Therefore, luminescent Cu(I) coordination compounds exhibit a wide variety of colors and emission origins. For example, the metal-to-ligand charge-transfer (MLCT) excited state is well known to be the emissive state for Cu(I) complexes bearing organic ligands that possess stable π^* orbitals. A wide range of luminescence colors, from blue to red, can be achieved by taking advantage of the fine tunabilities of the π^* orbitals of organic ligands.¹¹⁻¹⁶ Other typical examples are the cubane-type tetranuclear cluster complexes bridged by halide anions that exhibit phosphorescence from their cluster-centered (CC) excited states. In this CC state, metallophilic interactions between the Cu(I) ions in the cluster core are among the most important factors that determine the photophysical properties of the complex. Consequently, the structural flexibility of/around the cluster core can be usefully modified by functionalizing its coordinating ligands.

From the perspective of controllability during synthesis, solution reactions have been widely and traditionally used to prepare numerous luminescent Cu(I) complexes.¹ This strategy is reasonable since the Cu(I) ion is well known to be labile in the solution state; consequently thermodynamically stable complexes are easier to isolate. However, these solution reactions usually require large amounts of solvent and long reaction times to produce the target complex in high purity and yield.¹⁷⁻²⁶ Thermal solid-state reactions can be used to overcome the disadvantages of solution reactions; these methods are attracting increasing attention since they eliminate solvent and minimize reaction times, a result of the extremely high concentration conditions employed. For example, Maini et al. reported the rapid mechanochemical synthesis of luminescent $[\text{Cu}_2\text{I}_2(\text{DABCO})_2]_n$ (DABCO = 1,4-diazabicyclo[2,2,2]octane) Cu(I) coordination polymers that involved only a small amount (~2 drops) of the appropriate solvent.²⁷ Ohara et. al and we recently reported the solvent-free thermal syntheses of luminescent $[\text{CuI}(\text{PPh}_3)_2(\text{L})]$ mononuclear Cu(I) complexes bearing two triphenylphosphine ligands, one *N*-heteroaromatic(L) ligand, and an iodide anion.²⁸⁻²⁹ Although our previous studies suggested that the melting of the phosphine moiety was the key factor that promoted the solvent-free thermal reaction, control of the molecular structure of the luminescent Cu(I) complex using this method remains a challenge. Indeed, the $[\text{CuI}(\text{PPh}_3)_2(\text{iq})]$ mononuclear complex, bearing an isoquinoline (iq) ligand that melts at 24 °C, can be synthesized by a solvent-free mechanochemical method at room temperature. However, the same procedure using liquid pyridine as the *N*-heteroaromatic ligand gives rise to a complex mixture of the $[\text{Cu}_2\text{I}_2(\text{PPh}_3)_2(\text{py})_2]$ and $[\text{CuI}(\text{PPh}_3)_2(\text{py})]$ dinuclear and mononuclear complexes.²⁸ In this work, I aimed to further investigate the role of

coordinating-ligand melting during thermal synthesis. To that end, I chose 4-pyrrolidinopyridine (pyrpy) as the *N*-heteroaromatic ligand, because pyrpy melts at a higher temperature (56–61 °C) than iq or py (24 °C and –42°C, respectively) but lower than amino-functionalized isoquinolines that were used for the thermal synthesis of mononuclear [CuI(PPh₃)₂(L)] (L = amino-functionalized isoquinolines) complexes in our previous study.²⁹ The pyrpy moiety is expected to melt and coordinate to the Cu(I) ion ahead of the triarylphosphines (m.p. = 80, 97–99 and 144–148 °C for triphenylphosphine (PPh₃), tri(*m*-tolyl)phosphine (P(*m*-tol)₃), and tri(*p*-tolyl)phosphine (P(*p*-tol)₃), respectively) during the solid-state thermal reaction, which should lead to formation of the monophosphine-coordinated [Cu₂I₂(PR₃)₂L₂] dinuclear complex rather than the bisphosphine-coordinated [CuI(PR₃)₂L] mononuclear complex. In addition, the melting point of pyrpy, which is only slightly higher than room temperature, facilitates control over the solvent-free thermal synthesis.

Herein, I report the thermal syntheses, X-ray structures, and luminescence properties of the blue-emissive [Cu₂I₂(pyrpy)₂(PR₃)₂] dinuclear Cu(I) complexes (Scheme 3-1). Complexes bearing PPh₃ and P(*p*-tol)₃ ligands were successfully synthesized as crystalline powders by the solvent-free thermal method. A variety of emission experiments reveal that the three complexes exhibit relatively strong emissions that originate from thermally activated delayed fluorescence (TADF) at room temperature and phosphorescence at liquid-N₂ temperature.



Scheme 3-1. Schematic representations of complexes [Cu₂I₂(pyrpy)₂(PR₃)₂] **5–7**.

3-2. Experimental

Caution! *Although I experienced no difficulties, all solvents used in this study are potentially harmful, and should be used in small quantities and handled with care in a fume hood.*

3-2-1. Synthesis

General Procedures: All commercially available starting materials were used as received, and solvents were used without purification. Unless otherwise stated, all manipulations were conducted in air.

Synthesis of $[\text{Cu}_2\text{I}_2(\text{PPh}_3)_2(\text{pyrpy})_2]$ (**5**)

Preparation of 5 as single crystals (S5): CuI (47.6 mg, 0.25 mmol), PPh_3 (131.1 mg, 0.5 mmol), and pyrpy (55.6 mg, 0.375 mmol) were dissolved in CHCl_3 (2 mL). Yellow crystals were obtained by slowly diffusing diethyl ether vapor into the solution at 10 °C over 48 h. The crystals were collected, washed with diethyl ether, and dried under vacuum. Yield: 56.6 mg, 18.8%. Elemental analysis (%) calcd. for $\text{C}_{54}\text{H}_{54}\text{Cu}_2\text{I}_2\text{N}_4\text{P}_2$: C: 53.96, H: 4.53, N: 4.66; found: C: 53.66, H: 4.43, N: 4.50.

Thermal synthesis of 1 (T5): CuI (47.6 mg, 0.25 mmol), PPh_3 (65.6 mg, 0.25 mmol), and pyrpy (88.9 mg, 0.6 mmol) were manually ground using a mortar and pestle for 5 min. The mixture was then heated at 100 ± 5 °C for 20 min. The resulting white powder was collected by suction filtration, washed with diethyl ether, and dried under vacuum. Yield: 104.7 mg, 35.3%. Elemental analysis (%) calcd. for $\text{C}_{54}\text{H}_{54}\text{Cu}_2\text{I}_2\text{N}_4\text{P}_2 \cdot 2\text{H}_2\text{O}$: C: 52.39, H: 4.72, N: 4.53; found: C: 52.49, H: 4.37, N: 4.78.

Synthesis of $[\text{Cu}_2\text{I}_2(\text{P}(m\text{-tol})_3)_2(\text{pyrpy})_2]$ (**6**)

Preparation of 6 as single crystals (S6): CuI (48.5 mg, 0.25 mmol), $\text{P}(m\text{-tol})_3$ (152.9 mg, 0.5 mmol), and pyrpy (74.1 mg, 0.5 mmol) were added to Et_2O (20 mL). The mixture was stirred for 30 min and filtered to remove the unreacted starting materials. White crystals were obtained by slow evaporation of the diethyl ether solvent over 48 h. The crystals were collected by suction filtration, washed with diethyl ether, and dried under vacuum. Yield: 36.4 mg, 11.3%. Elemental analysis (%) calcd. for $\text{C}_{60}\text{H}_{66}\text{Cu}_2\text{I}_2\text{N}_4\text{P}_2$: C: 56.04, H: 5.17, N: 4.36; found: C: 56.10, H: 5.15, N: 4.28.

Synthesis of $[\text{Cu}_2\text{I}_2(\text{P}(p\text{-tol})_3)_2(\text{pyrpy})_2]$ (**7**)

Preparation of 7 as single crystals (S7): CuI (47.6 mg, 0.25 mmol), $\text{P}(p\text{-tol})_3$ (152.2 mg, 0.5 mmol), and pyrpy (92.6 mg, 0.625 mmol) were dissolved in CHCl_3 (6 mL). White crystals were obtained by slowly diffusing diethyl ether vapor into the solution over 48 h. The crystals were collected by filtration, washed with diethyl ether, and dried under vacuum. Yield: 23.9 mg, 32%. Elemental analysis (%) calcd. for $\text{C}_{60}\text{H}_{66}\text{Cu}_2\text{I}_2\text{N}_4\text{P}_2$: C: 56.04, H: 5.17, N: 4.36; found: C: 55.81, H: 5.12, N: 4.30.

Thermal synthesis of 3 (T7): CuI (47.6 mg, 0.25 mmol), $\text{P}(p\text{-tol})_3$ (152.2 mg, 0.5 mmol), and pyrpy (111.2 mg, 0.75 mmol) were added to a mortar and manually ground using a pestle for 5 min. The mixture was then heated at 100 ± 5 °C for 20 min. After cooling to room temperature, the resulting white powder was collected by filtration, washed with diethyl ether, and dried under vacuum. Yield: 141.4 mg, 87.4%. Elemental analysis (%) calcd. for $\text{C}_{60}\text{H}_{66}\text{Cu}_2\text{I}_2\text{N}_4\text{P}_2$: C: 56.04, H: 5.17, N: 4.36; found: C: 56.25,

H: 5.14 N: 4.45.

3-2-2. Physical measurements

Elemental analyses were performed using a MICRO CORDER JM 10 analyzer at the Analysis Center, Hokkaido University. ¹H NMR spectra were acquired on a JEOL EX-270 NMR spectrometer at room temperature; chemical shifts were internally referenced to tetramethylsilane. Thermogravimetry and differential thermal analyses (TG-DTA) were performed using a Rigaku ThermoEvo TG8120 analyzer. Powder X-ray diffraction (PXRD): All PXRD patterns were collected using a Bruker D8 Advance diffractometer equipped with a graphite monochromator using CuK α radiation and a one-dimensional LinxEye detector.

Single-crystal X-ray diffraction (XRD): All single-crystal XRD data were collected using a Rigaku Mercury diffractometer equipped with graphite-monochromated MoK α radiation ($\lambda = 0.71069 \text{ \AA}$) and a rotating anode generator. The single crystal was mounted on a MicroMount using paraffin oil. The crystal was then cooled using a N₂-flow-type temperature controller. The diffraction data were processed using CrystalClear software.³¹ Structures were solved by the direct method using SHELXS-2013 (for **5** and **7**) or SIR2014 (for **6**).^{32,33} Structures were refined by full-matrix least-squares refinement using SHELXL-2014.³³ Nonhydrogen atoms were refined anisotropically, while the hydrogen atoms were refined using the riding model. All calculations were performed using the CrystalStructure crystallographic software package.³⁴ The crystallographic data obtained for each complex are listed in Table 1. Full crystallographic data have been deposited with the Cambridge Crystallographic Data Centre (CCDC 1821141–1821143).

3-2-3. Luminescence measurements

The luminescence spectrum of each crystalline sample was measured using a JASCO FP-6600 spectrofluorometer at room temperature and 77 K. Luminescence quantum yields were determined using a Hamamatsu Photonics C9920-02 absolute photoluminescence quantum yield spectrometer fitted with an integrating sphere and a 150-W CW Xe light source. Emission life times were determined using a Hamamatsu Photonics C4334 system equipped with a streak camera as the photodetector and a nitrogen laser as the excitation light source ($\lambda_{\text{ex}} = 337 \text{ nm}$). The sample temperature was controlled using a liquid-N₂ cryostat (Optistat-DN optical Dewar and ITC-503 temperature controller, Oxford Instruments). Emission decays were analyzed using two exponentials; i.e., $I = A_1 \exp(-t/\tau_1) + A_2 \exp(-t/\tau_2)$, where τ_1 and τ_2 are the lifetimes, and A_1 and A_2 are the pre-exponential factors. The average lifetimes (τ_{av}) were used to determine the radiative and nonradiative rate constants of the two exponential decay components using Eq. 1.³⁰

$$\tau_{\text{av}} = (A_1\tau_1^2 + A_2\tau_2^2) / (A_1\tau_1 + A_2\tau_2) \quad \text{Eq. 3-1}$$

3-2-4. Computational methods

Starting from the X-ray structures, the ground states (S_0) of the Cu dimer complexes **5**–**7** were optimized using density functional theory (DFT) with the PBE1PBE functional³⁵ as implemented in the Gaussian16 program.³⁶ The SDD effective-core-

potential (ECP) basis set³⁷ was used for Cu and I, and the 6-311G(d,p)³⁸ basis sets was used for the remaining atoms. Following optimization of the S₀ structures, the lowest singlet excited state (S₁), and lowest triplet excited state (T₁) structures were optimized using time-dependent density functional theory (TD-DFT). The nature of each optimized structure was confirmed by vibrational frequency calculations (i.e., no imaginary frequencies for minima). Vertical excitations were calculated at The PBE1PBE/BS1 level of theory. The S₁ and T₁ states were optimized using the PBE1PBE functional and the SDD basis set for Cu and I, the Def2-TZV basis set for N and P, and the Def2-SVP basis set for the remaining atoms.³⁹ Computed emission wave length from the S₁ state show better agreement with the experimental data when I used the triple-zeta basis sets. All ground and excited state structure optimizations were full with no restrictions.

Table 3-1. Crystal parameters and refinement data for complexes **5–7**.

	5	6	7
<i>T</i> / K	173(1)	196(1)	196(1)
Formula	C ₅₄ H ₅₄ Cu ₂ I ₂ N ₄ P ₂	C ₆₀ H ₆₆ Cu ₂ I ₂ N ₄ P ₂	C ₆₀ H ₆₆ Cu ₂ I ₂ N ₄ P ₂
Formula weight	1201.90	1286.04	1286.04
Crystal system	<i>Monoclinic</i>	<i>Triclinic</i>	<i>Monoclinic</i>
Space group	<i>P2₁/c</i>	<i>P-1</i>	<i>P2₁/n</i>
<i>a</i> / Å	9.727(2)	15.1674(3)	10.5712(8)
<i>b</i> / Å	19.039(3)	16.5780(3)	20.134(1)
<i>c</i> / Å	13.576(2)	18.5498(4)	14.0267(9)
<i>α</i> / °	90	106.54 (2)	90
<i>β</i> / °	97.849(2)	98.782(2)	110.986(3)
<i>γ</i> / °	90	99.531(2)	90
<i>V</i> / Å ³	2490.7(7)	4309.9 (2)	2787.4(3)
<i>D</i> / g·cm ⁻³	1.602	1.486	1.532
<i>Z</i>	2	3	2
<i>R</i> ₁ (<i>I</i> > 2.00σ(<i>I</i>)) ^a	0.0305	0.0495	0.0376
<i>wR</i> ₂ ^b	0.0803	0.1164	0.0958

$$^a R_1 = \sum ||F_o| - |F_c|| / \sum |F_o|. \quad ^b wR_2 = [(w(F_o^2 - F_c^2)^2) / w(F_o^2)^2]^{1/2}.$$

3-3. Results and discussion

3-3-1. Crystal structures

Single crystals of complexes **5–7** were successfully obtained from traditional solution reactions followed by the widely used vapor-diffusion method. Note that I used CHCl_3 or Et_2O solvents for the solution reactions to synthesize **5–7**, but the reaction in CH_3CN that is a typical good solvent for CuI were failed because of the rapid oxidation of CuI . The molecular structure of each complex was determined by X-ray crystallography and is displayed in Figure 3-1. Each Cu(I) ion in each of the three complexes adopts a tetrahedral coordination geometry that is occupied by two iodide anions, a N atom from the pyrpy, and a P atom from the phosphine; a similar iodide-bridged rhombic dinuclear $\{\text{Cu}_2\text{I}_2\}$ core was found in each of the three complexes. Selected bond distances and angles are listed in Table 3-2. The coordination structures around the Cu(I) ions of the three complexes are similar to those reported to have inversion centers.^{40–42} Half of each dinuclear molecule is crystallographically independent in complexes **5** and **7** because of the inversion center at the midpoint of the dinuclear rhombic $\{\text{Cu}_2\text{I}_2\}$ core. While a similar symmetric molecular dinuclear complex (**6S**) was found in the crystal of **6**, another crystallographically independent dinuclear molecule that does not contain an inversion center (**6A**) was also found in the unit cell. This is ascribed to the orientations of the methyl groups attached to the PR_3 ligand; all six methyl groups in **6S** are located at the outer-edge of the **6S** molecule, whereas only one methyl group (C30A in Figure 1(b)) of **6A** faces toward the inside of the molecule (i.e., near the dinuclear Cu_2I_2 core). The dinuclear rhombic cores of the $\{\text{Cu}_2\text{I}_2\}$ units of the symmetric dinuclear complexes **5**, **6S**, and **7** are planar, while the core in asymmetric **6A** is slightly distorted. The Cu-P bond lengths increase in the order: **5** < **6** < **7**, which is probably due to enhanced σ -donation from the PR_3 ligands substituted by methyl groups at the *meta*- or *para*-positions of their benzene rings.

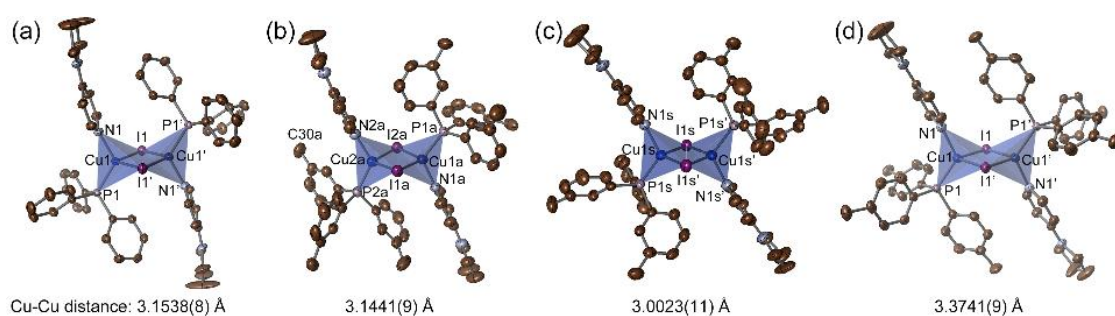


Figure 3-1. Molecular structures of (a) **5**, (b) **6A**, (c) **6S**, and (d) **7**. Cu(I) coordination spheres are depicted as blue tetrahedrons. Brown, light blue, pale purple, and dark purple ellipsoids represent C, N, P, and I atoms, respectively. H atoms are omitted for clarity. Displacement parameters are drawn at the 50% probability level.

Table 3-2. Selected bond lengths (Å), and bond and torsion angles (°) of **5**–**7**.

	5	6A	6S	7
Cu-I	2.6855(4)	2.7344(7), 2.6954(8)	2.6678(6)	2.7450(6)
Cu-I'	2.7017(5)	2.6741(8), 2.7104(7)	2.6922(5)	2.7002(6)
Cu-P	2.2198(6)	2.236(2), 2.229(2)	2.234(1)	2.2335(8)
Cu-N	2.044(2)	2.043(5), 2.047(5)	2.047(4)	2.053(3)
Cu...Cu'	3.1538(8)	3.1441(9)	3.002(1)	3.3741(9)
I-Cu-I'	108.44(2)	108.59(3), 108.68(3)	111.89(2)	103.42(2)
I-Cu-P	111.39(2)	108.36(4), 107.32(4)	107.13(4)	111.06(3)
I'-Cu-P'	108.68(2)	109.18(4), 108.91(4)	110.47(3)	109.79(3)
I-Cu-N	104.72(6)	103.1(1), 103.8 (1)	104.85(9)	102.71(8)
I'-Cu-N'	102.21(5)	107.7(1), 102.6(1)	104.16(9)	106.67(7)
Cu-I...I'-Cu'	180	170.88(4)	180	180

3-3-2. Thermal syntheses

Figure 3-2 displays the powder X-ray diffraction (PXRD) patterns of ground samples of CuI, pyrpy, and the phosphines. The ground mixtures of the starting materials (**G5** and **G6**; brown traces in Figure 3-2) exhibit strong diffraction peaks that correspond to the starting materials themselves (e.g., 25.4° for CuI), confirming that no reaction had occurred prior to heating. This is expected since all ligands used in these reactions have melting points that are higher than room temperature (m.p. = 54–58, 80, 97–99, and 144–148 °C for pyrpy, PPh₃, P(*m*-tol)₃, and P(*p*-tol)₃, respectively); hence no solvent that could actually promote any reaction was present. Notably, the observed PXRD patterns of the thermally synthesized samples (**T5** and **T7**; red traces in Figure 3-2) were almost identical to those of the complexes prepared by the traditional solution method (**S5** and **S7**; blue traces in Figure 3-2).

In addition, the simulated patterns, calculated from the X-ray structures, indicate that the [Cu₂I₂(PR₃)₂(pyrpy)₂] dinuclear Cu(I) complexes had been successfully synthesized by the solvent-free thermal method as well as through the traditional solution reaction. The purities of the solvent-free-prepared samples were confirmed by elemental analyses (see Experimental Section), and their ¹H NMR spectra (Figure 3-3) were identical to those of the complexes obtained by the traditional solution method. Although I also attempted to thermally prepare complex **6**, bearing the P(*m*-tol)₃ ligand, only an amorphous solid was formed (see Figure 3-4 in the Supporting Information). Although the reason for this observation remains unclear, it might be related to the following two factors. Firstly, two different dinuclear molecules **6A** and **6S** coexist in the crystal of the P(*m*-tol)₃-containing complex **6**, which engenders lower symmetry resulting in a synthesized product of poor crystallinity. Secondly, complex **6** exhibits different solubilities to **5** and **7**; that is, **6** dissolves well in Et₂O, but Et₂O is a poor solvent for the other complexes, as mentioned in the Experimental Section.

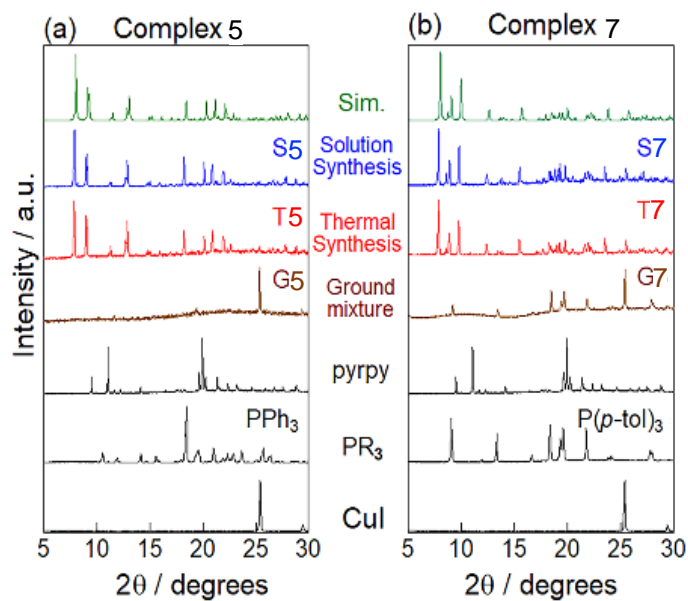


Figure 3-2. PXRD patterns of complexes **1** and **3** synthesized in the solution state (**S**) and by the thermal method (**T**); the ground mixture (**G**) is shown for comparison. The molar ratios of the starting materials used in these experiments are as described in the Experimental Section. The top pattern in each panel is that simulated on the basis of the X-ray structure.

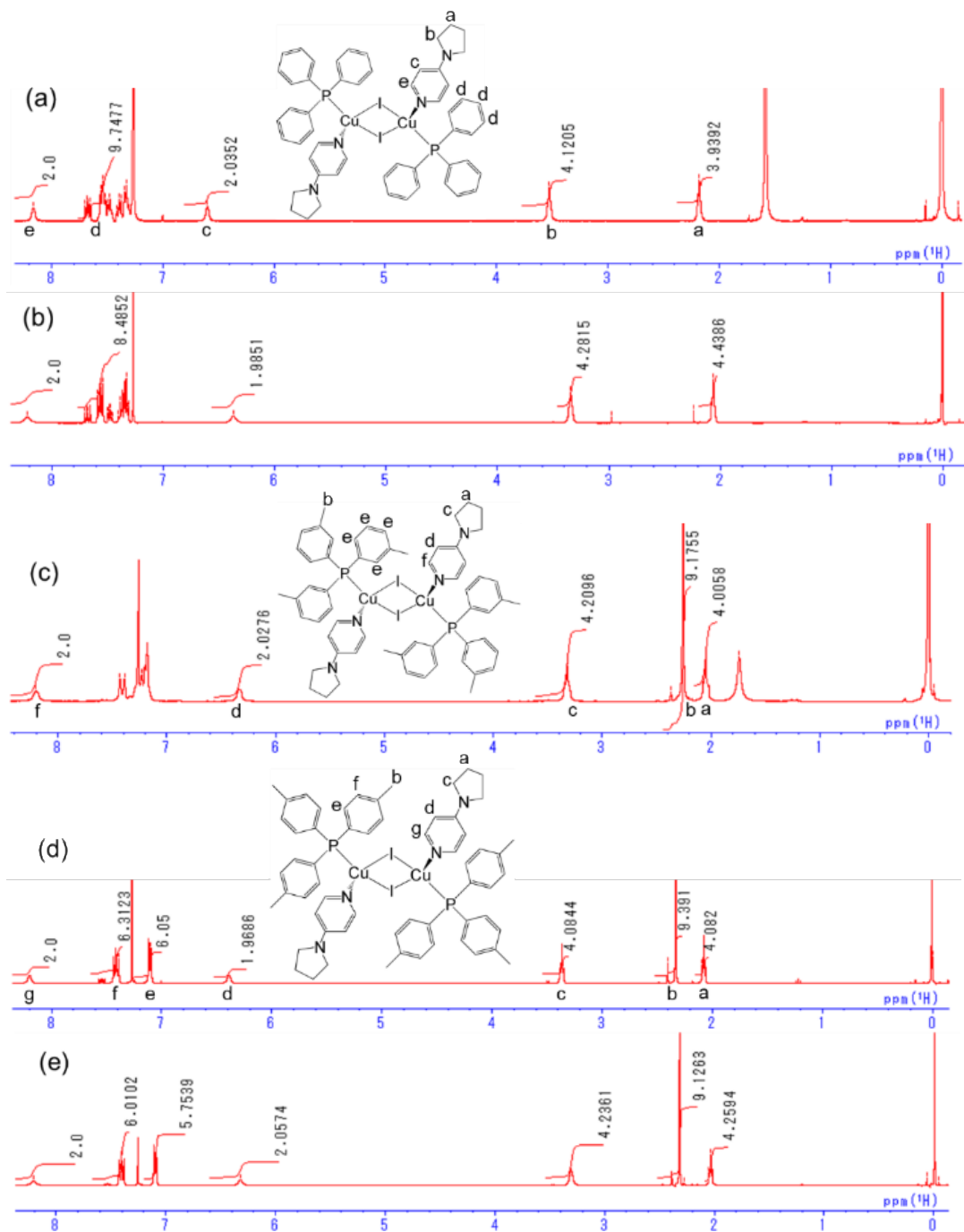


Figure 3-3. ^1H NMR spectra of **S5** (a) (CDCl_3), **T5** (b) (CDCl_3), **S6** (c) (CDCl_3), **S7** (d) (CDCl_3) and **T7** (e) (CDCl_3).

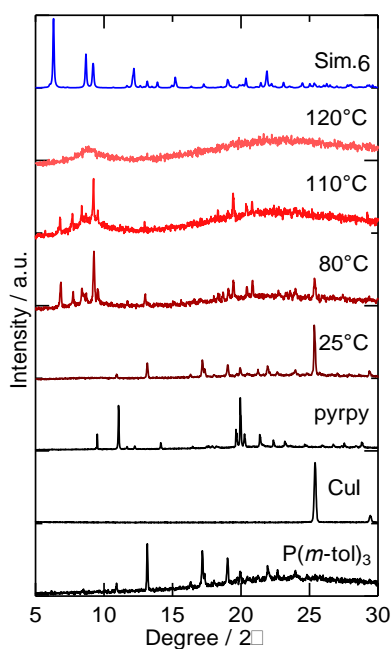


Figure 3-4. Temperature dependences of PXRD patterns of the ground mixtures of 1 eq. CuI, 1 eq. pyrpy, and 2 eq. P(*m*-tol)₃ to thermally synthesize complex **6**. The top blue line shows the simulation pattern calculated from the X-ray structure of **2**.

To investigate the thermal syntheses of **5** and **7** in more detail, I investigated the temperature dependences of the PXRD patterns of samples containing CuI, pyrpy, and the phosphines. As mentioned in the Introduction, I previously reported the thermal syntheses of the luminescent mononuclear Cu(I) complexes [CuI(PPh₃)₂L] (L = 4-aminoisoquinoline, 5-aminoisoquinoline) and found that the melting of the phosphine moiety was the key to a successful thermal synthesis.²⁹ Since pyrpy exhibits a lower melting point than the PR₃ moieties, I expected that the thermal synthesis might be achievable at lower temperature. Although a strong diffraction peak at 25.4° derived from unreacted solid CuI was observed for each sample at 25 °C, as shown in Figure 3-5, the peak was completely absent above 50 °C and dramatic changes were observed for both samples. The patterns observed for the PPh₃-containing sample above 60 °C were in qualitative agreement with the simulated pattern calculated from the X-ray structure of **1**. Hence, I conclude that the dinuclear complex **1** was successfully obtained by the simple heating of the ground mixture. On the other hand, the PXRD patterns of the mixture containing P(*p*-tol)₃ in the 50–110 °C temperature range were different from that simulated for complex **3**; however, at 150 °C it transformed into one that corresponded well with that simulated for **3**. This two-step change suggests that the thermal synthesis of **3** occurs via an intermediate phase, whereas complex **1** appears to be synthesized thermally in one step. These contrasting results clearly indicate that the temperature required to form the [Cu₂L₂(pyrpy)₂L₂] dinuclear Cu(I) complexes strongly depends on the melting point of the phosphine (L).

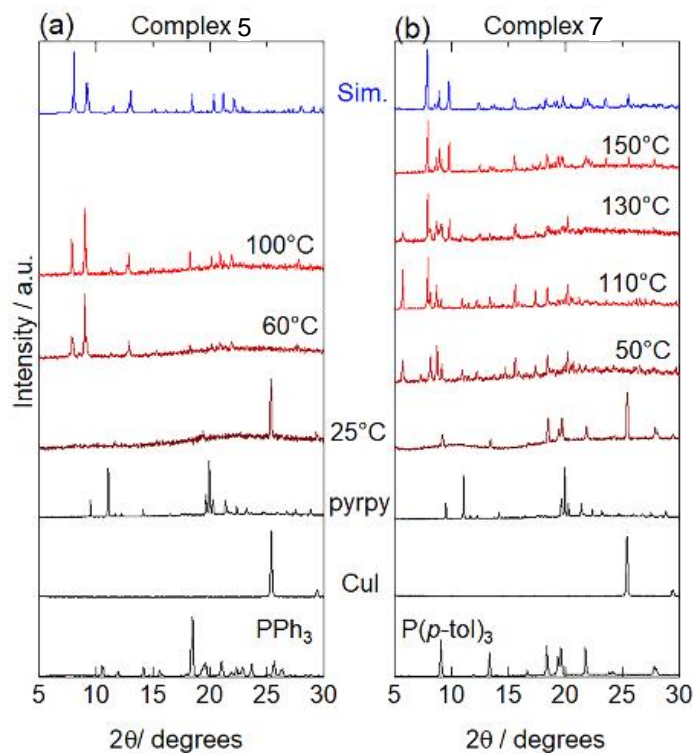


Figure 3-5. PXRD patterns of the ground mixtures of CuI, pyrpy, and (a) PPh₃ or (b) P(*p*-tol)₃ as functions of temperature. The molar ratios of the starting materials used in these experiments are as described in the Experimental Section. The top pattern in each panel is that simulated on the basis of the X-ray structure.

In order to obtain further insight into the thermal-syntheses of complexes **5** and **7**, ground mixtures of CuI, pyrpy, and the PR₃ ligands were also analyzed by TG–DTA. Figure 3-6 reveals that both mixtures underwent negligible weight changes (< 1%) at temperatures below 100 °C. The mixture containing PPh₃ underwent a weight decrease of about 10 wt% in the 100–150 °C temperature range (Figure 3-6a), which is probably ascribable to the evaporation of pyrpy and/or the PPh₃ ligands. The weight loss in this temperature range was suppressed for the P(*p*-tol)₃-containing mixture since P(*p*-tol)₃ melts at 144–148 °C. Hence, most of the reagents used in these thermal syntheses remained in the mixtures until complexes **5** and **7** had been synthesized by heating (below 100 and 150 °C for **5** and **7**, respectively). It should be noted that complexes obtained by the traditional solution method (**5S** and **7S**) did not exhibit any phase transition or decomposition in this temperature range (Figure 3-7). Several interesting features are evident in the DTA traces. For example, small endothermic peaks assignable to the melting of pyrpy were observed at around 30 °C for both mixtures. The discrepancy between the temperatures of these peaks and the melting point of the pure pyrpy ligand (54–58 °C) is ascribable to melting-point depression through the mixing of CuI and PPh₃. In fact, endothermic peaks that correspond to the melting of pyrpy were observed at 37 and 48 °C for the mixtures containing PPh₃ and P(*p*-tol)₃,

respectively (Figures 3-8 and 3-9). It should be noted that two remarkable exothermic peaks were observed at 42 and 76 °C for the PPh₃-containing mixture.

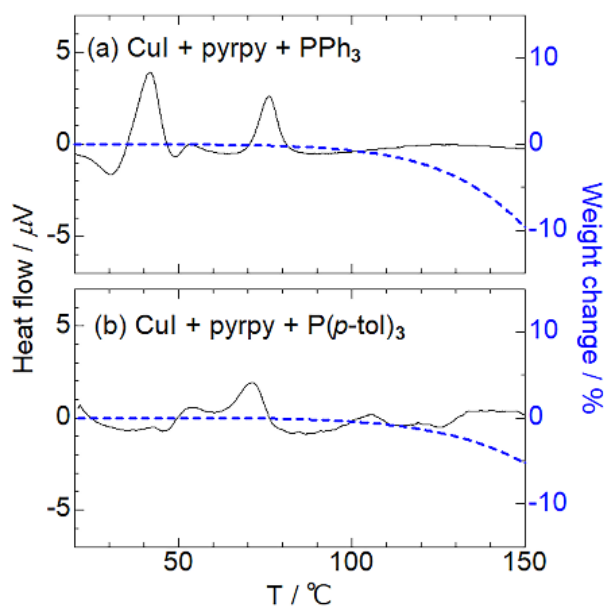


Figure 3-6. TG (dotted blue lines) and DTA (solid black lines) traces of ground mixtures of CuI, pyrpy, and (a) PPh₃ or (b) P(*p*-tol)₃ under a flow of Ar (flow rate: 250 mL/min). The molar ratios of the mixture are the same as those used in the thermal syntheses.

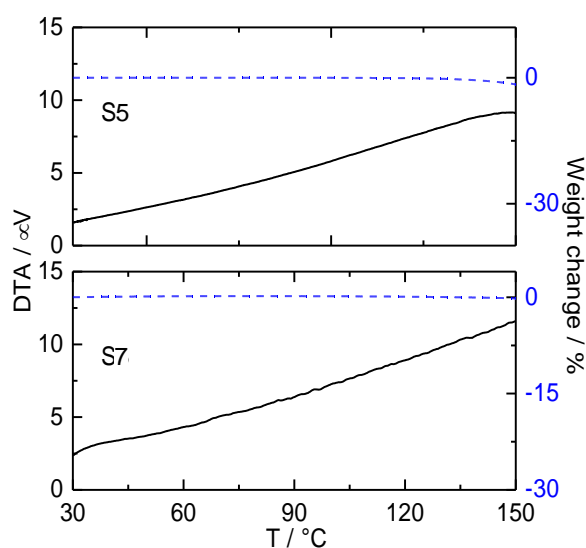


Figure 3-7. TG (dotted lines) and DTA (solid lines) curves of the solution synthesized complexes **S5** and **S7**, under Ar flow (flow rate: 250 mL/min).

Considering that complex **5** had already formed at 60 °C, as suggested by PXRD (Figure 3-5a), the exothermic peak at the lower temperature of 42 °C is ascribable to the heat associated with the formation of complex **5** in the molten pyrpy. On the other

hand, an almost identical PXRD pattern to that of **5** was also observed at 100 °C; the second exothermic peak at 76 °C is also assignable to the heat associated with the formation of complex **5** in the molten mixture of PPh₃ and pyrpy, since PPh₃ melts at a temperature close to this value. The DTA trace of the mixture used for the thermal synthesis of complex **7** is more complicated, but noticeable features are present. Exothermic peaks were observed at 54 and 71 °C, and broad endothermic peaks were observed at higher temperatures. An intermediate phase was observed at 50 °C in the PXRD pattern, as shown in Figure 3-5b, suggesting that the exothermic peaks can be assigned to the heat associated with the formation of the intermediate phase. Although I have not identified this intermediate, the dinuclear complex bearing four pyrpy ligands, [Cu₂I₂(pyrpy)₄], is one plausible species. The broad endothermic peak in the higher temperature region is due to the melting of the P(*p*-tol)₃ in the mixture, which might promote the ligand-exchange reaction from an already coordinated pyrpy in the above-mentioned intermediate to form complex **7** bearing two pyrpy and two P(*p*-tol)₃ ligands.

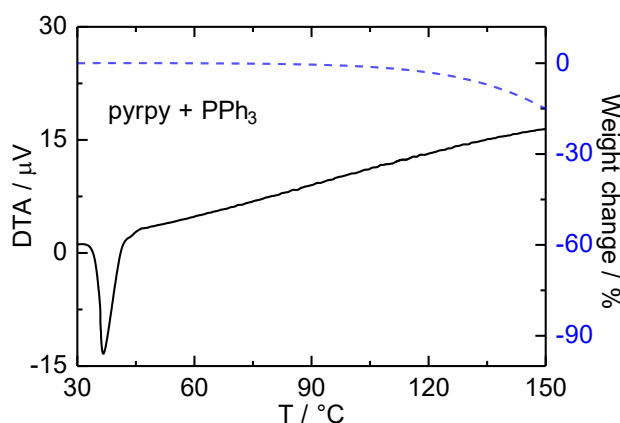


Figure 3-8. TG (blue dotted lines) and DTA (black solid lines) curves of the mixture of pyrpy and PPh₃ under Ar flow (flow rate: 250 mL/min).

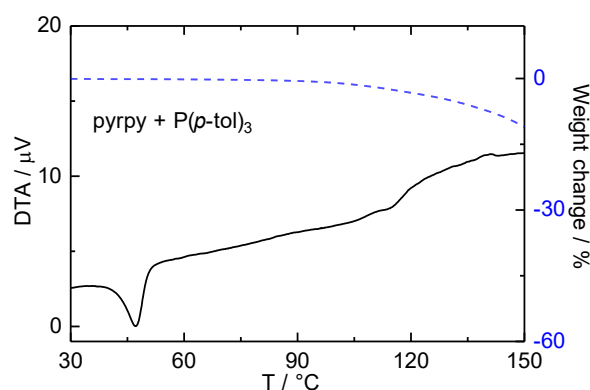


Figure 3-9. TG (dotted lines) and DTA (solid lines) curves of the mixture of pyrpy and P(*p*-tol)₃ under Ar flow (flow rate: 250 mL/min).

3-3-3. Photophysical properties

As discussed in the Introduction, halide-bridged dinuclear Cu(I) complexes are known to be luminescent materials and their emission colors can be modified by the *N*-heteroaromatic ligand. To evaluate the effect of the methyl groups on the aryl rings of the phosphine ligand, the photophysical properties of complexes **5–7** were investigated in detail, the results of which are summarized in Table 3-3. As shown in Figure 3-10, the three complexes (**S5–S7**) prepared through traditional solution reactions exhibit very similar blue emissions when irradiated by UV light. The emission spectra of **S5–S7** at 298 and 77 K are displayed in Figure 3-11. Almost identical emission spectra were observed for the thermally synthesized samples **T5** and **T7** (Figure 3-12), indicating that these complexes were successfully obtained through thermal synthesis. In order to evaluate the photophysical properties of these complexes, I used the solution-prepared crystalline samples of complexes **5–7** for all photophysical experiments. Broad bands devoid of vibrational progressions and centered at around 440 nm were commonly observed for the three complexes at 298 K.

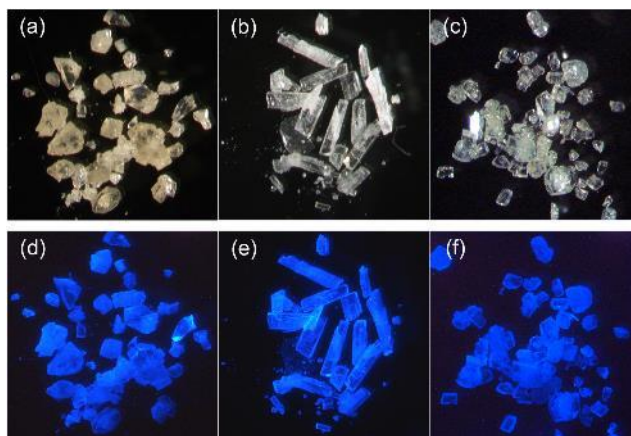


Figure 3-10. Photographic images of (a, d) **S5**, (b, e) **S6**, and (c, f) **S7** acquired under bright-field (upper) and UV-irradiation (lower) conditions.

A broad blue emission was also reported for $[\text{Cu}_2\text{Br}_2(\text{dmap})_2(\text{PPh}_3)_2]$, a similar dinuclear Cu(I) complex bearing an *N,N*-dimethylaminopyridine (dmap) ligand ($\lambda_{\text{max}} = 450$ nm at RT).^{43,44} These broad emission spectra suggest the contributions from charge-transfer transitions to emissive states. Emission bands from **6** and **7** were observed at slightly longer wavelengths than that of **5**, specifically by 17 and 14 nm, respectively, which is probably due to the enhanced σ -donating ability of the $\text{P}(p\text{-tol})_3$ ligand compared to PPh_3 , a consequence of the electron-donating methyl groups (see below). Narrower emission bands at slightly longer wavelengths were observed at 77 K for **5** and **7**, but at almost the same position for **7**. Interestingly, while the emission quantum yield (Φ) increased in the order: **5** < **6** < **7** at 298 K, the quantum yield of **5** was remarkably higher at 77 K, and higher than those of both **6** and **7** (Table 3-3). The higher emission quantum yield of **7** compared to **6** at both temperatures is ascribable to **7** having a more tightly packed crystal structure than **6**, consistent with its slightly

higher density (Table 3-1), which suppresses vibrational deactivation from the emissive state. The emission lifetimes of the three complexes at 298 K are of the order of a few μs , whereas they are remarkably longer at 77 K ($\sim 100 \mu\text{s}$) (see Table 3-3 and Figure 3-13). The estimated radiative decay constants (k_r) of the three complexes, based on their average emission lifetimes and quantum yields, are comparable to each other at each temperature. The significant decrease in the k_r values (by about two orders of the magnitude) observed by lowering the temperature to 77 K is suggestive of contributions from thermally activated delayed fluorescence (TADF) at 298 K.

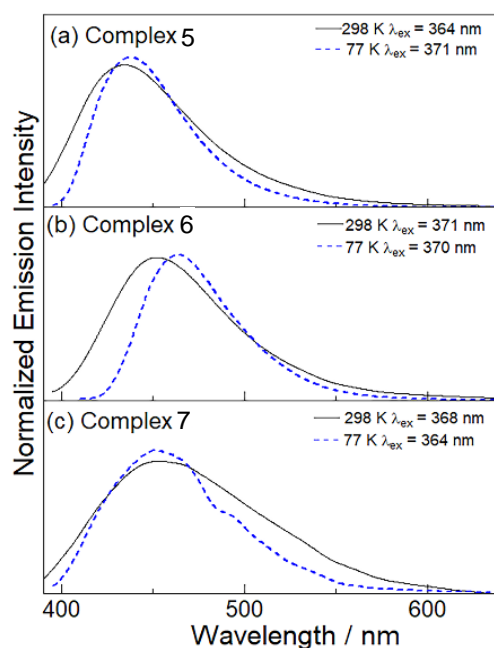


Figure 3-11. Solid-state emission spectra of (a) **S5**, (b) **S6**, and (c) **S7** at 77 K (blue dotted lines) and 298 K (black solid lines).

Table 3-3. Photophysical properties of complexes 5–7 in the solid state.

Complex	5		6		7	
T / K	298	77	298	77	298	77
$\lambda_{\text{max}} / \text{nm}$	435	438	452	463	449	432
$\tau_1 / \mu\text{s}$	0.777	50	1.609	83	2.299	24.431
$(A_1)^a$	(0.704)	(0.504)	(1.052)	(1.08)	(1.182)	(0.648)
$\tau_2 / \mu\text{s}$	3.325	120	6.042	305	8.076	101.532
$(A_2)^a$	(0.228)	(0.576)	(0.076)	(0.024)	(0.173)	(0.42)
$\tau_{\text{av}}^b / \mu\text{s}$	2.25	101.29	2.55	99.76	4.26	80.66
Φ	0.24	0.93	0.31	0.60	0.51	0.73

k_r^c / s^{-1}	106×10^3	9.2×10^3	122×10^3	6.0×10^3	120×10^3	9.0×10^3
k_{nr}^d / s^{-1}	337×10^3	0.7×10^3	269×10^3	4.1×10^3	115×10^3	3.4×10^3

^aEmission lifetime. Emission decays were analyzed with two components: $I = A_1 \exp(-t/\tau_1) + A_2 \exp(-t/\tau_2)$. ^bAverage emission lifetimes determined from Eq. (1). ^cRadiative rate constants $k_r = \Phi/\tau_{av}$. ^dNonradiative rate constants $k_{nr} = k_r(1 - \Phi) / \Phi$.

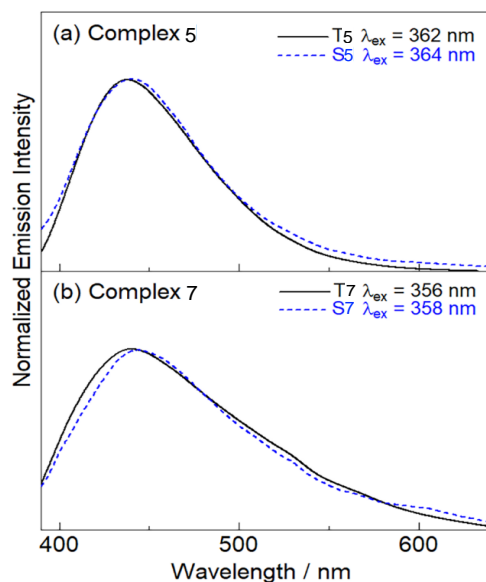


Figure 3-12. Emission spectra of complexes (a) S5 and T5, (b) S7 and T7 in the solid state at 298 K.

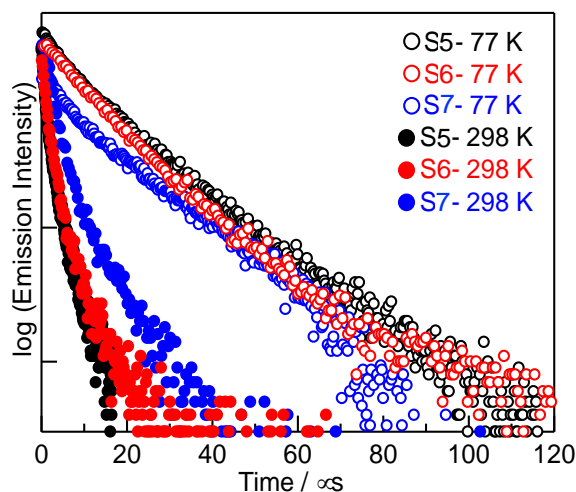


Figure 3-13. Emission decay curve of complexes S5, S6 and S7 in the solid state at 77 K and 298 K.

I investigated the origins of the emissions from the three complexes using density functional theory (DFT) and time-dependent density functional theory (TD-DFT). The

key structural parameters of the optimized S_0 , S_1 , and T_1 structures are summarized in Tables 3-4 to 3-6. Calculated ground state (S_0) structures [**5**: $r(\text{Cu-I}) = 2.73, 2.74, 2.74, 2.73 \text{ \AA}$; **7**: $r(\text{Cu-I}) = 2.73, 2.73, 2.74, 2.73 \text{ \AA}$, see Tables 3-4 to 3-6 for more information] are in good agreement with the X-ray structures and hold symmetric $\{\text{Cu}_2\text{I}_2\}$ units [**5**: $r(\text{Cu-I}) = 2.69, 2.70 \text{ \AA}$; **3**: $r(\text{Cu-I}) = 2.75, 2.70 \text{ \AA}$]. On the other hand, the X-ray structure of complex **6** displays both symmetric [$r(\text{Cu-I}) = 2.67, 2.69 \text{ \AA}$] and asymmetric $\{\text{Cu}_2\text{I}_2\}$ units [$r(\text{Cu-I}) = 2.73, 2.70, 2.67, 2.71 \text{ \AA}$]. However, both the symmetric and asymmetric structures of complex **6** converged to the same minimum during DFT optimizations; this structure exhibited a symmetric $\{\text{Cu}_2\text{I}_2\}$ unit [$r(\text{Cu-I}) = 2.74, 2.74, 2.74, 2.74 \text{ \AA}$]. The Kohn-Sham orbitals in the frontier region of complex **5** are shown in Figure 3-14 together with their energies. The HOMO of **5** is calculated to be delocalized over both the Cu and I atoms and displays Cu-I anti-bonding character, while the LUMO is delocalized over both phosphine ligands. Similar orbital features are observed for complexes **6** and **7** (Figures 3-15 and 3-16). Three complexes exhibit comparable calculated HOMO-LUMO gaps of 4.26 eV for **5**, 4.27 eV for **6**, and 4.30 eV for **7**, which are consistent with the almost identical excitation spectra of these complexes in the solid state (Figure 3-17).

Table 3-4. Selected bond lengths (\AA) and bond angles ($^\circ$) of **5** in S_0 , S_1 and T_1 states after the optimization.

	X-ray	S₀	S₁	T₁
Cu(1)-Cu(2)/ \AA	3.1538(8)	2.98	2.93	3.12
Cu(1)-I(1)/ \AA	2.6855(4)	2.73	2.70	2.75
Cu(1)-I(2)/ \AA	2.7017(5)	2.74	2.68	2.72
Cu(2)-I(1)/ \AA	2.7017(5)	2.74	2.64	2.65
Cu(2)-I(2)/ \AA	2.6855(4)	2.73	2.64	2.65
Cu(1)-P(1)/ \AA	2.2198(6)	2.27	2.33	2.31
Cu(1)-N(1)/ \AA	2.044(2)	2.09	2.06	2.04
Cu(2)-P(2)/ \AA	2.2198(6)	2.27	2.34	2.34
Cu(2)-N(2)/ \AA	2.044(2)	2.09	2.10	2.06
I(1)-Cu(1)-I(2)/ $^\circ$	108.44(2)	114.8	111.8	106.2
I(1)-Cu(1)-P(1)/ $^\circ$	111.39(2)	108.9	110.0	108.9
I(2)-Cu(1)-P(1)/ $^\circ$	108.68(2)	110.1	110.0	111.5
I(1)-Cu(1)-N(1)/ $^\circ$	104.72(6)	104.5	102.6	103.5
I(2)-Cu(1)-N(1)/ $^\circ$	102.21(5)	102.6	106.5	107.1
I(1)-Cu(2)-I(2)/ $^\circ$	108.44(2)	114.8	114.5	111.4
I(1)-Cu(2)-P(1)/ $^\circ$	108.68(2)	110.1	116.6	119.4
I(2)-Cu(2)-P(2)/ $^\circ$	111.39(2)	108.9	105.9	103.1
I(1)-Cu(2)-N(2)/ $^\circ$	102.21(5)	102.6	106.7	109.4
I(2)-Cu(2)-N(2)/ $^\circ$	104.72(6)	104.5	105.1	112.0

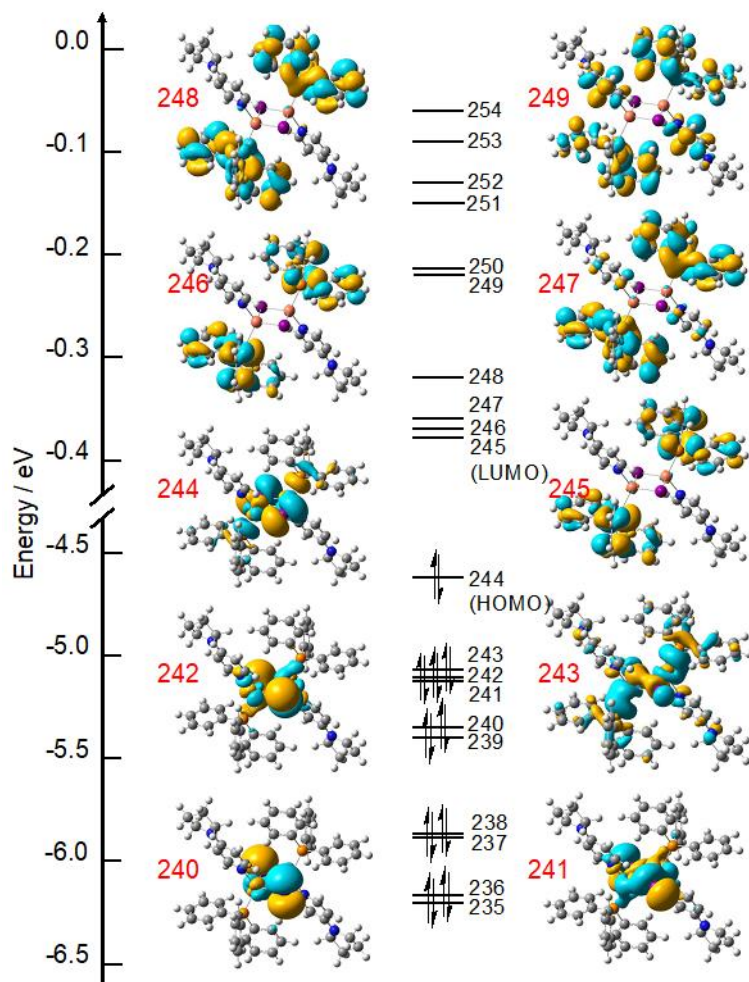


Figure 3-14. Kohn-Sham orbitals and energies in the frontier region of the ground-state-optimized complex **5**.

Table 3-5. Selected bond lengths (Å) and bond angles (°) of **6** in S₀, S₁ and T₁ states after the optimization.

	X-ray	S0	S1	T1
Cu(1)-Cu(2)	3.002(1)	2.94	2.93	3.07
Cu(1)-I(1)/Å	2.6678(6)	2.73	2.70	2.75
Cu(1)-I(2)/Å	2.6922(5)	2.73	2.67	2.71
Cu(2)-I(1)/Å	2.6922(5)	2.74	2.63	2.64
Cu(2)-I(2)/Å	2.6678(6)	2.73	2.64	2.65
Cu(1)-P(1)/Å	2.234(1)	2.27	2.33	2.31
Cu(1)-N(1)/Å	2.047(4)	2.09	2.06	2.04
Cu(2)-P(2)/Å	2.234(1)	2.27	2.33	2.34
Cu(2)-N(2)/Å	2.047(4)	2.09	2.11	2.07
I(1)-Cu(1)-I(2)/°	111.89(2)	114.9	111.4	107.2
I(1)-Cu(1)-P(1)/°	107.13(4)	109.1	110.0	109.1
I(2)-Cu(1)-P(1)/°	110.47(3)	110.4	110.3	110.4
I(1)-Cu(1)-N(1)/°	104.85(9)	104.5	102.6	103.1
I(2)-Cu(1)-N(1)/°	104.16(9)	102.7	106.4	106.9
I(1)-Cu(2)-I(2)/°	111.89(2)	114.7	114.5	112.8
I(1)-Cu(2)-P(1)/°	110.47(3)	110.0	116.2	116.9
I(2)-Cu(2)-P(2)/°	107.13(4)	109.0	106.2	104.3
I(1)-Cu(2)-N(2)/°	104.16(9)	102.7	107.2	110.4
I(2)-Cu(2)-N(2)/°	104.85(9)	104.6	105.3	110.3

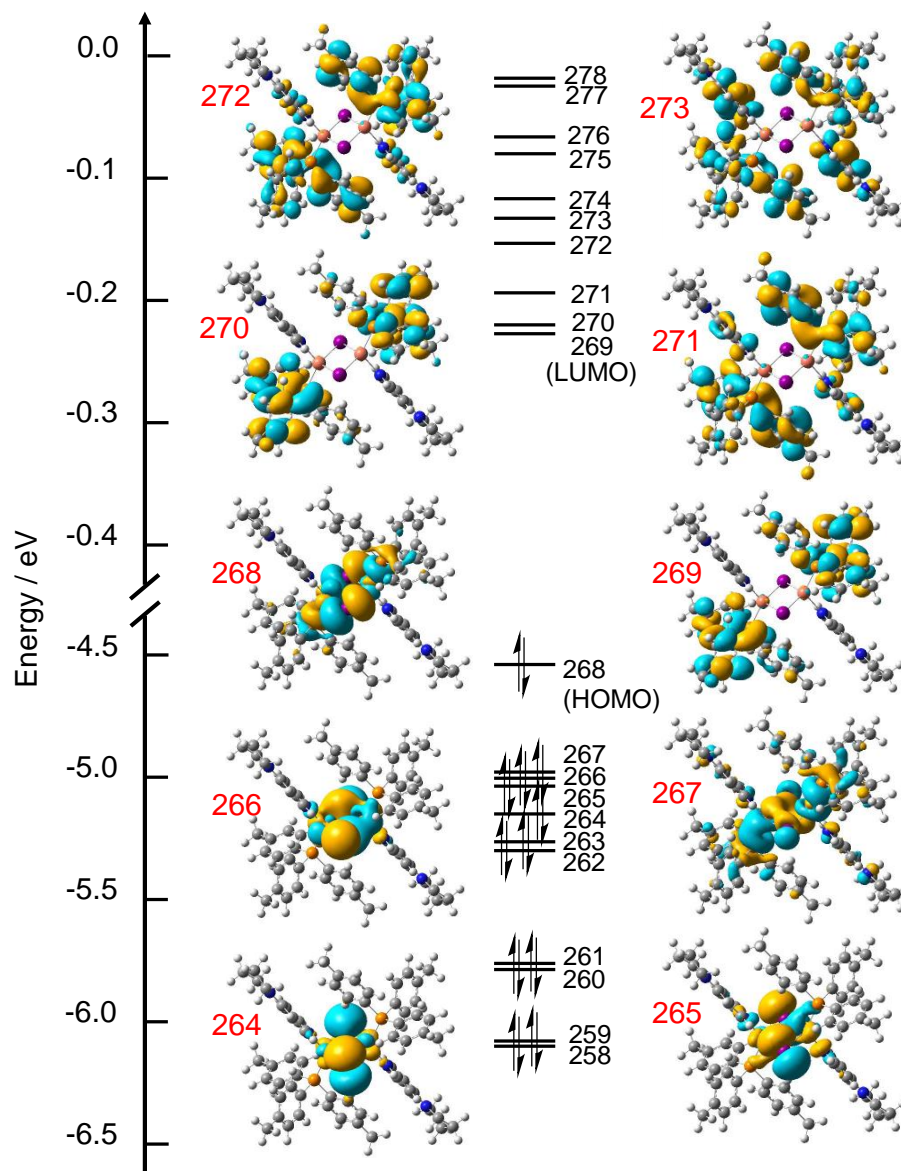


Figure 3-15. Kohn-Sham orbitals and energies at the frontier region of ground state optimized complex **6**.

Table 3-6. Selected bond lengths (Å) and bond angles (°) of **7** in S₀, S₁ and T₁ states after the optimization.

	X-ray	S₀	S₁	T₁
Cu(1)-Cu(2)	3.3741(9)	2.94	2.95	3.08
Cu(1)-I(1)/Å	2.7450(6)	2.74	2.71	2.76
Cu(1)-I(2)/Å	2.7002(6)	2.74	2.68	2.72
Cu(2)-I(1)/Å	2.7002(6)	2.74	2.63	2.64
Cu(2)-I(2)/Å	2.7450(6)	2.74	2.64	2.65
Cu(1)-P(1)/Å	2.2335(8)	2.27	2.33	2.31
Cu(1)-N(1)/Å	2.053(3)	2.09	2.06	2.04
Cu(2)-P(2)/Å	2.2335(8)	2.27	2.33	2.34
Cu(2)-N(2)/Å	2.053(3)	2.09	2.10	2.06
I(1)-Cu(1)-I(2)/°	103.42(2)	114.2	110.8	107.0
I(1)-Cu(1)-P(1)/°	111.06(3)	110.3	110.2	109.0
I(2)-Cu(1)-P(1)/°	109.79(3)	108.6	110.6	111.4
I(1)-Cu(1)-N(1)/°	106.67(7)	102.4	102.2	102.7
I(2)-Cu(1)-N(1)/°	102.71(8)	103.4	106.4	106.8
I(1)-Cu(2)-I(2)/°	103.42(2)	114.2	114.4	112.8
I(1)-Cu(2)-P(1)/°	109.79(3)	108.6	116.1	116.2
I(2)-Cu(2)-P(2)/°	111.06(3)	110.3	105.9	104.8
I(1)-Cu(2)-N(2)/°	102.71(8)	103.7	107.2	110.5
I(2)-Cu(2)-N(2)/°	106.67(7)	102.4	105.7	110.3

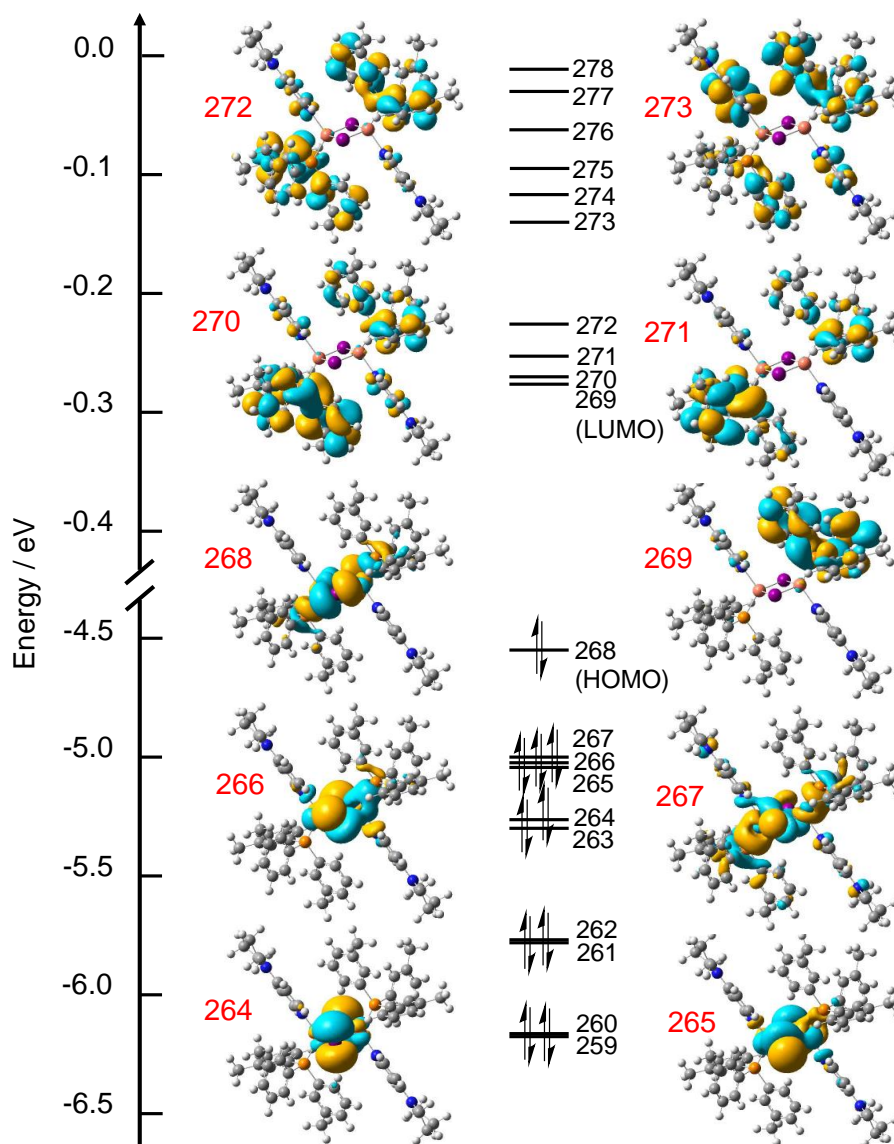


Figure 3-16. Kohn-Sham orbitals and energies at the frontier region of ground state optimized complex 7.

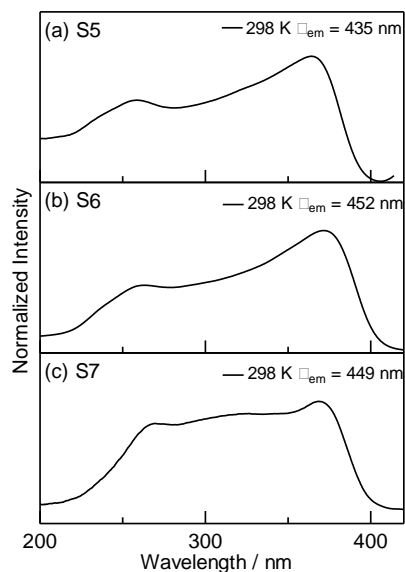


Figure 3-17. Excitation spectra of the complexes S5, S6 and S7 in the solid state at 298 K.

Starting from the S_0 optimized structures of complexes **5–7**, I calculated their vertical excitations. According to the natural transition orbital (NTO)⁴⁵ analysis of **5** (Scheme 3-2), three types of excitations are possible in the 290–350 nm region; charge transfer from the rhombic core to the phosphine ligand (i.e., $(M+X)L_1CT$ at 350 and 310 nm), charge transfer from the core to both ligands, $((M+X)L_{12}CT$ at 344 and 298 nm), and charge transfer from the core to the pyrpy ligand ($(M+X)L_2CT$ at 336 and 292 nm), where L_1 is PPh_3 and L_2 is pyrpy. Similar results were observed for complexes **6** and **7** (Schemes 3-3 and 3-4). Our computational analyses suggest that the absorptions observed for complexes **5–7** have contributions from both $(M+X)L_1CT$ and $(M+X)L_2CT$.

The calculated wavelengths for transitions from the TD-DFT-optimized lowest singlet excited state (S_1) and the lowest triplet excited (T_1), and the S_1-T_1 energy gap $\Delta(S_1-T_1)$ for each complex, are summarized in Table 3-7. The calculated emission wavelengths from the optimized S_1 states of **5** (488 nm), **6** (477 nm), and **7** (489 nm) are in qualitative agreement with the experimental values. The calculated $\Delta(S_1-T_1)$ values of the three complexes are relatively small (1715 cm^{-1} for **5**, 1694 cm^{-1} for **6**, and 1592 cm^{-1} for **7**) and decrease in the order: **5** > **6** > **7**. Given the smallness of these energy gaps, the emissions from complexes **5–7** originate from their S_1 states, consistent with TADF. The $\Delta(S_1-T_1)$ value for **7** is quantitatively in agreement with the estimated value (1090 cm^{-1}) based on the temperature dependence of the emission lifetime (Figure 3-18). The Cu_2I_2 unit was found to be asymmetric [$r(Cu-I) = 2.70, 2.67, 2.63, 2.64\text{ \AA}$] in the optimized S_1 state of **5**, in which the Cu-I bond distance of one of the two Cu sites is slightly longer. The optimized triplet excited state (T_1) of **5** displays similar features [$r(Cu-I) = 2.75, 2.71, 2.64, 2.65\text{ \AA}$] to the S_1 state, and similar structural

observations can be made for the optimized S_1 and T_1 structures of **6** and **7**. The nature of the emission from S_1 can be characterized by the electron density maps of the ground and excited states at the S_1 -optimized geometry (Figure 3-19); the electron density in each complex is observed to move from the phosphine ligand of one of the two Cu ions to the Cu-I unit, indicating that S_1 has (M+X) L_1 CT character. It is important to note that absorption occurs from the Cu_2I_2 unit to the phosphine ligands of both Cu ions, whereas emission is localized at one of two Cu sites, indicating that there are two low-lying singlet excited states for excitation and emission.

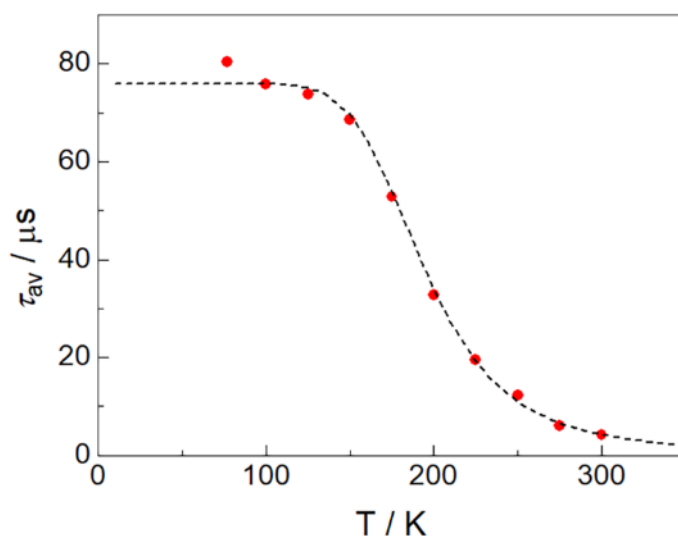


Figure 3-18. Temperature dependence of the average emission lifetime of complex **7** in the solid state. Assuming the two-state model involving the lowest excited singlet state (S_1) and the lowest excited triplet state (T_1), the observed lifetime can be expressed as a Boltzmann average by using equation (2).

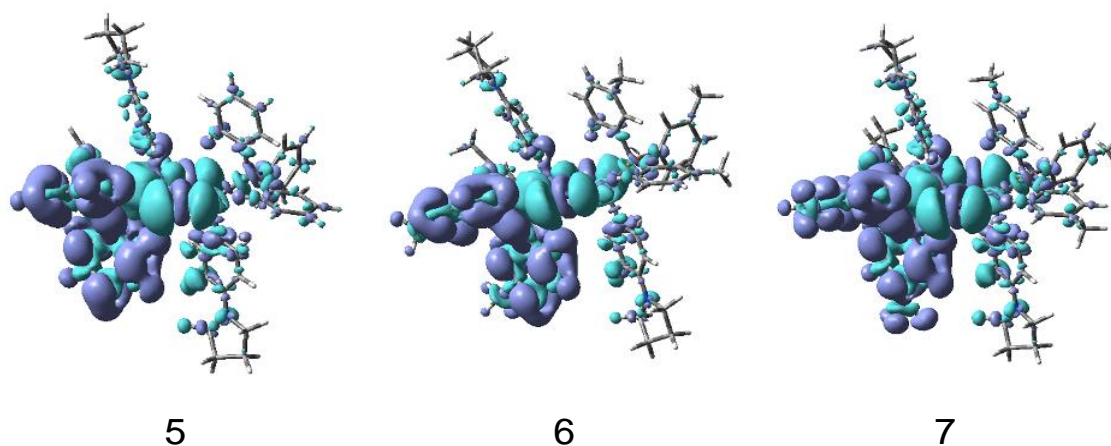


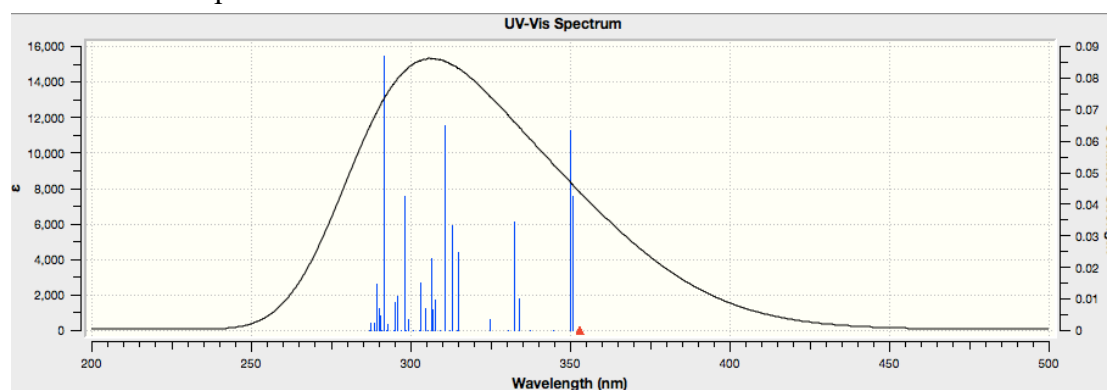
Figure 3-19. Ground-state and excited-state electron density differences at the S_1 -optimized geometries of complexes **5–7**.

Table 3-7. Calculated wavelengths (vertical transitions) at the optimized S_1 and T_1 states ($\lambda^{\text{em}}(S_1/T_1)$), the calculated S_1 - T_1 energy gaps [$\Delta(S_1-T_1)$], and the experimental emission-maximum wavelengths $\lambda^{\text{em}}(\text{exp})$.

	5	6	7
$\lambda^{\text{em}}(S_1) / \text{nm}$	488	477	489
$\lambda^{\text{em}}(T_1) / \text{nm}$	532	520	530
$\Delta(S_1-T_1) / \text{cm}^{-1}$	1715	1694	1592
$\lambda^{\text{em}}(\text{exp}) / \text{nm}$ at 298K	435	452	449

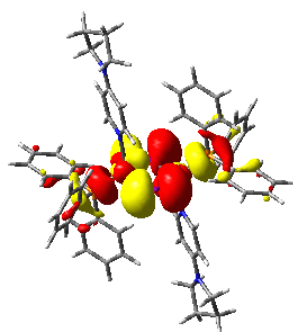
Scheme 3-2. Energy, oscillator strength, and transition orbitals of the important excitations for complex **5**.

Simulated UV spectrum:



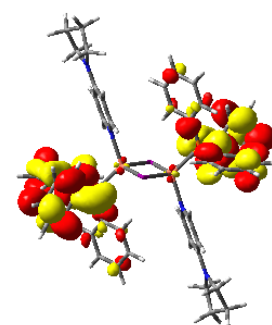
Excited State 2: 3.5365 eV (350.58 nm) f = 0.0426

243 -> 245	0.17398
244 -> 246	0.67620



occupied "hole"

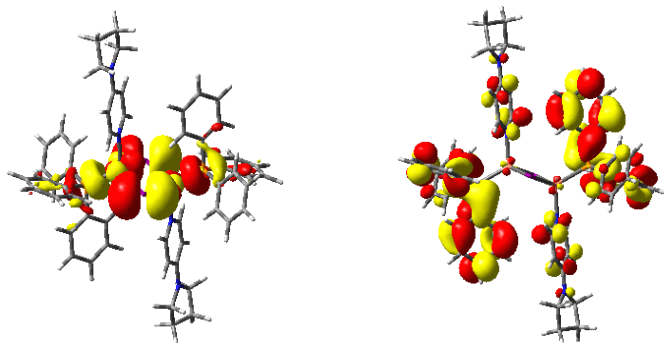
→



unoccupied "electron"

Excited State 3: 3.5417 eV (350.07 nm) f = 0.0634

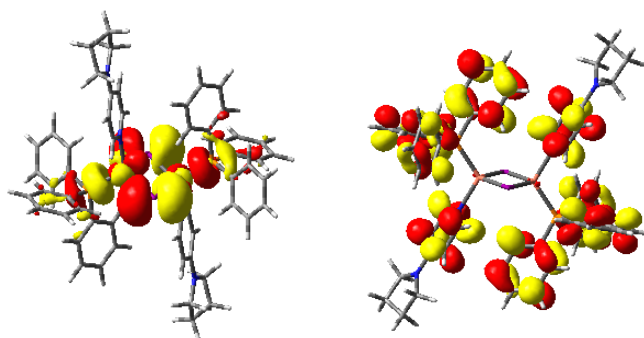
243 -> 248	-0.12335
244 -> 247	0.68377



occupied "hole" → unoccupied "electron"

Excited State 6: 3.7110 eV (334.10 nm) f = 0.0102

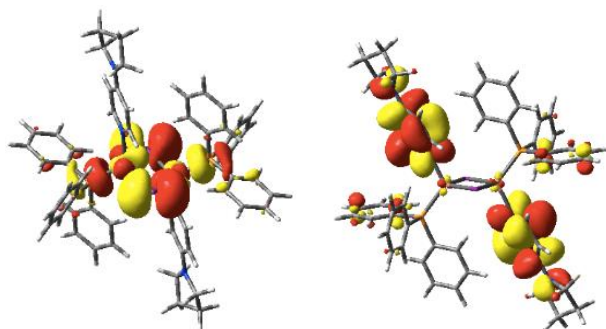
244 → 250	0.67453
244 → 254	0.12928



occupied "hole" → unoccupied "electron"

Excited State 7: 3.7314 eV (332.27 nm) f = 0.0342

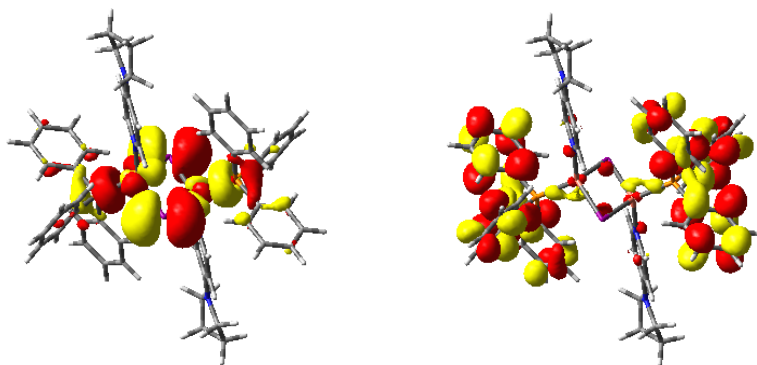
244 → 251	0.68171
-----------	---------



occupied "hole" → unoccupied "electron"

Excited State 15: 3.9889 eV (310.82 nm) f = 0.0648

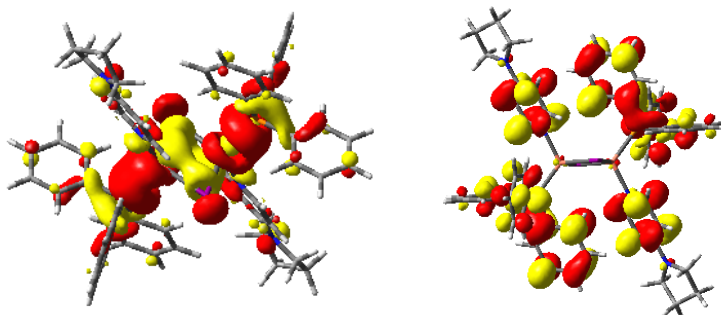
243 → 256	-0.11608
244 → 254	0.10337
244 → 255	0.65090



occupied "hole" → unoccupied "electron"

Excited State 30: 4.1571 eV (298.25 nm) f=0.0424

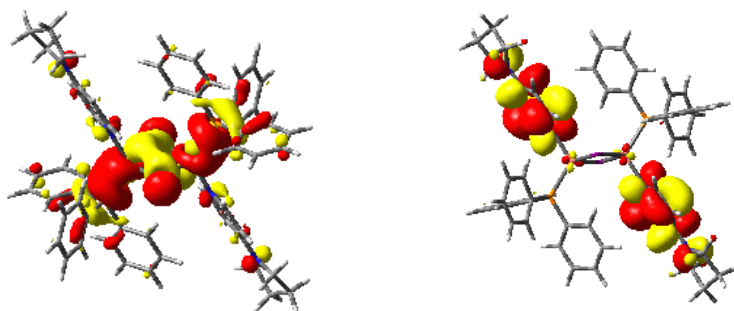
241 -> 250	-0.10301
242 -> 250	0.31901
242 -> 251	-0.10866
243 -> 249	0.54265
244 -> 254	-0.13190



occupied "hole" → unoccupied "electron"

Excited State 38: 4.2530 eV (291.52 nm) f=0.0871

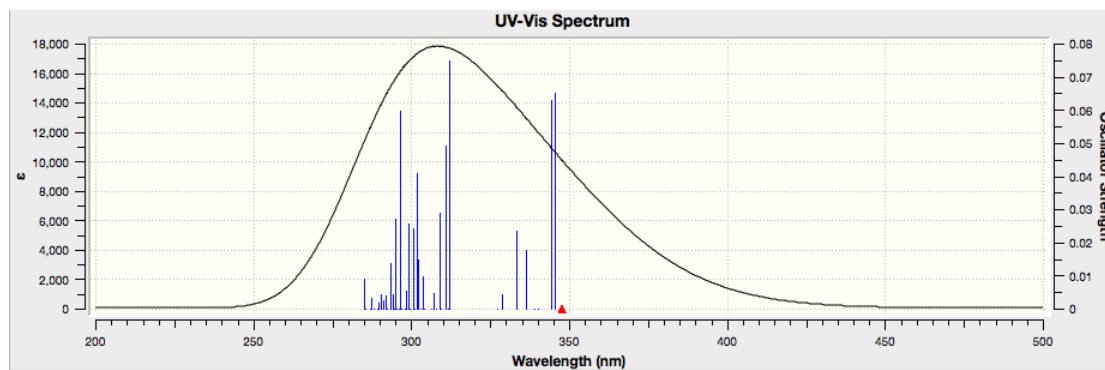
240 -> 245	-0.15681
241 -> 250	-0.13262
242 -> 251	0.10302
243 -> 249	-0.11466
243 -> 252	0.56038
243 -> 253	-0.14626
244 -> 261	-0.15072



occupied “hole” → unoccupied “electron”

Scheme 3-3. Energy, oscillator strength, and transition orbitals for complex **6**.

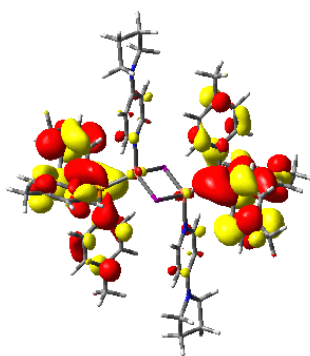
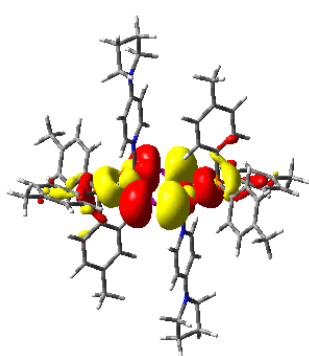
Simulated UV spectrum:



Excited State 1: 3.5652 eV (347.76 nm) f = 0.0000

267 → 270 0.16990

268 → 269 0.67396



occupied “hole” → unoccupied “electron”

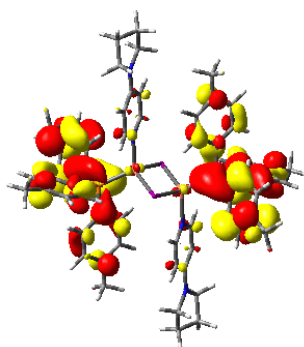
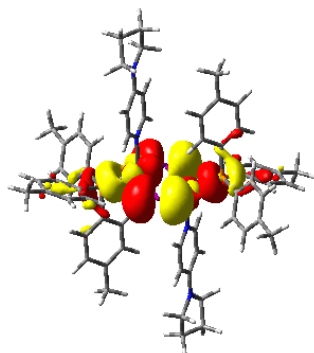
Excited State 2: 3.5875 eV (345.60 nm) f = 0.0651

267 → 269 0.16808

268 → 270 0.63815

268 → 271 -0.19741

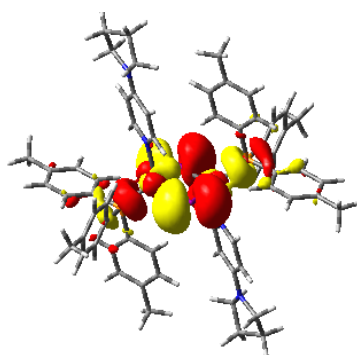
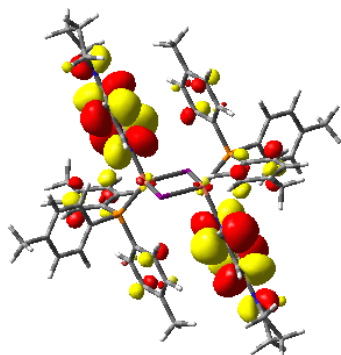
268 → 275 -0.11623



occupied "hole" → unoccupied "electron"

Excited State 3: 3.6028 eV (344.14 nm) f = 0.0629

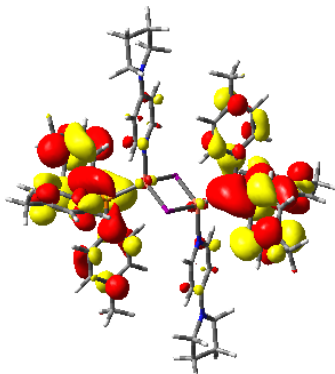
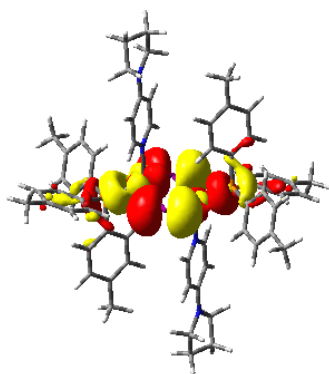
267 -> 272	0.11393
268 -> 270	0.21509
268 -> 271	0.64682
268 -> 275	0.10165



occupied "hole" → unoccupied "electron"

Excited State 6: 3.6859 eV (336.37 nm) f = 0.0176

268 -> 274	0.48171
268 -> 275	0.45762
268 -> 278	0.14999

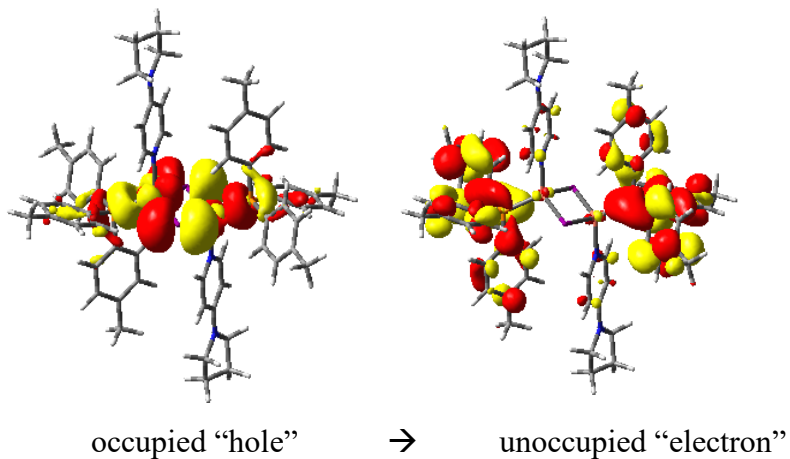


occupied "hole" → unoccupied "electron"

Excited State 11: 3.9746 eV (311.94 nm) f = 0.0748

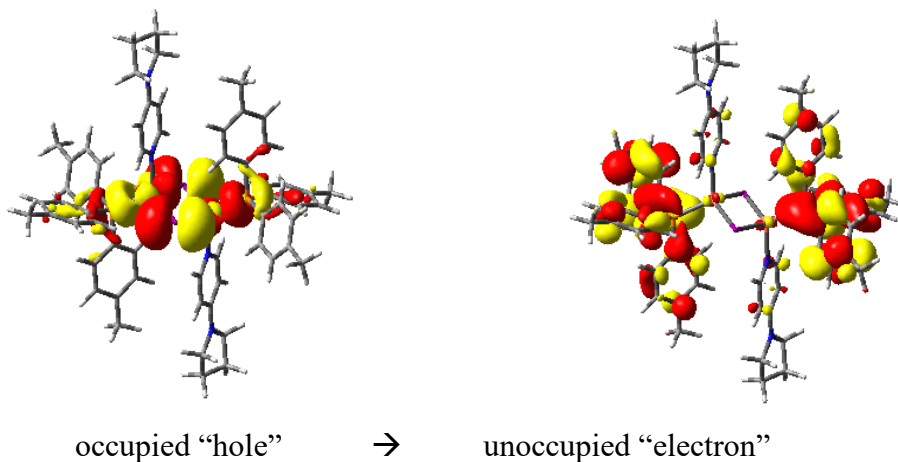
263 -> 273	0.14350
263 -> 276	-0.18952
265 -> 270	0.15017
265 -> 271	-0.23131
265 -> 275	-0.29388
266 -> 270	0.11544
266 -> 271	-0.14302

266 -> 275	-0.20409
267 -> 269	0.16351
267 -> 273	-0.10601
267 -> 276	0.14989
268 -> 279	0.30260



Excited State 13: 3.9901 eV (310.73 nm) f = 0.0491

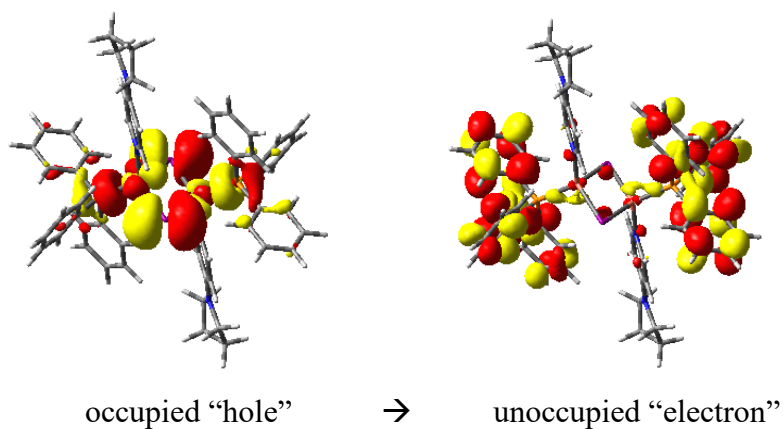
263 -> 276	0.11160
265 -> 271	0.18105
265 -> 275	0.15421
266 -> 271	0.12279
266 -> 275	0.11060
268 -> 279	0.57296
268 -> 282	0.12834



Excited State 15: 4.0140 eV (308.88 nm) f = 0.0291

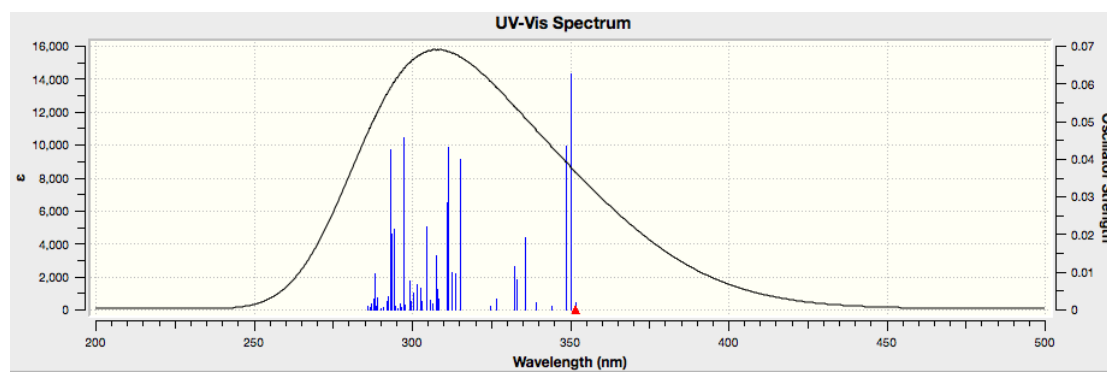
263 -> 269	-0.14479
265 -> 270	0.27230
265 -> 274	0.13368

265 -> 275	0.14964
265 -> 278	0.10497
266 -> 270	0.20104
266 -> 275	0.11537
267 -> 269	0.45597
267 -> 273	0.10496
268 -> 270	-0.13070



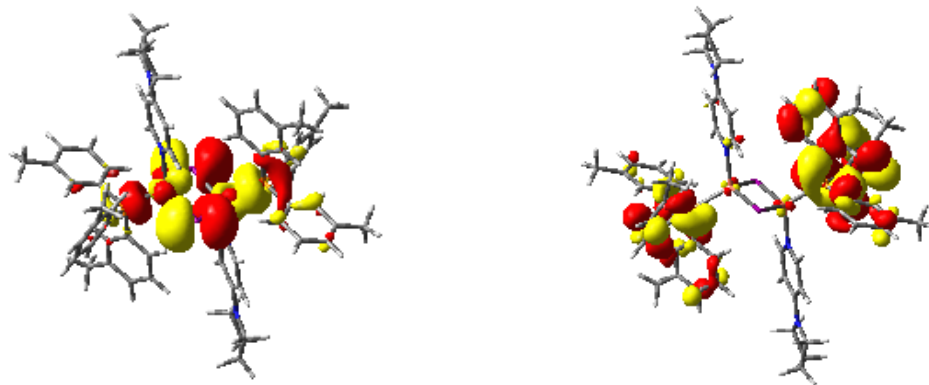
Scheme 3-4. Energy, oscillator strength, and transition orbitals for complex 7.

Simulated UV spectrum:



Excited State 1: 3.5261 eV (351.62 nm) f = 0.0019

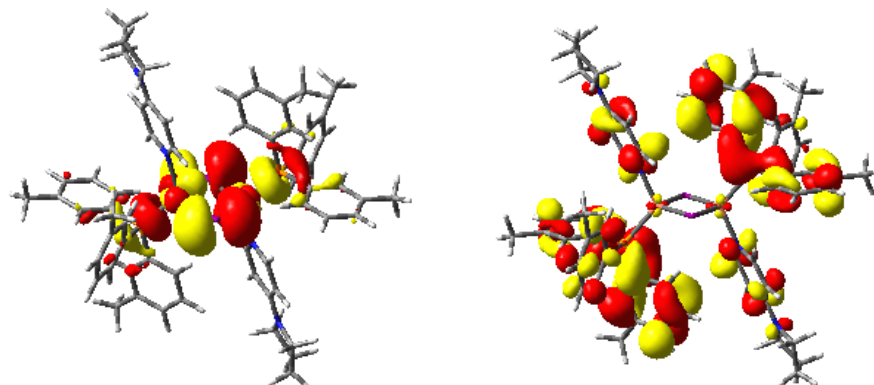
267 -> 269	-0.11585
268 -> 269	0.58497
268 -> 270	0.27140
268 -> 271	-0.21622



occupied "hole" → unoccupied "electron"

Excited State 2: 3.5395 eV (350.29 nm) f = 0.0628

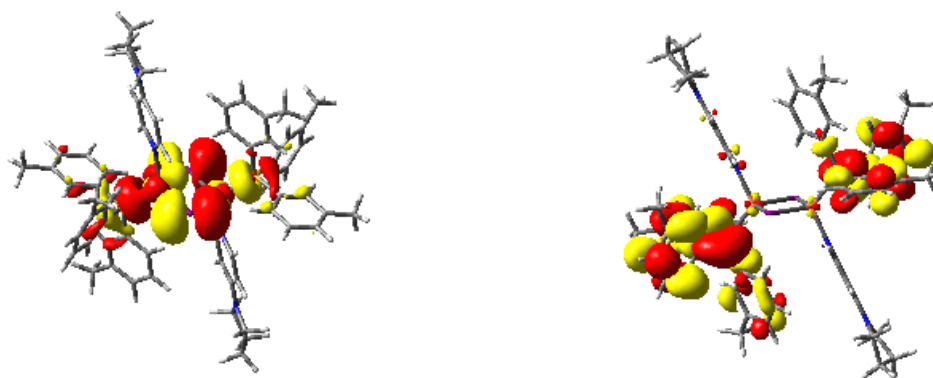
268 -> 269	-0.24524
268 -> 270	0.62614
268 -> 271	0.13550



occupied "hole" → unoccupied "electron"

Excited State 3: 3.5577 eV (348.50 nm) f = 0.0435

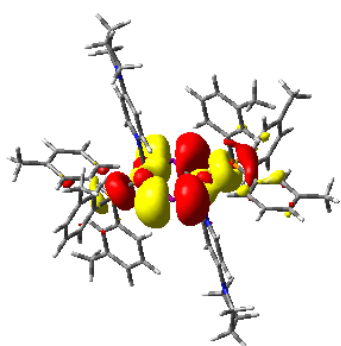
267 -> 270	-0.10341
268 -> 269	0.25053
268 -> 271	0.62411



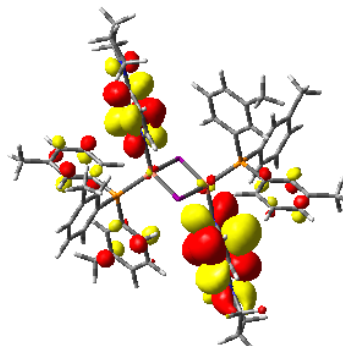
occupied "hole" → unoccupied "electron"

Excited State 6: 3.6947 eV (335.58 nm) f = 0.0191

268 -> 274	0.31665
268 -> 275	0.58801
268 -> 276	-0.11789



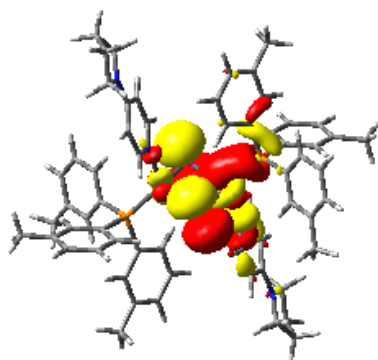
occupied "hole"



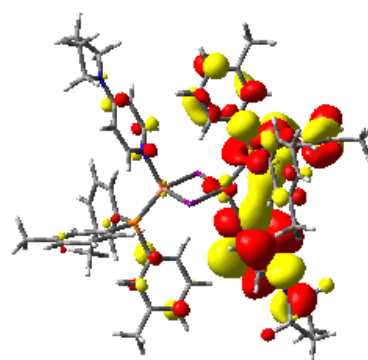
unoccupied "electron"

Excited State 11: 3.9343 eV (315.14 nm) f = 0.0399

263 -> 273	0.10206
263 -> 276	-0.15534
265 -> 270	-0.16842
265 -> 271	-0.14406
265 -> 275	0.13687
266 -> 269	-0.10166
266 -> 270	0.21858
266 -> 271	0.18111
266 -> 275	-0.18290
267 -> 269	-0.15369
267 -> 270	0.16745
267 -> 271	0.20856
267 -> 272	-0.14090
267 -> 273	0.12332
267 -> 275	-0.17240
267 -> 276	-0.16092



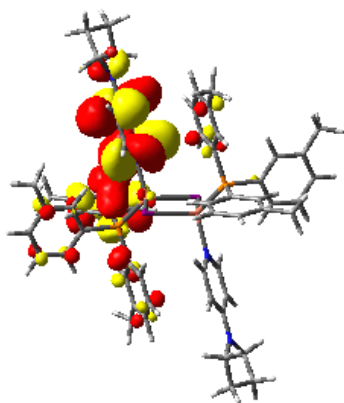
occupied "hole"



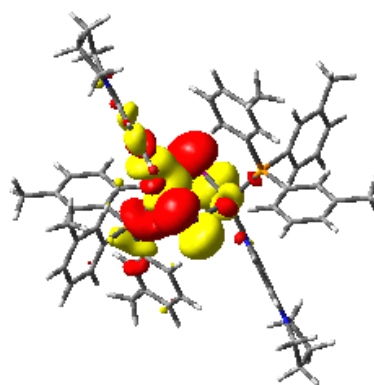
unoccupied "electron"

Excited State 15: 3.9833 eV (311.26 nm) f = 0.0430

263 -> 273	-0.11766
265 -> 272	0.10518
265 -> 273	0.11324
266 -> 272	-0.13126
266 -> 273	-0.15132
266 -> 275	0.11687
267 -> 269	-0.10297
267 -> 270	0.12879
267 -> 272	-0.21035
267 -> 273	-0.18052
267 -> 275	0.12146
267 -> 277	0.14689
268 -> 279	0.29742
268 -> 280	0.22539
268 -> 281	0.15971



occupied "hole"



unoccupied "electron"

3-4. Conclusion

I synthesized three new luminescent dinuclear Cu(I) complexes, $[\text{Cu}_2\text{I}_2(\text{pyrpy})_2(\text{PR}_3)_2]$ ($\text{PR}_3 = \text{PPh}_3$ (**5**), $\text{P}(m\text{-tol})_3$ (**6**), $\text{P}(p\text{-tol})_3$ (**7**)) using both the traditional solution method and the recently developed solvent-free thermal method. Single crystals obtained from the traditional solution reaction enabled us to determine the X-ray crystal structures of these complexes; this revealed that complexes **5–7** contain halide-bridged rhombic dinuclear $\{\text{Cu}_2\text{I}_2\}$ cores. Complexes **5** and **7** were successfully synthesized by both methods, whereas complex **6** was not obtained using the solvent-free thermal method. Thermogravimetric analyses and PXRD studies clearly reveal that the melting of the organic moieties promotes the reaction with solid CuI to form luminescent Cu(I) complexes, and that the temperature to form **5** was significantly lower than that required to form **7**. The three complexes exhibit strong blue emissions at around 440 nm ($\Phi = 0.24, 0.31, \text{ and } 0.51$ for **5**, **6**, and **7**, respectively), with lifetimes of a few microseconds, and radiative decay constants (k_r) that exhibit large temperature dependences, indicative of TADF. TD-DFT calculations reveal a small energy gap between the S_1 and T_1 states of **5–7** complexes, suggesting TADF with the (M+X)LCT character. Although further fine tuning of the solvent-free thermal syntheses of these Cu(I) TADF materials is still required, I believe that this method is promising for the direct preparation of luminescent layers on thin-film electronic devices, such as organic light-emitting diodes.

3-5. References

- (1) Kobayashi, A.; Kato, M. Stimuli-Responsive Luminescent Copper(I) Complexes for Intelligent Emissive Devices. *Chem. Lett.* **2017**, 46, 154–162.
- (2) Kamecka, A.; Muszyńska, W.; Kapturkiewicz, A. Luminescence Properties of Heteroleptic $[\text{Ru}(\text{H})(\text{CO})(\text{N}^{\wedge}\text{N})(\text{tpp})_2]^+$ Complexes: Comparison with their $[\text{Os}(\text{H})(\text{CO})(\text{N}^{\wedge}\text{N})(\text{tpp})_2]^+$ Analogues. *J. Lumin.* **2017**, 192, 842–852.
- (3) Donato, L.; McCusker, C. E.; Castellano, F. N.; Zysman, C. E. Mono- and Dinuclear Cationic Iridium(III) Complexes Bearing a 2,5-Dipyridylpyrazine (2,5-dpp) Ligand. *Inorg. Chem.* **2013**, 52, 8495–8504.
- (4) Julio, F.; Gabriel, A.; Bautista, D.; and Gonzalez-Herrero, P. Exploring Excited-State Tunability in Luminescent Tris-Cyclometalated Platinum(IV) Complexes: Synthesis of Heteroleptic Derivatives and Computational Calculations. *Chem. Eur. J.* **2014**, 20, 17346–17359.
- (5) Yamashita, Y.; Tateishi, T.; Sawaguchi, K.; Kobayashi, A.; Kato, M.; Nakajima, K. Tribo-, thermo-, and Vapochromic Behavior of Hydrazone–Pt(II) Complexes Induced by Protonation–Deprotonation in the Solid State, and Their Luminescence Properties in Solution. *Chem. Lett.* **2014**, 43, 1912–1914.
- (6) Kataoka, Y.; Kitagawa, Y.; Kawakami, T.; Okumura, M. Photophysical Properties of Mono- and Di-Nuclear Platinum(II) Complexes with the Tridentate Ligand 2-Phenyl-6-(1H-pyrazol-3-yl)-pyridine: A DFT and TDDFT Study. *J. Org. Chem.* **2013**, 743, 163–169.
- (7) Shimada, K.; Kobayashi, A.; Ono, Y.; Ohara, H.; Hasegawa, T.; Taketsugu, T.; Sakuda, E.; Akagi, S.; Kitamura, N.; Kato, M. Core-Structure-Dependent Luminescence of Thiolato-Bridged Copper(I) Cluster Complexes. *J. Phys. Chem. C* **2016**, 120, 16002–16011.
- (8) Cunningham, C. T.; Cunningham, K. L. H.; Michalec, J. F.; McMillin, D. R. Cooperative Substituent Effects on the Excited States of Copper Phenanthrolines. *Inorg. Chem.* **1999**, 38, 4388–4392.
- (9) McCusker, C. E.; Castellano, F. N. Design of a Long-Lifetime, Earth-Abundant, Aqueous Compatible Cu(I) Photosensitizer Using Cooperative Steric Effects. *Inorg. Chem.* **2013**, 52, 8114–8120.
- (10) Benito, Q.; Xavier, F.; Goff, L.; Nocton, G.; Fargues, A.; Garcia, A.; Berhault, A.; Kahlal, S.; Saillard, J. Y.; Charlotte, M.; Trebosc, J.; Gacoin, T.; Boilot, J. P., Perruchas, S. Geometry Flexibility of Copper Iodide Clusters: Variability in Luminescence Thermochromism. *Inorg. Chem.* **2015**, 54, 4483–4494.
- (11) Angelis, F. D.; Fantacci, S.; Sgamellotti, A.; Cariati, E.; Ugo, R.; Ford, P. C. Electronic Transitions Involved in the Absorption Spectrum and Dual Luminescence of Tetranuclear Cubane $[\text{Cu}_4\text{L}_4(\text{Pyridine})_4]$ Cluster: A Density Functional Theory/Time-Dependent Density Functional Theory Investigation. *Inorg. Chem.* **2006**, 45, 10576–10584.
- (12) Kyle, K. R.; Ryu, C. K.; DiBenedetto, J. A.; Ford, P. C. Photophysical Studies in Solution of the Tetranuclear Copper(I) Clusters $\text{Cu}_4\text{L}_4\text{L}_4$ (L = Pyridine or Substituted Pyridine). *J. Am. Chem. Soc.* **1991**, 113, 2954–2965.
- (13) Perruchas, S.; Goff, X. F. L.; Maron, S.; Maurin, I.; Guillen, F.; Garcia, A.; Gacoin, T.; Boilot, J. P. Mechanochromic and Thermochromic Luminescence of a Copper Iodide Cluster. *J. Am. Chem. Soc.* **2010**, 132, 10967–10969.

- (14) Berhault, A.; Kahlal, S.; Saillard, J. Y.; Martineau, C.; Trébosc, J.; Gacoin, T.; Boilot, J. P.; Perruchas, S. Geometry Flexibility of Copper Iodide Clusters: Variability in Luminescence Thermochromism. *Inorg. Chem.* **2015**, *54*, 4483–4494.
- (15) Liu, Z.; Qayyum, M. F.; Wu, C.; Whited, M. T.; Djurovich, P. I.; Hodgson, K. O.; Hedman, B.; Solomon, E. I.; Thompson, M. E. A Codeposition Route to CuI–Pyridine Coordination Complexes for Organic Light-Emitting Diodes. *J. Am. Chem. Soc.* **2011**, *133*, 3700–3703.
- (16) Zhao, C. W.; Ma, J. P.; Liu, Q. K.; Wang, X. R.; Liu, Y.; Yang, J.; Yang, J. S.; Dong, Y. B. An In Situ Self-Assembled Cu₄I₄–MOF-Based Mixed Matrix Membrane: A Highly Sensitive and Selective Naked-Eye Sensor for Gaseous HCl. *Chem. Commun.* **2016**, *52*, 5238–5241.
- (17) Tanaka, N.; Nanjo, M. The Thermal Decomposition of Metal Oxalato Complexes. *Bull. Chem. Soc. Jpn.* **1967**, *40*, 330–333.
- (18) Dikarev, E. V.; Li, B.; Chernyshev, V. V.; Shpanchenko, R. V.; Petrukhnina, M. A. Coordination Polymers Formed in Solution and in Solvent-Free Environment. Structural Transformation due to Interstitial Solvent Removal Revealed by X-Ray Powder Diffraction. *Chem. Commun.* **2005**, 3274–3276.
- (19) Barea, E.; Navarro, J. A. R.; Salas, J. M.; Masciocchi, N.; Galli, S.; Sironi, A. Coordination Frameworks Containing the Pyrimidin-4-olate Ligand. Synthesis, Thermal, Magnetic, and Ab Initio XRPD Structural Characterization of Nickel and Zinc Derivatives. *Inorg. Chem.* **2004**, *43*, 473–481.
- (20) Espallargas, G. M.; Brammer, L.; Streek, J. W. D.; Shankland, K.; Florence, A. J.; Adams, H. Reversible Extrusion and Uptake of HCl Molecules by Crystalline Solids Involving Coordination Bond Cleavage and Formation. *J. Am. Chem. Soc.* **2006**, *128*, 9584–9585.
- (21) Adams, C. J.; Crawford, P. C.; Orpen, A. G.; Podesta, T. J.; Salt, B. Thermal Solid State Synthesis of Coordination Complexes from Hydrogen Bonded Precursors. *Chem. Commun.* **2005**, 2457–2458.
- (22) Tsuchiya, R.; Murai, K.; Uehara, A.; Kyuno, E. Solid Phase Thermal S_E Reaction of Metal Complexes. *Chem. Lett.* **1974**, 21–24.
- (23) Hoshina, G.; Ohba, S.; Nakajima, K.; Ishida, H.; Kojima, M.; Tsuchimoto, M. Molecular Rearrangement Accompanied by Solid-State Isomerization of {N,N'-Di-3-ethoxysalicylidene-(R,S)(S,R)-1,2-diphenyl-1,2-ethanediamine} oxovanadium(IV). *Bull. Chem. Soc. Jpn.* **1999**, *72*, 1037–1041.
- (24) Tsuchiya, R.; Uehara, A.; Sakui, M.; Kyuno, E. Preparation of Squarato-Complexes and Thermal S_E Reaction Thereof in Solid Phase. *Bull. Chem. Soc. Jpn.* **1974**, 1511–1514.
- (25) Kutal, C.; Bailar, J. C., Jr. Reactions of Coordination Compounds in the Solid State. Racemization of (+)-[Co(en)₃] X₃•nH₂O. *J. Phys. Chem.* **1972**, *76*, 119–127.
- (26) Kuroda, R.; Yoshida, J.; Nakamura, A.; Nishikiori, S. I. Annealing Assisted Mechanochemical Syntheses of Transition-Metal Coordination Compounds and Co-Crystal Formation. *Cryst. Eng. Comm.* **2009**, *11*, 427–432.
- (27) Braga, D.; Grepioni, F.; Maini, L.; Mazzeo, P. P.; Ventura, B. Solid-State Reactivity of Copper(I) Iodide: Luminescent 2D-Coordination Polymers of CuI with Saturated Bidentate Nitrogen Bases. *New J. Chem.* **2011**, *35*, 339–344.
- (28) Ohara, H.; Kobayashi, A.; Kato, M. Simple Manual Grinding Synthesis of Highly Luminescent Mononuclear Cu(I)–Iodide Complexes. *Chem. Lett.* **2014**, *43*, 1324–1326.

- (29) Liang, P.; Kobayashi, A.; Hasegawa, T.; Yoshida, M.; Kato, M. Thermal and Mechanochemical Syntheses of Luminescent Mononuclear Copper(I) Complexes. *Eur. J. Inorg. Chem.* **2017**, 5134–5142.
- (30) Lakowicz, J. R. Principles of Fluorescence Spectroscopy, 3rd ed., Springer, New York, 2006; pp 141–143.
- (31) *Crystal Clear*, Data Collection and Processing Software, Rigaku Corporation: Tokyo, Japan, **1998–2014**.
- (32) *SIR-2014*: Burla, M. C.; Caliendo, R.; Carrozzini, B.; Cascarano, G. L.; Giacovazzo, C.; Mallamo, M.; Mazzone, A.; Polidori, G. Crystal Structure Determination and Refinement via SIR2014. *J. Appl. Cryst.* 2015, **48**, 306–309.
- (33) *SHELXL-2014* and *SHELEXS-2013*: Sheldrick, G. M. A Short History of SHELX. *Acta Crystallogr. A.* **2008**, *64*, 112–122.
- (34) *CrystalStructure 4.1*, Crystal Structure Analysis Package, Rigaku Corporation: Tokyo, Japan, **2000–2014**.
- (35) (a) Perdew, J. P.; Burke, K.; Ernzerhof, M. Generalized Gradient Approximation Made Simple. *Phys. Rev. Lett.* **1996**, *77*, 3865–3868. (b) Perdew, J. P.; Burke, K.; Ernzerhof, M. Errata: Generalized Gradient Approximation Made Simple. *Phys. Rev. Lett.* **1997**, *78*, 1396. (c) Adamo, C.; Barone, V. Toward Reliable Density Functional Methods Without Adjustable Parameters: The PBE0 Model. *J. Chem. Phys.* **1999**, *110*, 6158–6169.
- (36) *Gaussian 16*, Revision A.03, Frisch, M. J.; Trucks, G. W.; Schlegel, H. B.; Scuseria, G. E.; Robb, M. A.; Cheeseman, J. R.; Scalmani, G.; Barone, V.; Petersson, G. A.; Nakatsuji, H.; Li, X.; Caricato, M.; Marenich, A. V.; Bloino, J.; Janesko, B. G.; Gomperts, R.; Mennucci, B.; Hratchian, H. P.; Ortiz, J. V.; Izmaylov, A. F.; Sonnenberg, J. L.; Williams-Young, D.; Ding, F.; Lipparini, F.; Egidi, F.; Goings, J.; Peng, B.; Petrone, A.; Henderson, T.; Ranasinghe, D.; Zakrzewski, V. G.; Gao, J.; Rega, N.; Zheng, G.; Liang, W.; Hada, M.; Ehara, M.; Toyota, K.; Fukuda, R.; Hasegawa, J.; Ishida, M.; Nakajima, T.; Honda, Y.; Kitao, O.; Nakai, H.; Vreven, T.; Throssell, K.; Montgomery, J. A., Jr.; Peralta, J. E.; Ogliaro, F.; Bearpark, M. J.; Heyd, J. J.; Brothers, E. N.; Kudin, K. N.; Staroverov, V. N.; Keith, T. A.; Kobayashi, R.; Normand, J.; Raghavachari, K.; Rendell, A. P.; Burant, J. C.; Iyengar, S. S.; Tomasi, J.; Cossi, M.; Millam, J. M.; Klene, M.; Adamo, C.; Cammi, R.; Ochterski, J. W.; Martin, R. L.; Morokuma, K.; Farkas, O.; Foresman, J. B.; Fox, D. J. Gaussian, Inc., Wallingford CT, **2016**.
- (37) (a) Dunning, T. H., Jr.; Hay, P. J. Modern Theoretical Chemistry; Plenum: New York, **1977**; Vol. 3, pp 1–28. (b) Fuentealba, P.; Preuss, H.; Stoll, H.; Vonszentpaly, L. A Proper Account of Core-Polarization with Pseudopotentials: Single Valence-Electron Alkali Compounds. *Chem. Phys. Lett.* **1982**, *89*, 418–422.
- (38) (a) Ditchfie, R.; Hehre, W. J.; Pople, J. A. Self-Consistent Molecular-Orbital Methods. IX. An Extended Gaussian-Type Basis for Molecular-Orbital Studies of Organic Molecules, *J. Chem. Phys.* **1971**, *54*, 724. (b) Hehre, W. J.; Ditchfie, R.; Pople, J. A., Self-Consistent Molecular Orbital Methods. XII. Further Extensions of Gaussian-Type Basis Sets for use in Molecular Orbital Studies of Organic Molecules. *J. Chem. Phys.* **1972**, *56*, 2257. (c) Hariharan, P. C.; Pople, J. A. The Influence of Polarization Functions on Molecular Orbital Hydrogenation Energies. *Theor. Chim. Acta* **1973**, *28*, 213–222. (d) Francl, M. M.; Pietro, W. J.; Hehre, Self-Consistent Molecular Orbital

Methods. XXIII. A Polarization-Type Basis Set for Second-Row Elements. *J. Chem. Phys.* **1982**, *77*, 3654.

(39) (a) Weigend, F.; Ahlrichs, R. Balanced Basis Sets of Split Valence, Triple Zeta Valence and Quadruple Zeta Valence Quality for H to Rn: Design and Assessment of Accuracy. *Phys. Chem. Chem. Phys.* **2005**, *7*, 3297–3305. (b) Weigend, F. Accurate Coulomb-Fitting Basis Sets for H to Rn,” *Phys. Chem. Chem. Phys.* **2006**, *8*, 1057–1065.

(40) Karagiannidis, P.; Hadjikakou, S. K.; Aslanidis, P.; Hountas, A. Synthesis and Photochemical Study of Cu(I) Complexes with Tri-p-tolylphosphine and Heterocyclic Thiones. The Crystal Structure of [CuCl(pymtH)(p-CH₃C₆H₄)₃P]₂. *Inorg. Chim. Acta* **1990**, *178*, 27–34.

(41) Wallesch M.; Verma A.; Fléchon C.; Flügge H.; Zink D. M.; Seifermann, S. M.; Navarro, J. M.; Vitova, T.; Göttlicher, J.; Steininger, R.; Weinhardt, L.; Zimmer, M.; Gerhards, M.; Heske, M.; Bräse, S.; Baumann, T.; Volz, D. Towards Printed Organic Light-Emitting Devices: A Solution-Stable, Highly Soluble Cu^I-NHetPHOS. *Chem. Eur. J.* **2016**, *22*, 16400–16405.

(42) Ghorai, A.; Mondal, J.; Patra, G. K. Photoluminescent Mixed Ligand Complexes of CuX (X = Cl, Br, I) with PPh₃ and a Polydentate Imino-Pyridyl Ligand – Syntheses, Structural Variations and Catalytic Property. *J. Mol. Struct.* **2015**, *1097*, 52–60.

(43) Araki, H.; Tsuge, K.; Sasaki, Y.; Ishizaka, S.; Kitamura, N. Luminescence Ranging from Red to Blue: A Series of Copper(I)-Halide Complexes Having Rhombic {Cu₂(μ-X)₂} (X = Br and I) Units with N-Heteroaromatic Ligands. *Inorg. Chem.* **2005**, *44*, 9667–9675.

(44) Tsuge, K.; Chishina, Y.; Hashiguchi, H.; Sasaki, Y.; Kato, M.; Ishizaka, S.; Kitamura, N. Luminescent Copper(I) Complexes with Halogenido-Bridged Dimeric Core. *Coord. Chem. Rev.* **2016**, *306*, 636–651.

(45) Martin, R. L. Natural Transition Orbitals. *J. Chem. Phys.* **2003**, *118*, 4775–4777.

Chapter 4

General conclusions

The studies in this thesis demonstrated the relationship between melting point of ligands and the heating temperature. According to the two groups of complexes, identified by VTPXRD and TG, the complexation of reagents started at a temperature slightly lower than the melting point of ligands, while, the complexes obtained around the melting point in accordance with the solution synthesized. Meanwhile, the ligand dependence of complexation was observed, as for the *m*-tolylphosphine, amorphous state was obtained by thermal method instead of totally crystallized.

In chapter 1, three new mononuclear CuI complexes [CuI(PPh₃)₂L] (L = 4-aiq, 5-aiq, and 5-niq) were synthesized by conventional solution reactions, mechanochemical syntheses, and newly developed thermal syntheses. The introduction of an amino or nitro group to the isoquinoline ligand significantly affected not only the luminescence properties, but also the mechanochemical synthesis. In the mechanochemical syntheses of the three functionalized isoquinoline complexes, a small amount of PhCN solvent was required to form the mononuclear complexes. The melting point differences of ligand **1** and the **2-4** prompted us to investigate the thermal synthesis of luminescent CuI complex. Complexes **2** and **3** with amino-functionalized isoquinoline ligands were successfully synthesized in high yields by simply heating the ground mixtures of the three starting materials (CuI, PPh₃, and L) at ca. 100 °C. Complexes **2** and **3** exhibited yellow and orange phosphorescence with ms-range lifetimes originating from the ligand-centered ³ππ* excited state, whereas complex **4**, with a nitro-functionalized isoquinoline ligand, did not show any emission in the visible region. The TD-DFT calculations indicated that the introduction of an electron-donating amino group to the isoquinoline ligand stabilized the ¹ππ* excited state localized on the isoquinoline ligand, whereas the MLCT excited state of complex **4** was remarkably stabilized by the electron-withdrawing nature of the nitro group.

In the chapter 3, three new dinuclear Cu(I) luminescent complexes, [Cu₂I₂(pyrpy)₂(PR₃)₂] (PR₃= PPh₃ (**5**), P(*m*-tol)₃ (**6**), P(*p*-tol)₃ (**7**)) were synthesized by both the normal solution reaction and recently-developed solvent-free thermal synthesis. Complexes **5** and **7** were successfully synthesized by both methods, whereas the complex **6** was not obtained by the solvent-free thermal reaction. Thermogravimetric analysis and PXRD measurements clearly revealed that the melting of organic ligands promotes the reaction with CuI solid to form luminescent Cu(I) complexes, and the temperature to form the dinuclear complex **5** was significantly lower than that of **7**. These three complexes exhibit strong blue emission at around 440 nm (Φ = 0.24, 0.31, and 0.51 for **5**, **6**, and **7**, respectively) with a few μs lifetime and the large temperature dependence of radiative decay constants (k_r) are indicative of TADF. TDDFT results confirmed the small energy gap between S₁ and T₁ states of three complexes, and the TADF from the S₁ has (M+X)LCT character.

The above results illustrated the possibility of solvent-free thermal method to synthesize luminescent Cu(I) luminescent complexes, and the heating temperature largely depending on the melting of organic ligands. Although, the studies of mechanism of metal-organic thermal synthesis has not been explored massively,

thermal method that described in this thesis may provide one more way in the domain of green chemistry.